

See without being seen

**Novel, radiolucent MRI receive arrays
for MR-linac and PET/MRI**

Stefan Zijlema

See without being seen

Novel, radiolucent MRI receive arrays for
MR-linac and PET/MRI

Stefan Emiel Zijlema

Cover

Edited from "Depth of the ocean" by kraft2727. Light rays are dispersed by the waves, much like photon beams are dispersed by MRI receive arrays. This thesis aims to "calm the ocean" with radiolucent receive arrays.

See without being seen

PhD Thesis, Utrecht University, The Netherlands
Stefan Emiel Zijlema (2022)

Manuscript

Layout: S.E. Zijlema
Typesetting: \LaTeX 2 ϵ
Printed by: Ridderprint BV
ISBN: 978-90-393-7469-6

Copyright

© S.E. Zijlema
© IOP Publishing Ltd (Chapter 2 and 3)
© kraft2727 / Adobe Stock (Cover photo)

Funding

This work is part of the research program HTSM with project number 15354, which is financed by the Netherlands Organization for Scientific Research (NWO) and Philips Healthcare.

Financial support for publication of this thesis was kindly provided by NWO, Chipsoft, and Elekta.

See without being seen
Novel, radiolucent MRI receive arrays for
MR-linac and PET/MRI

Zien zonder gezien te worden
Nieuwe, radiolucente ontvangstspoelen voor MR-linac en PET/MRI
(met een samenvatting in het Nederlands)

Proefschrift

ter verkrijging van de graad van doctor aan de Universiteit Utrecht op gezag
van de rector magnificus, Prof. dr. H.R.B.M. Kummeling, ingevolge het besluit
van het college voor promoties in het openbaar te verdedigen op
donderdag 9 juni 2022 des middags te 12:15 uur

door

Stefan Emiel Zijlema

geboren op 18 augustus 1993
te Apeldoorn

Promotoren: Prof. dr. ir. C.A.T. van den Berg
Prof. dr. ir. J.J.W. Lagendijk

Copromotor: Dr. ir. H.N. Tijssen

Voor opa Joop[†]

Contents

List of Acronyms	I
1 Introduction	1
2 Design and feasibility of a flexible, on-body, high impedance coil receive array for a 1.5 T MR-linac	13
3 Improving the imaging performance of the 1.5 T MR-linac using a flexible, 32-channel, on-body receive array	35
4 A mask-compatible, radiolucent, 8-channel head and neck receive array for MRI-guided radiotherapy treatments and pre-treatment simulation	51
5 Minimizing the need for coil attenuation correction in integrated PET/MRI at 1.5 T using low-density MR-linac receive arrays	69
6 Summary and Discussion	87
7 Samenvatting	97
Bibliography	101
Publications	111
Dankwoord	115
Curriculum Vitae	119

List of Acronyms

3D	Three-dimensional
4D	Four-dimensional
AC	Attenuation correction
ADC	Apparent diffusion coefficient
AP	Anterior-posterior
bSSFP	Balanced steady-state free precession
CT	Computed tomography
DWI	Diffusion weighted imaging
EBRT	External beam radiotherapy
EPI	Echo planar imaging
EPID	Electronic portal imaging device
FH	Feet-head
FOV	Field of view
GE	Gradient echo
g-factor	Geometry factor
H&N	Head and neck
HIC	High impedance coil
LIC	Low impedance coil
Linac	Linear accelerator
LR	Left-right
MLC	Multi-leaf collimator
MRI	Magnetic resonance imaging
MRIGRT	MRI-guided radiotherapy
MRL	Magnetic resonance imaging – linear accelerator
M2D	Multiple 2D
MS	Multislice
MU	Monitor units
NCM	Noise correlation matrix
OAR	Organ at risk
PET	Positron emission tomography
PI	Parallel imaging

PSF-TOF Point spread function - time-of-flight

QA Quality assurance

RF Radiofrequency

ROI Region of interest

sCT Synthetic computed tomography

SENSE Sensitivity encoding

SNR Signal-to-noise ratio

TPS Treatment planning system

TSE Turbo spin echo

VMAT Volumetric arc therapy

VOI Volume of interest

CHAPTER 1

Introduction

1.1 Image-guided radiotherapy

Cancer is the leading cause of death in the Netherlands (CBS, 2020) and treatment with radiation therapy is indicated for 50% of cancer patients globally (Delaney et al., 2005). Radiotherapy, or radiation therapy, tries to damage and kill malignant tissue using ionizing radiation. The radiation damages the cell's DNA, which leads to cell death if the delivered dose is sufficiently high. Radiotherapy is based on two concepts: (1) the delivery of a high dose to the tumor, while the dose to the healthy tissue is kept as low as possible, and (2) the fact that healthy tissue recovers slightly better than malignant tissue.

Dose can be delivered to the tumor in several ways. For example, brachytherapy uses radioactive sources that are inserted directly into the malignant tissue, which minimizes the dose to the healthy tissue, but is highly invasive. This work focuses on another dose delivery method, namely external beam radiotherapy (EBRT), where radiation originates from a source outside the body. Photon radiation is mostly used and can be emitted from a radioactive source, such as Cobalt-60, or produced by a linear accelerator (linac).

EBRT is not invasive but radiation passes through healthy tissue before reaching the tumor, thereby damaging these tissues as well. To reduce toxicity from large doses to healthy tissue, radiation beams are administered from multiple angles so that the tumor is struck by all beams, while each beam passes through different parts of the healthy tissue. This leads to a spatially focused dose in the target while the dose in healthy tissue is minimized. Furthermore, each beam is optimized to minimize the dose to healthy tissues. EBRT devices have a multileaf collimator (MLC) that consists of metal 'leaves' that can move into the beam path and alter the beam's shape by partially blocking it. This way, the shape of the beam can match the shape of the target volume for an optimal dose distribution. Finally, a full treatment is delivered in so-called fractions over the course of several days or weeks, which allows the healthy tissue to recover before the next fraction is delivered (Hoskin, 2012).

A specialized treatment planning system (TPS) is used to calculate how (much) radiation should be delivered to achieve the prescribed dose in the target volume and which machine settings will spare the healthy tissue and organs at risk (OARs) as much as possible. There is a large range of parameters that can be tweaked, such as the MLC positions, beam angles, beam intensity, and beam duration.

1.1.1 Imaging for radiotherapy treatment planning

The TPS requires 3D imaging information of each patient to optimize all parameters. Traditionally, a CT scan has been used to obtain high-resolution, 3D electron density information of a patient and other structures in the beam path, such as immobilization devices. This information is then used by the TPS to simulate the delivered dose of a certain beam, e.g. using Monte Carlo engines (Purdy, 1992). For more information about treatment planning, the reader is referred to Xia et al. (2018).

Even more importantly, the treatment planning CT scan can also be used for the delineation of target volumes and OARs, which are used by the TPS for dose optimization. However, soft-tissue anatomy and malignancies are often not distinguishable on CT images. Therefore, scans with other imaging modalities are added in the pre-treatment phase, such as magnetic resonance imaging (MRI) or positron emission tomography (PET).

MRI uses magnetic fields and radiofrequency pulses to visualize the whole anatomy with a much better soft-tissue contrast than CT. Additionally, MRI allows for easy tailoring of contrast between tissue types and is therefore very versatile.

PET uses radioactive tracers that are injected into the patient to visualize metabolic activity. For example, fluorodeoxyglucose (FDG) accumulates most in active tissues with a high glucose consumption, such as tumor tissues and the brain. This way, regions with increased uptake can be visualized using photon-sensitive detector arrays around the patient.

In the treatment planning process, the scans of all imaging modalities are spatially aligned so that their information can be combined. Delineation of volumes of interest (VOIs), such as target volumes, is often performed on MRI images, as its soft-tissue contrast is best, while some OARs can also be delineated on the CT. PET can be used to highlight active tumor tissue or assess lymph node involvement and can thereby improve the accuracy of the delineations on MRI or CT. The final delineations are then used to calculate the optimal treatment plan.

Unfortunately, there are several sources of uncertainty in this process. Although daily patient positioning is performed as carefully as possible, imaging information from the planning stage will never perfectly match the internal anatomy at each treatment day (inter-fraction motion). Especially for obese patients daily positioning can be difficult (Moszyńska-Zielińska et al., 2014). The anatomy also changes *during* dose delivery, e.g.

due to respiration (intrafraction motion). Additionally, tumors often have microscopic tumor spread that is not visible on the aforementioned imaging modalities (ICRU 50, 1993). These three effects, amongst others, are traditionally compensated for by adding margins around the target volumes. These margins can be up to 10-15 mm for very mobile regions to ensure that the tumor will receive its prescribed dose (Ekberg et al., 1998; ICRU 62, 1999). However, larger margins will also lead to higher doses in surrounding healthy tissues, which can result in more severe side effects (van Herk, 2004). It is therefore essential to reduce these margins as much as possible.

1.1.2 MRI-guided radiotherapy

More recently, MRI capabilities have become available during treatments with the introduction of hybrid MRI-radiotherapy machines (Fallone, 2014; Keall et al., 2014; Legendijk et al., 2014; Mutic & Dempsey, 2014). One of these machines for MRI-guided radiotherapy (MRIGRT) is the Elekta Unity MR-linac, which combines a 1.5 T MRI scanner with a 7 MV linac (Figure 1.1). The availability of MR imaging during each treatment fraction allows for pre-beam plan adaptation based on the daily anatomy, or even tracking of the anatomy during the treatment with beam-on imaging. The latter allows for temporary interruptions of the beam (gating) when the anatomy of



Figure 1.1 The 1.5 T Elekta Unity MR-linac. This hybrid machine combines an MRI scanner (1) and a linear accelerator (2). The MRI receive hardware consists of a 4-channel anterior element (3) and 4-channel posterior element that is located in the middle of the bore under the table (4). Image adapted from Elekta (2018).

interest moves outside the beam path. When 3D imaging is available, retrospective dose accumulation is possible to validate the delivered dose and allow for adaptations in the next treatment fraction (Kontaxis et al., 2020). Moreover, anatomy tracking has the potential to make real-time treatment adaptations possible (real-time adaptive MRIGRT), e.g. via beam steering to follow the target volume over time (Glitzner et al., 2019; Uijtewaal et al., 2021). All these techniques aim to increase the accuracy of the dose delivery by reducing treatment uncertainties. Consequently, margin reductions may be possible, which will reduce the dose to healthy tissues.

Pre-beam scans for MRIGRT are usually high-resolution scans that take several minutes but tracking sequences must be much faster. Scans of the thorax or abdomen may only take around 200 ms (≥ 5 Hz) in order to resolve respiratory motion (Keall et al., 2006). Anatomy tracking therefore requires very fast imaging with low latencies (Borman et al., 2018) and fast reconstructions (Borman et al., 2019). Currently, the MR-linac is able to achieve such speeds for 2D slices but extension to 3D would open the door to aforementioned retrospective dose analyses and real-time treatment adaptations. The following section explains why 3D tracking is currently not possible, how MRI receive hardware can be built to accelerate 3D imaging, and why radiation complicates the hardware's design.

1.2 MRI and Coils

As mentioned before, MRI uses magnetic fields and radiofrequency pulses to visualize the anatomy. The exact mechanisms of the MRI signal generation and detection are not covered here. Excellent books have been written about the origin of the MRI signal to which the reader is referred (Dale et al., 2015; Haacke et al., 1999; McRobbie, 2003; Webb & Balcom, 2016).

1.2.1 Receive coils

The MRI signal is picked up by receive coils, or loops, that are placed on top of or close to the subject. The simplest receive coil is a single loop that consists of a (copper) conductor that is tuned to the resonance frequency with tuning capacitors. Multiple capacitors are generally placed in series around the loop (segmentation) to reduce noise arising from losses due to electric fields (Vaughan & Griffiths, 2012). A single loop, however, will have a limited field of view (FOV). Therefore, arrays of loops were proposed to increase the FOV. Interestingly, Roemer et al. (1990) found that the signals from an array of multiple individually connected loops can be combined to increase the signal-to-noise ratio (SNR) compared to a single loop that covers the same area. A limitation of this approach is that the SNR of a loop is highest at a depth that is approximately equal to the diameter of the loop, i.e. smaller loops will have their optimal SNR at a smaller depth and will have a reduced penetration depth. Consequently, the channel count cannot be increased infinitely by reducing loop sizes, as the SNR can suffer from an inadequate penetration

depth. Ideally, receive arrays surround the anatomy of interest to allow for placement of a large number of channels, while loops are still large enough.

Within a coil array, loops can interact with neighboring loops (coupling) and thereby significantly reduce each other's performance. The electromotive force (EMF) that is generated in each loop (the MRI signal) induces a current in the loop that subsequently induces a secondary field. This field is then detected by neighboring channels, which has a negative impact on their performance (Haacke et al., 1999). This effect becomes more problematic when a larger number of (small) loops is used. The coupling effect can be largely resolved by partially overlapping the loops to eliminate the mutual inductance and by connecting all loops individually to low input impedance preamplifiers (Roemer et al., 1990). The former is a precise and tedious process and requires a robust support structure to avoid (relative) shifts of loops and consequent increased coupling.

1.2.2 High impedance coils

Up to this point, a traditional type of coil is described, which is referred to as a low impedance coil (LIC). The EMF experiences a low impedance, which allows relatively high currents to be induced in these coils. These currents induce large secondary fields that worsen the aforementioned channel coupling issues. More recently, Zhang et al. (2018) proposed high impedance coils (HICs), which use a coaxial cable of which the shield and port are interrupted (Figure 1.2). HICs do not require tuning capacitors along the loop and instead use the distributed capacitance of the coaxial structure for tuning. Their design and mechanisms have significant advantages over LICs. In HICs, the EMF experiences a high impedance on the outer shield, which reduces currents and consequent secondary fields here. Currents on the inner conductor are relatively high but are 'shielded' from the sample and neighboring channels by the HIC's shield, which results in low inter-channel coupling compared to LICs (Ruytenberg et al., 2020). Residual inductive coupling with direct neighbors is still resolved with partial overlap of neighboring loops but the manufacturing process of an HIC array is strongly simplified compared to LIC arrays. Overlapping is less critical and the HIC's performance is relatively robust against shape changes of the loop, which together enable the use of support structures that are not rigid. Consequently, flexible HICs can be used, which allow for imaging of difficult or mobile anatomies, such as the wrist, hand, or knee (Zhang et al., 2018). HICs offer these advantages while the SNR remains approximately equal to the SNR of LICs (Ruytenberg et al., 2020; Zhang et al., 2018).

1.2.3 Accelerating MRI

As discussed before, multi-channel receive arrays are useful to scan larger FOVs and can improve the SNR. One important feature has not been discussed yet: multi-channel arrays can be employed to significantly reduce scan times using parallel imaging (PI) techniques, such as SENSE or GRAPPA (Griswold et al., 2002; Pruessmann et al., 1999). These PI techniques can reconstruct images with fewer data, thus reducing acquisition times. Without PI techniques, sampling fewer data points, i.e. below the Nyquist limit,

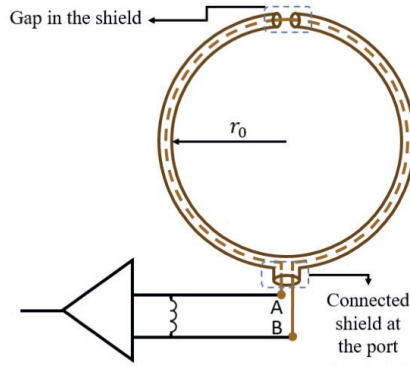


Figure 1.2 Design of a HIC. The HIC consists of a coaxial structure with an interrupted central conductor at the port side and an interrupted shield on the opposite side. Adapted from Mollaei et al. (2020).

leads to an aliased image with a reduced field of view (FOV) but PI techniques use the spatial sensitivity information of all channels to unfold the image to reconstruct an alias-free image. However, as fewer data are acquired, this process does reduce the SNR as follows:

$$SNR_{PI} = \frac{SNR_{full}}{g\sqrt{R}},$$

where SNR_{PI} and SNR_{full} are the SNR of the PI and fully sampled acquisitions, respectively. The g -factor in the denominator is the geometry factor, which is a measure of the (spatially varying) noise amplification due to the PI's data unfolding process. In general, more channels result in stronger spatial encoding, a lower g -factor, and thus a higher potential acceleration factor R . Hence, there is a trend towards receive arrays with a high channel count. However, as noted before, smaller channels can eventually reduce the SNR when their penetration depth is inadequate.

1.2.4 Receive arrays for MRIGRT

Over the years, vendors and researchers have designed, optimized, and manufactured a wide range of receive arrays to optimize the MRI performance in terms of SNR and acceleration performance. Unfortunately, these conventional receive arrays are not compatible with MRIGRT, although the MRI scanner inside the MR-linac has the same magnetic field strength as many conventional scanners, i.e. 1.5 T.

This incompatibility is caused by the fact that the receive array of an MR-linac is, by definition, in the beam path, as MRI sensitivity is especially important in and around the target volume(s). Traditional receive arrays were not designed for the MRIGRT application and therefore have electronics distributed over their surface that attenuate the beam severely, i.e. up to tens of percents for a single beam. The TPS can correct

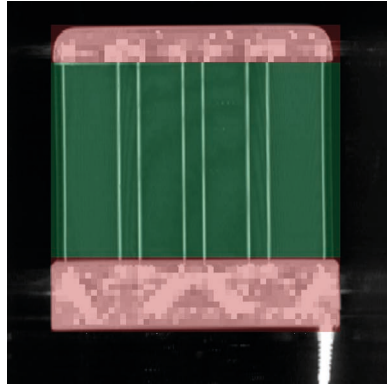


Figure 1.3 CT projection image (MIP) of an MR-linac receive array. The radiolucent window (green) is approximately 30 cm high and contains no electronics, except conductors for signal reception. All electronics are moved to the feet and head sides (red). Image from Hoogcarspel et al. (2018). Reproduced by permission of IOP Publishing.

for most of this attenuation, albeit only when the array's position is known, but some of the electronics may not be radiation resistant and could be damaged when irradiated. Therefore, receive arrays for MRIGRT have been redesigned to have a radiation transparent, or radiolucent, window (Figure 1.3). This region contains no electronics and attenuation is low.

The current clinical array of the 1.5 T MR-linac (Figure 1.1) indeed features such a radiolucent window. Additionally, the anterior element of the array is elevated above the patient to avoid an increased skin dose (Hoogcarspel et al., 2018). When an object is placed directly on the patient, a so-called buildup effect occurs, as secondary electrons are generated in the object and deposit their dose at the surface of the subject, which can result in skin burns. However, when the array is elevated above the patient, the negatively charged electrons are curved away by the Lorentz force from the perpendicular magnetic field before they reach the patient (Raaijmakers et al., 2005). This effect is visualized in Figure 1.4.

Dosimetrically, the clinical array thus suffices. However, imaging performance is reduced compared to conventional arrays. This is caused by the limited channel count (8) with respect to most conventional arrays (20-32), which reduces acceleration performance (and possibly SNR). Moreover, these channels are positioned several centimeters from the patient, which reduces its sensitivity. The 4-channel posterior element is placed in the middle of the bore under the table, while the 4-channel anterior element is attached to a coil bridge that is placed over the patient and holds the element in a fixed position above the patient (Figure 1.1). Finally, the performance of the individual loops is not optimal, as tuning capacitors can only be placed in the electronics regions of the array (Figure 1.3). Normally, more capacitors are distributed over the

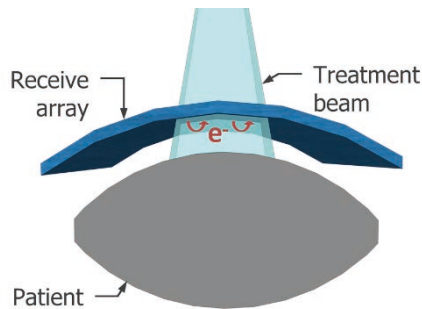


Figure 1.4 Mechanism of reducing the skin dose by elevating the receive array. The beam from above induces secondary electrons in the receive array, which are curved away by the Lorentz force before depositing their dose into the skin of the patient. Image from Zijlema et al. (2019a). Reproduced by permission of IOP Publishing.

conductor's path to limit signal losses (see section 1.2.1). However, as this is not possible in the radiolucent window, the performance of the individual elements is reduced.

With the current array, tracking sequences are restricted to 2D or low-resolution 3D, which limits the potential applications. Therefore, new, radiolucent receive arrays are needed that feature more channels and are placed closer to the patient, so that the imaging performance can be increased.

1.2.5 Receive arrays for head and neck radiotherapy

Similarly to body imaging in the previous sections, conventional, beam-attenuating arrays cannot be used for MRIGRT of the head and neck (H&N) region. Therefore, the body array of the 1.5 T MR-linac is currently used for MRIGRT in the H&N, even though this array has a poor fit and relatively low sensitivity in this region. Even worse, the conventional, close-fitting arrays cannot be used in the pre-treatment simulation stage either. The devices that are used for reproducible patient positioning in H&N radiotherapy, i.e. thermoplastic immobilization masks, hamper the use of conventional arrays due to their shape and size. Current clinical MRI setups for the simulation phase therefore often consist of (multiple) receive arrays with suboptimal geometries and coil positions (Figure 5), which result in a poor fit of the anatomy, i.e. a low filling factor (Mandija et al., 2019; Verduijn et al., 2009). Consequently, the signal-to-noise ratio (SNR) and acceleration performance are relatively low.

Hence, both the pre-treatment and treatment setups are currently suboptimal. Ideally, a dedicated H&N array would exist that has a close fit to the anatomy and is mask- and radiation-compatible so that the same array can be used for MRI-simulation and MRIGRT in treatment position.



Figure 1.5 Clinical setup for MRI-simulation before H&N radiotherapy. The setup consists of two loop coils against the head and a 16-channel anterior element on a coil bridge that is placed against the chin.

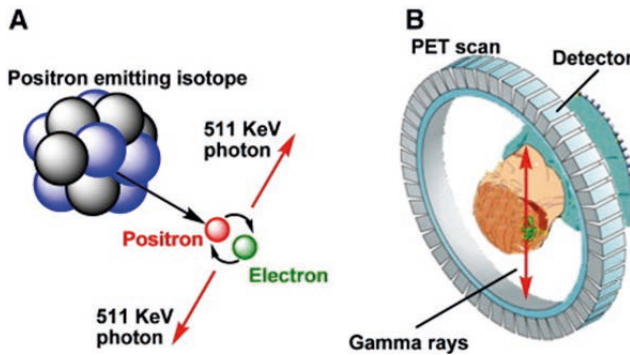


Figure 1.6 (a) Radioactive tracer emits positrons, which annihilate with a nearby electron. Two 511 keV photons are emitted at a 180° angle. (b) Both photons are detected by a PET detector array around the subject. Image adapted from Li and Conti (2010) with permission from Elsevier.

1.2.6 Receive arrays for PET-MRI

Interestingly, many similarities exist between coil requirements for MRIgRT and PET/MRI. As noted before, PET uses radioactive tracers to visualize metabolic activity. The radioactive tracers emit positrons, which react with a nearby electron in a process called positron-electron annihilation. The result of this reaction is the emission of two photons with an energy of 511 keV (Figure 5). These two photons are detected by a PET detector ring around the subject, from which the location of the annihilation can be pinpointed. For a more extensive and detailed explanation, the reader is referred to Cherry et al. (2012) and Wahl and Beanlands (2008).

The combination of PET and MRI allows for simultaneous acquisition of metabolic and anatomical information, respectively. Objects that are in the photon path, such as

MRI receive arrays, can attenuate photons or alter their path. Therefore, attenuation correction (AC) is performed in the reconstruction process to compensate for these effects. However, similarly to MRIGRT, AC is not possible for on-body (surface) MRI receive arrays¹, as their exact position is unknown. This can result in significant PET reconstruction errors (Fürst et al., 2014; Wollenweber et al., 2014). These are unacceptable for quantitative measurements, such as treatment response assessment or dose reconstructions of radioembolization treatments (Bastiaannet et al., 2018; Braat et al., 2018). Moreover, the resulting reconstruction errors could result in misdiagnoses, e.g. when the signal of a small lesion, such as a metastasis, is reduced such that the signal is lost in the noise, or when a patient's treatment response is wrongly classified due to a lower measured activity (Wahl et al., 2009).

Clearly, PET/MRI receive arrays have similar radiolucency requirements as MRIGRT, although the photon energy is different between the two: 511 keV versus a ~7 MV spectrum for MRIGRT. The lower photon energy of PET may increase photon attenuation of a certain array with respect to MRIGRT.

1.3 Thesis outline

This thesis aims to present designs and performance characteristics of novel, radiolucent receive arrays for MRIGRT and PET/MRI. The MRI receive array plays an important role in the imaging speed and image quality that can be achieved on a certain machine, such as the MR-linac. Therefore, the design needs to be optimized for imaging capabilities but must remain compatible with its application (MRIGRT).

The current clinical array of the 1.5 T MR-linac features a radiolucent window with low attenuative properties to be compatible with MRIGRT but its design is not fully optimized for imaging performance. The array is rigid, placed several centimeters from the body, and only features 8 channels. These properties limit the speed and quality of the pre-beam and beam-on imaging. In **Chapter 2**, the design of an improved MRIGRT array is proposed. The proposed array is placed directly on-body to achieve optimal SNR. HICs are used to give the array its flexible properties, limit inter-channel coupling, and make its radiolucent design possible, as their lack of tuning capacitors allows for channel placement in a double row layout without (large) dose disturbances. Simple prototypes are benchmarked and potential issues of the design, such as an increased surface dose or beam attenuation, are investigated.

Based on this design, a full 32-channel array was manufactured. **Chapter 3** describes the building process of this array and compares its imaging performance against the current clinical array. Furthermore, its radiolucency is quantified, i.e. its impact on a treatment beam.

¹ Technically, AC is possible but all methods that attempt to correct for flexible arrays have major disadvantages or limitations. For more information, see section 5.1.

Thus far, only body arrays were considered. However, other sites may benefit even more from the flexible properties of HICs, in particular the head and neck (H&N) region. The geometry of this anatomy varies heavily between subjects and has relatively sharp curves. Similarly to the body arrays, conventional H&N arrays are incompatible with MRIGRT. Additionally, an immobilization mask is used to restrict patient movement for more precise treatments. In **Chapter 4**, an 8-channel MRIGRT receive array for H&N is developed, which is compatible with immobilization masks and is flexible so that it follows the shape of the anatomy.

All aforementioned MRIGRT receive arrays were designed to be radiolucent to reduce dose changes during treatments. However, photon radiolucency is similarly important in simultaneous PET/MRI, where attenuation by the MRI receive array can lead to significant reconstruction errors when no attenuation correction (AC) is performed. As dedicated, radiolucent PET/MRI receive arrays are scarce, can MRIGRT arrays be used for this purpose? In **Chapter 5**, this question is answered for two MR-linac arrays: the 8-channel clinical array and the 32-channel prototype array.

Finally, the most important findings of this thesis are summarized and discussed in **Chapter 6**. The chapter ends with suggestions for further research.

CHAPTER 2

Design and feasibility of a flexible, on-body, high impedance coil receive array for a 1.5 T MR-linac

The following chapter is based on:

Zijlema, S. E., Tijssen, H. N., Malkov, V. N., Dijk, L. van, Hackett, S. L., Kok, J. G. M., Lagendijk, J. J. W., & van den Berg, C. A. T. (2019). Design and feasibility of a flexible, on-body, high impedance coil receive array for a 1.5 T MR-linac. *Physics in Medicine & Biology*, 64(18), 185004.

Abstract

Introduction The lack of radiation-attenuating tuning capacitors in high impedance coils (HICs) make HICs an interesting building block of receive arrays for MRI-guided radiotherapy (MRIGRT). Additionally, their flexibility and limited channel coupling allow for low-density support materials, which are likely to be more radiation transparent (radiolucent).

Purpose In this work, we introduce the use of HICs in receive arrays for MRIGRT treatments. We discuss the design and show the dosimetric feasibility of a HIC receive array for on-body placement, which has a high channel count and aims to improve the imaging performance of the 1.5 T MR-linac.

Methods Our design comprises an anterior and posterior element, which each feature a 2×8 channel layout (32 channels total). The anterior element is flexible, while the posterior element is rigid to support the patient. Mockups with support materials and conductors were built, irradiated, and optimized to minimize impact on the surface dose and dose at depth. Functional, single-channel HIC imaging prototypes and a 5-channel array were built to assess the performance in terms of signal-to-noise ratio (SNR). The performance was compared to the clinical MR-linac array.

Results Surface dose increases were minimized to 7% of the dose maximum. At 10 cm depth, dose changes were limited to $\leq 0.8\%$ under a single conductor and $\leq 1.4\%$ under a conductor crossing. This dose change will be further minimized by anatomical motion and the use of multiple beam angles. The 5-channel imaging prototype outperformed the clinical array in terms of SNR and channel coupling. Imaging performance was not affected by the radiation beam.

Conclusions The use of HICs allowed for the design of our flexible, on-body receive array for MRIGRT. The design was shown to be dosimetrically feasible and improved the SNR. Future research with a full array will have to show the gain in parallel imaging performance and thus acceleration.

2.1 Introduction

Several hybrid MRI-radiotherapy systems have been developed in an effort to improve radiation therapy treatments, i.e. to ensure tumor coverage and minimize toxicity, using MRI to monitor positions of mobile tumors and organs at risk (Fallone, 2014; Keall et al., 2014; Lagendijk et al., 2014; Mutic & Dempsey, 2014). However, MRI is known to be inherently slow. Long acquisition times lengthen preparatory (pre-beam) imaging and limit real-time anatomy monitoring to 2D planes or low-resolution 3D volumes. A receive array with a high channel count can overcome this limitation by enabling the use of high undersampling factors through its increased parallel imaging (PI) capabilities (Breuer et al., 2005; Larkman et al., 2001; Pruessmann et al., 1999).

The 1.5 T Elekta MR-linac (Unity, Elekta AB, Stockholm, Sweden) is equipped with a clinical receive array that consists of two 4-channel elements, which are positioned centimeters away from the anatomy: the anterior element is elevated above the patient and the posterior element is positioned under the table (Hoogcarspel et al., 2018). The limited channel count, combined with the 1×4-channel arrangements and distant positioning, limits the signal-to-noise ratio (SNR) and PI performance in all planes.

A dense¹, on-body receive array for the MR-linac could considerably improve the imaging performance, both during the preparatory pre-beam phase, as well as during irradiation. However, the design and on-body placement of such an array are not trivial, as the radiation beam passes through during treatments, which has two major dosimetric consequences. Firstly, the array may function as bolus and increase the patient's surface dose (Ghila et al., 2016). The surface dose of patients is currently minimized by the elevated design of the clinical array. The elevation allows most secondary electrons that are generated in the coil materials, to be bent off by the magnetic field before they reach the patient's skin (Raaijmakers et al., 2005). This so-called electron return effect (ERE) will not reduce the surface dose when dense coil materials are placed directly onto the patient, as the electrons have no space to curve back. A second dosimetric consequence of the receive array is that its electronics and support materials could cause local attenuation of the treatment beam (Hoogcarspel et al., 2013). A large region in the center of the array is required that does not attenuate the beam, i.e. a radiolucent window. However, conventional, low impedance coils (LICs) use multiple capacitors that are distributed over the loop (Vaughan et al., 1994), which would attenuate the treatment beam due to their dense structure. The current clinical array solves this issue by restricting the amount of capacitors per loop to two and placing these on the cranial and caudal sides outside the radiolucent window. However, when a second row would be added to maximize the number of channels, only one capacitor can be placed per coil, which, combined with the smaller loop sizes, will lead to severe channel coupling. Unlike LICs, the recently proposed high impedance coils (HICs) do not require capacitors in the loop (Zhang et al., 2018). Instead, the distributed capacitance of the

1. A dense array is a coil engineering term that refers to an array with a large number of channels that densely cover a surface. It should not be confused with a high mass or electron density.

coaxial conductor is used for tuning. Zhang et al. showed that HICs can be very flexible and exhibit limited coupling interactions with neighboring loops. A HIC receive array therefore requires less-critical overlap optimization than LICs to achieve the optimal imaging performance and consequently does not demand dense support materials to firmly secure the geometry. This will be beneficial for the array's radiolucency and thus makes HICs an attractive building block of a radiolucent receive array for MRI-guided radiotherapy (MRIgRT).

In this work, we introduce the use of HICs in receive arrays for MRI-guided radiotherapy treatments and discuss the design and feasibility of a dense HIC receive array for on-body placement to improve the imaging performance of the 1.5 T MR-linac. The anterior element is flexible in order to closely match the body contour of all patients. The posterior element is placed directly under the patient for optimal imaging sensitivity. The full array allows for the use of up to 32 channels. All aspects of the design are optimized to minimize the impact on the radiation therapy, e.g. the composition and thickness of the support materials and conductors. Ideally, its impact is kept as low as possible. This way, the array does not require inclusion in the treatment planning system (TPS) or tracking of the dynamic position over time, which greatly simplifies its use. Finally, functional, single-channel and 5-channel prototypes are built and the gain in SNR from our on-body approach is quantified with respect to the current clinical array, both with and without a radiation beam enabled.

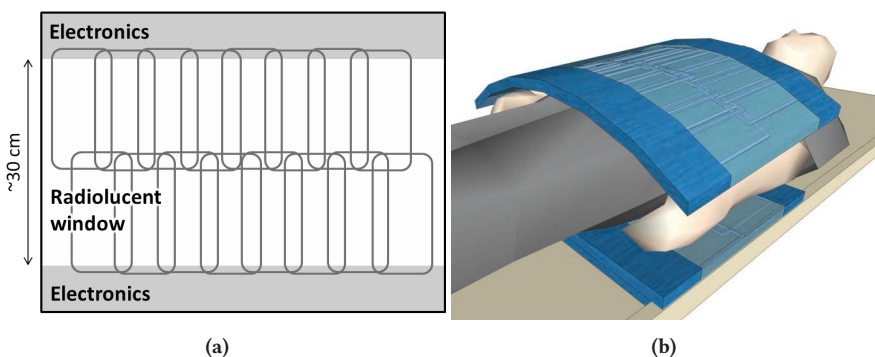


Figure 2.1 (a) Proposed element design featuring a double-row layout and 30 cm radiolucent window. The radiolucent window contains only loops and support materials. Electronics, i.e. matching and detuning circuitry, are all placed outside this window. No data or power lines cross the radiolucent window. (b) Render of the full array on a patient.

2.2 Methods

2.2.1 Proposed design

Major changes are made to the coil design with respect to the clinical array (Figure 2.1). Flexible HICs are used instead of LICs. The anterior element is no longer rigid and elevated, but is placed on the patient and can bend to fit any anatomy. The posterior element is placed on the table, directly under the patient. The single-row layout is replaced by a double-row layout, which will provide extra spatially varying coil sensitivities in the feet-head direction for enhanced parallel imaging capabilities. This will require cable outputs on two sides of the array (feet and head) and consequently both ends of the bore, as the data and power cables cannot run through the radiolucent window. Each channel can be connected with a coaxial cable to an in-house developed interface box on the table, which performs preamplification and digitization of the signal. From here, the data are transferred to the system via an optical fiber. The final anterior and posterior element will comprise 16 channels each, totaling 32 channels when both elements are used simultaneously (Table 2.1).

Support materials of the array were chosen to have a low mass density, which is expected to lead to a low electron density and thus a low dosimetric impact. The HIC's flexibility allows for the removal of sturdy, dense layers that are required for LICs to fix their relative positioning that is essential for minimizing channel coupling. This will allow easier bending of the array and improves radiolucency. The support material thicknesses were also optimized. For optimal sensitivity in the body, the coil loops should be as close to the patient as possible. However, as discussed before, dense loop materials can increase the surface dose. Here, the use of low-density foam between the loops and the patient is investigated to reduce this so-called bolus effect (Figure 2.2). The resulting distance is expected to allow the secondary electrons that are generated in the dense materials to be absorbed or bent off by the Lorentz force from the perpendicular magnetic field (Raaijmakers et al., 2005).

	Clinical array	Proposed design
Nr. channels (total)	8	32
Nr. channels per element	4	16
Nr. channels (RL)	4	8
Nr. channels (FH)	1	2
Single channel width (RL)	~128 mm	~90 mm
Single channel length (FH)	~440 mm	~190 mm

Table 2.1 Coil dimension comparison between the current clinical array of the 1.5 T MR-linac and the proposed design.

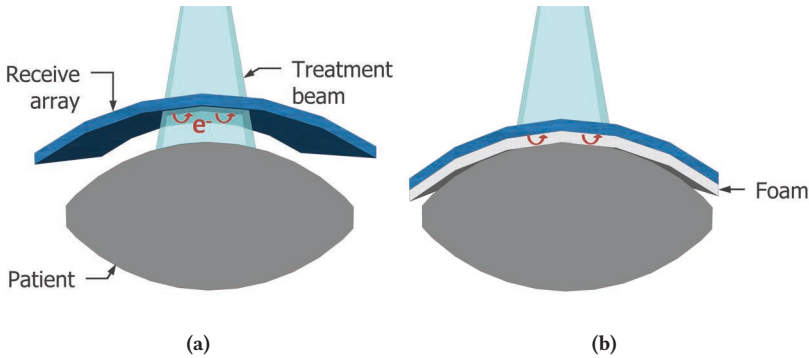


Figure 2.2 Curvature of secondary electrons (red arrows) from dense materials of an elevated array (left) and an on-body array (right) to reduce the bolus effect in a magnetic field. The elevated array allows electrons to curve away from the patient in air. On-body placement eliminates the air between array and patient and therefore requires a low-density foam layer where electrons can curve away from the patient.

2.2.2 Dosimetry

Above hypotheses, as well as the attenuation of the conductors, are dosimetrically investigated by quantifying the design's bolus effect at the surface and dose reduction at larger depths. Monte Carlo simulations were performed to investigate beam angulation effects.

2.2.2.1 Bolus effect minimization

Several mockups were manufactured to investigate and minimize the bolus effect. First, three mockups of the anterior element (mockups_{ant}) were created with varying foam thicknesses (Figure 2.3a/b). The low (electron) density foam serves as a spacer between the materials with high electron density (i.e., the conductors) and the patient's skin. Between the foam layers of the mockups, three candidate HIC coaxial cable types were placed with partially overlapping strands. AlphaWire (Elizabeth, NJ, USA) 9434 (ϕ 1.0 mm), AlphaWire 9432 (ϕ 1.1 mm), and RG178 (ϕ 1.8 mm) cables were used, of which the latter was also used by Zhang et al. (2018) for a flexible hand array. These will henceforth be referred to as wire_{1.0}, wire_{1.1}, and wire_{1.8}, respectively.

The mockups_{ant} were irradiated on a 1.5 T MR-linac with a 7 MV, 400 MU, 57×22 cm² field (Figure 2.3c) and a source-surface distance (SSD) of 142 cm. A GAFChromic (Ashland, USA) EBT-3 film (lot: 07181601) was placed at the surface and the dose was measured without a mockup ($D_{no\ mockup}$) and with the mockups placed directly onto the film (D_{mockup}). Films were scanned with an Epson Expression 10000XL flatbed scanner. Films were aligned and converted to dose with an in-house, clinically used tool. The

dose change ΔD was calculated with:

$$\Delta D = D_{mockup} - D_{no\ mockup}. \quad (2.1)$$

As a reference, the measurement was repeated with a gantry angle of 180° to see the bolus effect due to the treatment couch. The dose was corrected for the different beam characteristics.

2.2.2.2 Dosimetry at depth

Film dosimetry was found to be insufficiently accurate for a dosimetric comparison at depth, as inhomogeneities in the film were larger than the expected dose changes of a few percent or less. Instead, an Electronic Portal Imaging Device (EPID) was used to spatially quantify the dose changes with a high resolution (0.25×0.25 mm² pixels). The response of an aSi EPID panel has been shown to be linear with dose (Grein et al., 2002), thus the relative dosimetric impact of the mockups can be quantified. The correspondence between EPID signal and dose is validated using ionization chamber measurements in Appendix I.

All EPID imaging was performed on a conventional linac (Synergy, Elekta AB) without a magnetic field present so that the setup could be placed against the panel. Images were acquired with the XIS (PerkinElmer, Waltham, MA, USA) software package with an acquisition time of 433 ms per frame. A 100 MU 10×10 cm² 6 MV beam was delivered at a gantry angle of 90° with a dose rate of 250 MU/min. A 100-frame average was saved that covered the full beam delivery. All automatic corrections were disabled. A five-minute waiting step was employed between acquisitions to avoid ghosting effects. Measurements assessed the radiolucency of an optimized mockup_{ant} (Figure 2.3a) and of a posterior mockup_{pos} (Figure 2.3d), of which the latter featured non-flexible foam layers, as the array has to support the patient.

First, two reference images are acquired without mockup or phantom present to normalize the EPID response: an open flood-field image (I_{flat}) and a dark-field image without irradiation (I_{dark}). Subsequently, 100 mm solid water was placed against the EPID panel (SSD = 150 cm). EPID measurements were performed with and without placement of a mockup against the phantom. Prior to each acquisition, a new dark image was acquired (I_{dark_dyn}). The raw images (I_{raw}) were then processed with (McDermott et al., 2004):

$$I_{proc} = \frac{I_{raw} - I_{dark_dyn}}{I_{flat} - I_{dark}}. \quad (2.2)$$

The dose attenuation fraction due to the mockup (A_{EPID}) can then be found by simply calculating the relative change:

$$A_{EPID} = \frac{I_{proc, mockup} - I_{proc, no\ mockup}}{I_{proc, no\ mockup}}. \quad (2.3)$$

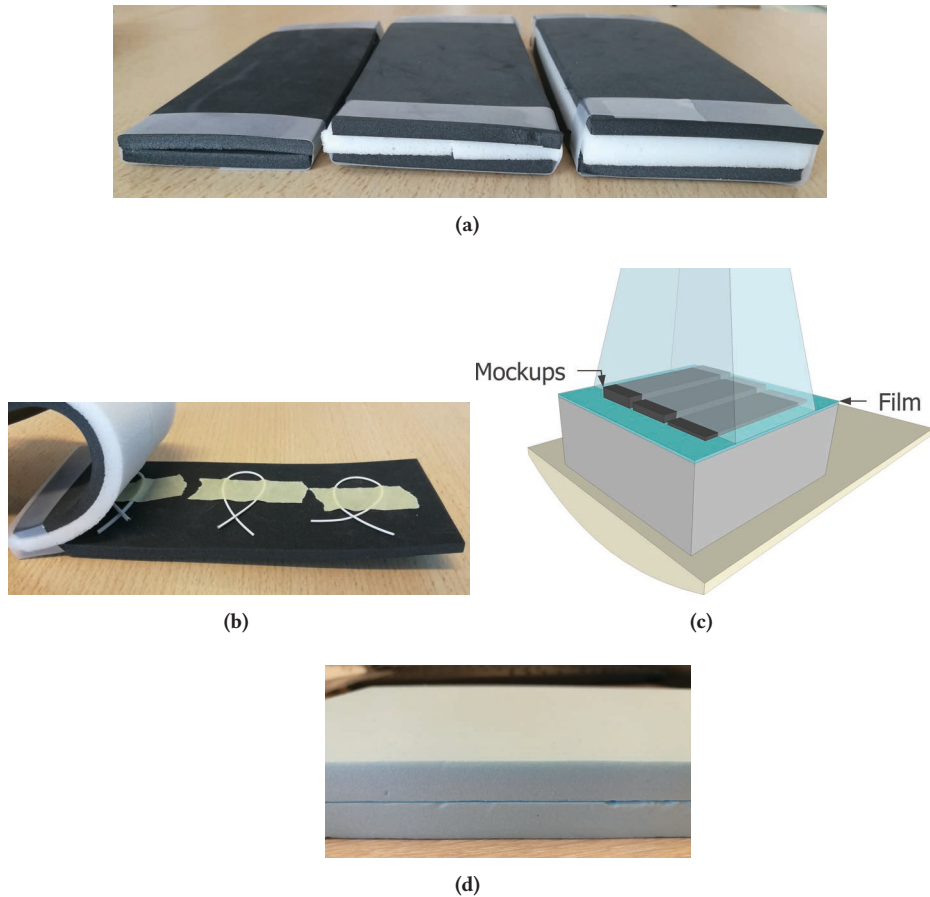


Figure 2.3 (a) Photo of the anterior mockups ($mockups_{ant}$) with varying foam thicknesses. Each mockup consists of the following layers (from top to bottom): 5 mm EVA-PE foam, partially overlapping strands of HIC cable, 0, 5, or 10 mm Flamex Basic (Merford, Gorinchem, NL) foam (9.5 kg/m^3), and 5 mm EVA-PE foam again. The conductor-to-surface distance consequently ranged from 5 to 15 mm. (b) Placement of the three HIC wires on the upper foam layer of the mockups. (c) Experimental setup of foam thickness optimization. A film was placed on a solid water volume and irradiated from gantry angle 0° in a 1.5 T MR-linac. Two films were irradiated, one with (D_{mockup}) and one without ($D_{no \text{ mockup}}$) the mockups. (d) Outside view of $mockup_{pos}$ consisting of three layers: 15 mm XPS, HIC cable, and 15 mm XPS.

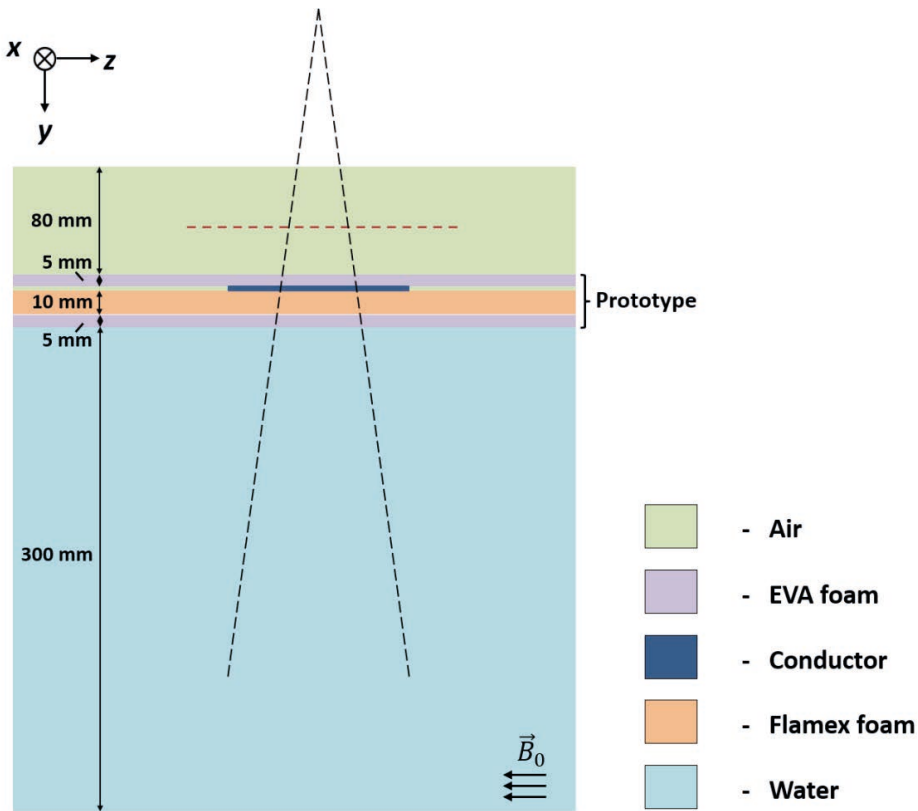


Figure 2.4 Schematic of the simulation setup with `mockupant` with corresponding dimensions. The beam enters from a 0° angle (dashed black line). The red dashed line shows the location of the phase-space scoring plane. Scoring regions were placed in the phantom at a depth of 0.134, 13, and 100 mm.

2.2.2.3 Monte Carlo simulations

Monte Carlo simulations were used to investigate the influence of angulated, non-perpendicular beams on the dose changes. Additionally, simulations were performed to translate the EPID measurements without a magnetic field to an expected dose change at 1.5 T. The correspondence between the EPID signal and the Monte Carlo simulations with and without a magnetic field is discussed in Appendix II.

Engine and beam characteristics

The `egs_chamber` application (Wulff et al., 2008) of the EGSnrc Monte Carlo package (Kawrakow & W.O. Rogers, 2000) was used for all simulations. The magnetic field transport is included using the enhanced electric and magnetic field macros (Malkov & Rogers, 2016). The electron and photon total energy cut-offs were set to 661 keV and

10 keV, respectively. The latest available Elekta-provided phase-space data for the 7 MV FFF Elekta Unity accelerator were used. These data define a $10 \times 10 \text{ cm}^2$ field at isocenter, located 143.5 cm away from the source and stores the particles in the phase space at 128.5 cm from the source. Both electrons and photons were provided in the phase-space and included in the simulation. For tilted beam simulations a photon spectrum is extracted from the phase-space and used instead.

Simulated setup

The receive array is modeled with the same composition as mockup_{ant} with a conductor-to-surface distance of 15 mm (Figure 2.3a). The dimensions and material compositions from the manufacturer's datasheets were used. The conductors are simulated as two perpendicular, straight coaxial cables that cross in the center. For practical reasons, only the wire_{1,1} prototype was simulated.

The simulated setup is shown in Figure 2.4. A $30 \times 30 \times 30 \text{ cm}^3$ water phantom is positioned with an SSD of 133.5 cm. An 8 cm layer of air is positioned on top in the simulations without prototype. When the prototype is present, it replaces the air in the region closest to the phantom. Simulations with a 1.5 T magnetic field are run with beams incoming at a 0° , $\pm 30^\circ$ and $\pm 55^\circ$ rotation around the z-axis. The rotation will cause a higher path length through the conductor, which is expected to increase the attenuation. Higher angles than 55° are unlikely, as the array will fold around the patient and thus most beams will hit the array approximately perpendicularly. The field sizes were set to be $10 \times 10 \text{ cm}^2$ in the isocenter.

Scoring and analysis

As the (surface) dose will vary greatly within the first mm, $1 \times 1 \times 1 \text{ mm}^3$ voxels will give an inaccurate representation of the surface dose. Therefore, a thin single voxel of dimension $20 \times 20 \times 0.028 \text{ mm}^3$ is analyzed at a depth of 0.134 mm to reflect the sensitive region of an EBT-3 film that is placed on top of a phantom. This way, the simulations can be compared to the experimental findings. At depth, two scoring regions are set up as $101 \times 101 \times 1$ matrices with 1 mm^3 voxels. The regions are positioned at 13 mm (D_{max}) and 100 mm depth in the water phantom. All simulations were performed with and without the prototype on the phantom and the relative change was calculated (A_{sim}).

2.2.3 Imaging

The imaging performance of single-channel prototypes and a 5-channel prototype array were investigated in this work. High-impedance coils ($\sim 9 \times 19 \text{ cm}^2$) were constructed from coaxial wire_{1,0}, wire_{1,1}, and wire_{1,8} and cable lengths were adjusted for resonance at 63.87 MHz (Zhang et al., 2018). The loops were connected to matching and detuning circuitry, which in turn connected to an interfacing box with the preamplification and digitization hardware. Bending of the loops around a phantom during bench tests did not affect the matching significantly ($< 1 \text{ dB}$) and should therefore not affect the imaging

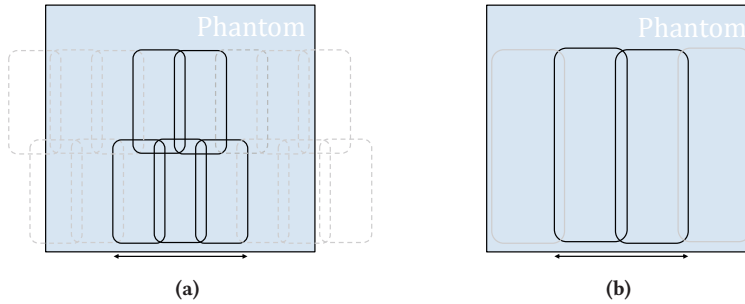


Figure 2.5 (a) Channel positions of the 5-channel prototype on a phantom. The dashed gray channels will be added to create the final 16-channel layout. (b) Channel positions of the clinical anterior element above a phantom. The two outer channels of the clinical array are disabled (gray). This resulted in a comparable phantom coverage of the two setups (black arrow).

performance. To assess the impact of channel coupling on the imaging performance, five wire_{1,1} loops were combined into an array (Figure 2.5a) and its performance was compared to the clinical anterior element with its two center channels enabled (Figure 2.5b), such that the phantom coverage of the two arrays was approximately equal.

All imaging was performed on a 1.5 T Elekta Unity MR-linac using a pelvis-sized phantom (PVP- and agar-based, 2.6% NaCl) with dielectric properties that are representative of a human body. Prototypes were placed onto the phantom on a 15 mm foam spacer. The anterior element of the clinical array was elevated 3 cm above the phantom, i.e. in treatment position.

For the single-channel prototypes, 2D spoiled gradient echo acquisitions (TR/TE = 30/4.0 ms, flip angle = 20°, FOV = 420×240 mm², voxel size = 3×3×10 mm³) were performed. For the multi-channel arrays, transverse and sagittal 3D spoiled gradient echo acquisitions (TR/TE = 30/4.0 ms, flip angle = 40°, FOV = 66×40×25 cm³, voxel size = 3×3×10 mm³) were performed. The raw k-space data were reconstructed using ReconFrame (Gyrotools, Zurich, CH). For the multi-channel acquisitions, sum-of-squares channel combination was performed. The SNR was calculated (Kellman & McVeigh, 2005) and used as a performance metric. Furthermore, channel coupling was quantified from the noise-only pre-scan by calculating the Pearson correlation coefficients.

Finally, the impact of the radiation beam on the SNR is investigated. Burke et al. (2010) described radiation-induced signal spikes in k-space when a receive array is irradiated, which can lead to a reduction in SNR. The effect of radiation was assessed for the wire_{1,1} single-channel prototype and a single channel of the clinical anterior element. A 50-dynamic spoiled gradient echo (TR/TE = 7.3/2.3 ms) acquisition was performed with and without a 15×15 cm² beam that crossed the loop. Under the assumption that the

signal from the phantom is stationary, we can use the time-course SNR as a metric for the SNR (Kellman & McVeigh, 2005; Sijbers et al., 1998). Radiation-induced spikes in k-space will disrupt the stationary signal and consequently lower the time-course SNR. Using the dynamic imaging series, we can calculate the SNR with:

$$SNR(x, y) = \frac{S_{mean}(x, y)}{\sigma(x, y)}, \quad (2.4)$$

where $S_{mean}(x, y)$ and $\sigma(x, y)$ are the mean and standard deviation of the magnitude pixel intensity over time at location (x, y) , respectively.

2.3 Results

2.3.1 Dosimetry

2.3.1.1 Bolus effect minimization

The dose without a mockup ($D_{no\ mockup}$) equaled 15% with respect to the dose maximum (D_{max}) at 13 mm. As expected, placement of the mockups_{ant} increases the surface dose, but the addition of low-density foam layers is shown to decrease the bolus effect from the dense materials (Figure 2.6). Here, d_{foam} represents the conductor-to-surface distance, as explained in Figure 2.3. An increase from 5 mm to 10 or 15 mm decreased the surface dose from 29% (directly under the conductor of $D_{mockup_{ant,5mm}}$) to 22% ($D_{mockup_{ant,10mm}}$ and $D_{mockup_{ant,15mm}}$) of D_{max} . In comparison, a posterior beam through the treatment couch more than doubled the surface dose to 40% of D_{max} .

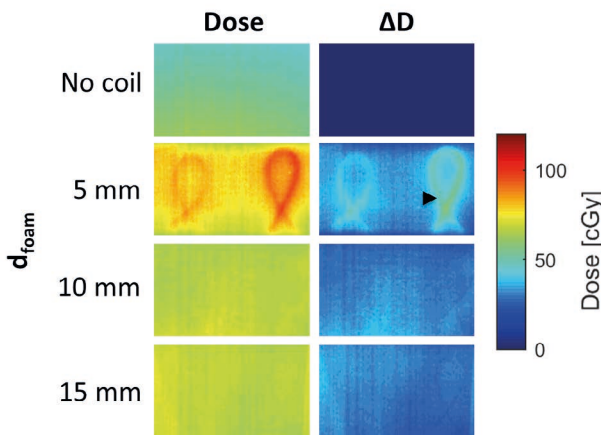


Figure 2.6 Left column: the measured surface dose on film for several foam thicknesses (d_{foam}). Right column: dose difference ΔD with respect to $D_{no\ mockup}$ (first row). Note that for 5 mm thickness the imprint of the loops is visible (black arrow).

Prototype	Attenuation (A_{EPID})
Support _{ant} only	-0.2 ± 0.1 %
Support _{pos} only	-0.4 ± 0.1 %
Support _{ant} + wire _{1,8} [single/double]	-1.4 ± 0.1 % / 2.8 %
Support _{ant} + wire _{1,1} [single/double]	-0.8 ± 0.1 % / 1.4 %
Support _{ant} + wire _{1,0} [single/double]	-0.8 ± 0.2 % / 1.3 %

Table 2.2 Dose attenuation fractions obtained by EPID measurements (A_{EPID}) due to the prototype materials at a depth of 10 cm. Results are shown for the support materials of anterior mockup_{ant} (support_{ant}) and posterior mockup_{pos} (support_{pos}), and attenuation fractions directly under the conductors. If applicable, the attenuation of a single wire and a double wire (crossing point) are both reported.

2.3.1.2 Dosimetry at depth

Table 2.2 shows the dose attenuation fractions, obtained by EPID measurements, due to the prototypes and their corresponding support materials at 10 cm depth. The weight-bearing support materials of posterior mockup_{pos} (support_{pos}) attenuate more than the flexible foam layers of anterior mockup_{ant} (support_{ant}). Mockup_{ant}, which contains wire_{1,1} conductors, induces local dose reductions of $\leq 1.4\%$.

2.3.1.3 Monte Carlo simulations

The 28 μm surface dose simulations at 1.5 T showed a $46.7 \pm 0.2\%$ increase of the surface dose with a 0° beam angle, which equals 7% of D_{max} . Similar simulations from a -55° and $+55^\circ$ angle resulted in a $39.3 \pm 0.2\%$ increase (6% of D_{max}) and a $3.5 \pm 0.1\%$ decrease (0.5% of D_{max}) of the surface dose, respectively.

Table 2.3 shows the prototype-induced dose attenuation fractions at several beam angles. The attenuation of the support materials stays $\leq 0.3\%$. The cable results in local decreases of up to 1.5% for conductor crossings at 0° . Larger beam angles result in slightly larger dose changes: up to 2.1%. Values at 13 and 100 mm depth are approximately equal.

2.3.2 Imaging

Figure 2.7 shows the SNR maps of the single-channel prototypes. Depth profiles are plotted and show that the SNR on the anterior side is similar for all three prototypes, although wire_{1,0} produces the highest SNR. From 7 cm onwards, the wire_{1,0} and wire_{1,1} profiles overlap. All profiles end up at a similar asymptotic SNR value of around 5.0.

Figure 2.8 shows the the SNR maps of the multi-channel arrays. The transverse plane is positioned at the center of the array in craniocaudal direction. Depth profiles are plotted and clearly show that the SNR on the anterior side is increased when the prototype array is used. The SNR more than doubles at the surface and ends up at a similar asymptotic

Prototype	Angle [°]	A_{sim} (13 mm)	A_{sim} (100 mm)
Support only*	0	-0.1 ± 0.2 %	-0.2 ± 0.2 %
	30	-0.1 ± 0.2 %	-0.2 ± 0.2 %
	-30	-0.0 ± 0.2 %	-0.2 ± 0.3 %
	55	-0.3 ± 0.2 %	Not visible
	-55	-0.1 ± 0.2 %	Not visible
Support + wire _{1,1} [single/double]	0	-0.8 ± 0.1 % / -1.5 %	-0.8 ± 0.2 % / -1.3 %
	30	-1.0 ± 0.2 % / -1.4 %	-0.9 ± 0.2 %
	-30	-0.9 ± 0.2 % / -1.5 %	-1.0 ± 0.3 %
	55	-1.5 ± 0.2 % / -2.1 %	Not visible
	-55	-1.3 ± 0.2 % / -2.0 %	Not visible

Table 2.3 Dose attenuation fractions that were found with simulations (A_{sim}) due to the anterior support materials and wire_{1,1} cable at 1.5 T. If applicable, the attenuation of a single cable and a double cable (crossing point) are both reported. For some larger angles the dose profile at 100 mm fell outside of the scoring region. *Extracted from the conductor-free regions of the wire_{1,1} simulation.

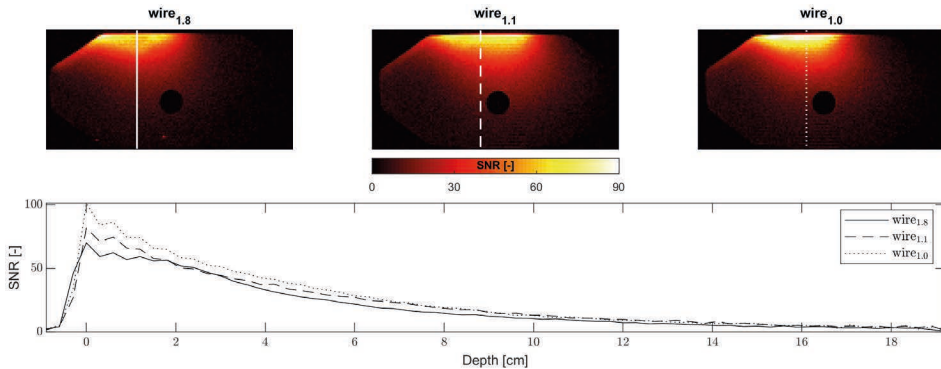


Figure 2.7 Top: Transverse SNR maps comparing the single-channel HIC prototypes. Bottom: Profiles are plotted through the center of the loops.

SNR value. Figure 2.9 shows the noise correlation matrices of the HIC prototype and full clinical array. No significant coupling effects can be observed in the prototype, while the clinical array does show channel coupling between channel 2 and 3.

Radiation experiments showed that the SNR, determined in an ROI directly under the loop, was not affected by irradiation with a 15×15 cm² beam. Figure 2.10 shows that both the single-channel prototype as well as the clinical array do not demonstrate a drop in SNR when radiation is turned on. Visual inspection revealed no signal changes or artifacts in the reconstructed images.

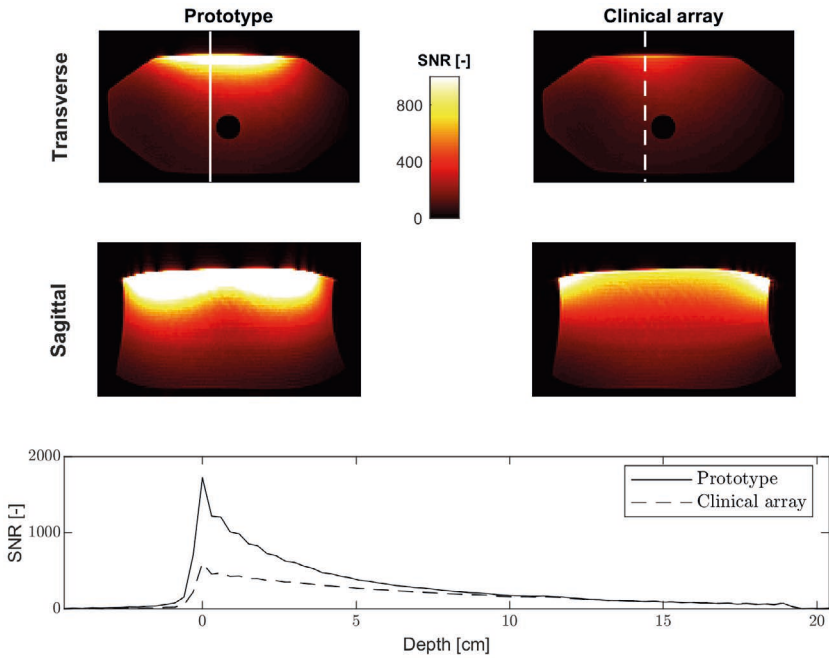


Figure 2.8 Top: SNR maps of the prototype (left) and clinical (right) array in the transverse and sagittal planes. No geometry correction was performed. Bottom: Profiles are plotted through the center of the arrays in the transverse plane.

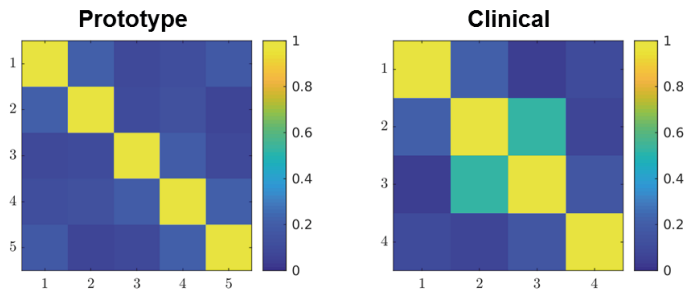


Figure 2.9 Noise correlation matrices of the 5-channel prototype (left) and clinical array (right).

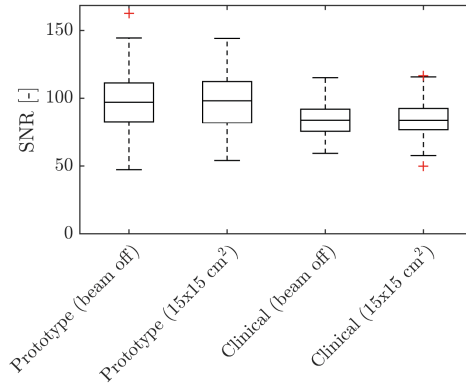


Figure 2.10 Comparison of the beam-on and beam-off SNR in a region of interest (ROI) under the prototype and clinical array. The ROI is placed directly under the loop.

2.4 Discussion

In this work, we introduce HICs as a suitable building block of radiolucent receive arrays for MRI-guided radiotherapy, as they lack tuning capacitors that can attenuate the treatment beam. The use of HICs has many advantages from an imaging perspective: HICs are flexible, inherently decoupled due to their limited current flow, easy to manufacture, and easily detunable over a broad frequency range. In addition, they allow for the use of non-rigid, low-density support materials to create radiolucent and light-weight arrays for increased patient comfort.

In this work, we showed the design and demonstrated the dosimetric feasibility of a flexible on-body receive array using HICs and showed the design's impact on the surface dose and dose at depth. Additionally, we investigated the imaging performance of single-channel prototypes.

Minimization of the bolus effect, and thus the surface dose of the patient, due to on-body placement was achieved by placing a 10 or 15 mm spacer between the HICs and the skin (Figure 2.6). Here, a conservative 15 mm distance is used for the dosimetry at depth and imaging measurements. When this 15 mm foam layer is placed, the HIC's dose imprint was resolved and anterior surface dose increase was only 7% of D_{max} , which we deemed acceptable. In comparison, the table currently increases the surface dose by 25% of D_{max} and is not considered problematic, as the introduction of high-energy beams and volumetric techniques have significantly decreased local surface doses. Moreover, direct placement of the posterior element under the patient may actually reduce the surface dose for posterior beams, as secondary electrons from the dense table may be curved away from the patient in the low-density support materials. On-body placement of the array does change the body outline and thus hinders the use of pre-calculated treatment plans that use a CT scan (without receive array) as reference image. However, current clinical practice for the MR-linac already includes adaptation of the treatment plan to

the anatomy of the day (adapt-to-shape) and therefore no longer requires an intact body contour. On-body placement should therefore pose no problem for MRI-guided radiotherapy treatments.

Dosimetry at a depth of 10 cm showed that the prototypes with the two thinnest cables result in maximal local dose changes of $\leq 0.8\%$ under a single cable and $\leq 1.4\%$ under a crossing point. The use of wire_{1,8} induced higher dose changes: -1.4% and -2.8% under the single cable and crossing points, respectively. Monte Carlo simulations with and without the magnetic field resulted in similar findings and matched well with the EPID dosimetry. Angulated simulations showed that the local dose reductions at depth increased up to 2.1% at a depth of 13 mm. Interestingly, the negatively angulated simulations led to an increased surface dose, while a positive angle reduced the surface dose with respect to the 0° situation. This is partially due to secondary electrons from the support materials that are curved away from the phantom by the Lorentz force and thus deposit less dose at the surface. Secondary electrons from the phantom's surface will also be curved away from the phantom and may partially be absorbed by the support materials, thus reducing the surface dose.

The clinical impact of all conductor-induced dose changes is deemed negligible, as slight, local underdosages from one beam will be smeared out due to physiological motion and clinical multi-angle beam or volumetric arc treatments. Clinically, local dose changes are expected to stay below 1% , which needs to be verified with dosimetry of a full multi-angle treatment using a full 32-channel array. If this proves to be the case, the full array can be disregarded during treatment planning. Hence, the array will have little impact on the clinical MR-linac workflow.

We demonstrated that the wire_{1,0} imaging prototype performed best, shortly followed by wire_{1,1}. Wire_{1,1} was found to be more durable and was therefore used in the multi-channel array. The 5-channel prototype clearly outperformed the clinical array: SNR at the surface more than doubled and became similar at larger depths. Expansion of the array to 32 channels will further improve the SNR and, more importantly, the parallel imaging capabilities for accelerated imaging. The flexible nature of the array will allow for optimal imaging sensitivity by folding around the patient. Irradiation of the HIC while imaging did not pose any problems and did not influence the measured SNR.

This work focused on the dosimetric feasibility of a radiolucent on-body array for MRI-guided radiotherapy, but its low-attenuating design also makes it interesting for application in hybrid PET/MRI systems. In this diagnostic application, the photons that are generated in a patient need to pass through the array to reach the PET detector. However, the attenuation of 511 keV photons will be different and must be assessed. Furthermore, other sites may also benefit from the flexible properties of the design, for example in the head and neck.

Theoretically, a low-impedance coil conductor can be thinner and could therefore lower local dose changes directly under the conductors of the array. However, the use of LICs poses severe challenges that complicate the design of a radiolucent MRIgRT receive array with a high channel count. An increased number of channels will result in narrower LICs, which in turn increases channel coupling. This can be mitigated to a certain degree by coil overlapping. However, this is only partially effective and requires rigid support materials, which in turn reduce the design's radiolucency. Adding more tuning capacitors (i.e., segmentation) is also not possible due to their beam attenuation. Additionally, gamma radiation can change the effective capacitance and consequently the coil's resonance frequency (Ferreira & Souza, 2017; Hamman, 1971). This effect should be further investigated in future work. HICs do not require tuning capacitors, thereby avoiding this issue altogether. Furthermore, this work shows that the use of HICs is dosimetrically feasible and, as discussed before, the advantages of HICs for imaging are abundant.

Future work will aim at manufacturing a full 32-channel array using the design described in this work. Realistic treatment plans with beams from multiple angles can then be delivered to show the final dosimetric impact of the array. Furthermore, a quantitative analysis of the parallel imaging performance of this array will show the potential acquisition time reduction.

2.5 Conclusion

In conclusion, the design of a flexible, on-body receive array was presented and was shown to be suitable for MRI-guided radiotherapy. HICs were shown to allow for dense placement of channels in a flexible radiolucent array without the coupling issues that LICs would exhibit. Surface dose increases were kept to a minimum with low-density foam spacers. The dosimetric impact at depth, even directly under the conductors, is acceptably low and will be further reduced by anatomical motion and the use of multiple beam angles. $wire_{1,0}$ and $wire_{1,1}$ outperform $wire_{1,8}$, both dosimetrically and in image quality. Beam-on imaging is possible and the radiation does not affect the SNR. Future research with a full array will have to show the gain in parallel imaging performance and thus acquisition time reduction.

2.6 Acknowledgements

This work is part of the research program HTSM with project number 15354, which is financed by the Netherlands Organization for Scientific Research (NWO). We thank André Wopereis for his help with the EPID measurements. We also extend thanks to David W. O. Rogers and the Carleton Laboratory for Radiotherapy Physics for granting the use of the Carleton Physics Department CPU computing cluster.

Appendix I: EPID dosimetry validation

The EPID signal response is expected to be linear with dose (Grein et al., 2002). This was validated by comparing the EPID signal response to ionization chamber measurements.

Methods

EPID measurements and attenuation calculations (A_{EPID}) were performed as described in section 2.2.2.2. Ionization chamber measurements used a 0.6 cm³ NE2571 Farmer type ionization chamber (NE Technology Limited, Berkshire, England) in solid water at a depth of 10 cm and with a slightly lower SSD of 144 cm. The same 10×10 cm² field size was used but with a 0° gantry angle. The dose attenuation fractions were calculated with

$$A_{ion\ chamber} = \frac{Q_{object} - Q_{open}}{Q_{open}}, \quad (2.5)$$

where Q_{object} and Q_{open} are the measured charges with and without an object on the phantom. Ionization chamber measurements were performed three times per setup.

Results

Table 2.4 shows that the dose attenuation fractions that are measured using an EPID and an ionization chamber are similar. The attenuation of 10 mm solid water and 1 mm copper are slightly under- and overestimated by the EPID, respectively. With an R^2 of 0.95 with respect to the identity line, the signal-dose linearity assumption is found to be reasonable.

Object (+ 100 mm solid water)	$A_{ionchamber}$ [%]	A_{EPID} [%]
Support anterior element	-0.17±0.04 %	-0.2±0.2 %
2 mm solid water	-0.76±0.04 %	-0.8±0.2 %
5 mm solid water	-1.99±0.00 %	-1.8±0.2 %
10 mm solid water	-3.91±0.00 %	-3.4±0.2 %
1 mm copper	-2.59±0.07 %	-2.9±0.2 %

Table 2.4 Dose attenuation fractions that were found with ionization chamber ($A_{ionchamber}$) and EPID (A_{EPID}) measurements. Values are shown for several objects that are placed against 100 mm solid water.

Appendix II: Impact of the magnetic field on the attenuation

The magnetic field is expected to have no influence on the dose at a depth of 10 cm. Here, the impact of the magnetic field is investigated.

Methods

The EPID dosimetry results were taken from Table 2.2. The results of the simulations with a 1.5 T magnetic field were taken from Table 2.3. These simulations were repeated without a magnetic field (0 T) to investigate the influence of the field strength on the dose.

Results

Table 2.5 shows the dose attenuation fractions that were found with the three methods. The simulations show no impact of the magnetic field on the dose changes that were found. The EPID dosimetry matches well with the simulations, although the wire_{1.8} attenuation values are slightly lower than in the simulations.

Prototype	A_{EPID} (0 T)	A_{sim} (0 T)	A_{sim} (1.5 T)
Support only	-0.2±0.1 %	-0.2±0.2 %	-0.2±0.2 %
Support + wire _{1.8} [single/double]	-1.4±0.1% / -2.8%	-1.7±0.3 % / -3.0 %	-1.7±0.2 % / -3.0 %
Support + wire _{1.1} [single/double]	-0.8±0.1% / -1.4%	-0.8±0.2 % / -1.3 %	-0.8±0.2 % / -1.3 %
Support + wire _{1.0} [single/double]	-0.8±0.2% / -1.3%	Not available	-0.7±0.2 % / -1.1 %

Table 2.5 Comparison of the dose attenuation fractions at a depth of 10 cm that are measured with EPID dosimetry (A_{EPID}) and Monte Carlo simulations (A_{sim}) at 0 T and 1.5 T. If applicable, the attenuation of a single cable and a double cable (crossing point) are both reported.

CHAPTER 3

Improving the imaging performance of the 1.5 T MR-linac using a flexible, 32-channel, on-body receive array

The following chapter is based on:

Zijlema, S. E., Tijssen, H. N., Dijk, L. van, Hackett, S. L., Wolthaus, J. W. H., Breimer, W., Lagendijk, J. J. W., & van den Berg, C. A. T.. (2020). Improving the imaging performance of the 1.5 T MR-linac using a flexible, 32-channel, on-body receive array. *Physics in Medicine & Biology*, 65(21), 215008.

Abstract

Background High impedance coils (HICs) are suitable as a building block of receive arrays for MRI-guided radiotherapy (MRIgRT) as HICs do not require radiation-attenuating capacitors and dense support materials. Recently, we proved the feasibility of using HICs to create a radiation transparent (i.e., radiolucent) window.

Purpose In this work, we constructed a fully functional 32-channel array based on this design. The anterior element is flexible and follows the shape of the subject, while the posterior element is rigid to support the subject. Both elements feature a 2×8 channel layout. Here, we discuss the construction process and characterize the array's radiolucency and imaging performance.

Methods The dosimetric impact of the array was quantified by assessing the surface dose increase and attenuation of a single beam. The imaging performance of the prototype was compared to the clinical array in terms of visual appearance, signal-to-noise ratio (SNR), and acceleration performance, both in phantom and in-vivo measurements.

Results Dosimetry measurements showed that on-body placement changed the anterior and posterior surface dose by +3% and -16% of the dose maximum. Attenuation under the anterior support materials and conductors was 0.3% and $\leq 1.5\%$, respectively. Phantom and in-vivo imaging with this array demonstrated an improvement of the SNR at the surface and the image quality in general. Simultaneous irradiation did not affect the SNR. G-factors were reduced considerably and clinically used sequences could be accelerated by up to 45%, which would greatly reduce pre-beam imaging times. Finally, the maximally achievable temporal resolution of abdominal 3D cine imaging was improved to 1.1 s, which was $>5\times$ faster than could be achieved with the clinical array. This constitutes a big step towards the ability to resolve respiratory motion in 3D.

Conclusions The proposed 32-channel array is compatible with MRIgRT and can significantly reduce scan times and/or improve the image quality of all on-line scans.

3.1 Introduction

Hybrid MRI-radiotherapy systems (Fallone, 2014; Keall et al., 2014; Lagendijk et al., 2014; Mutic & Dempsey, 2014) allow for monitoring of mobile tumors and organs at risk (OARs) with magnetic resonance imaging (MRI) before, during, and after radiation therapy treatments. Based on observed changes, the tumor and OARs can be recontoured and the treatment plan can be adapted to improve tumor coverage and minimize toxicity. High image quality is therefore required to accurately delineate these structures. Furthermore, cine MRI can be used to track the anatomical changes that occur during treatments (intrafraction motion). However, as MRI is inherently slow, high-quality preparatory (pre-beam) imaging takes relatively long and real-time anatomy monitoring is limited to 2D planes or small, low-resolution 3D volumes. This limitation may be overcome when receive arrays with a high channel count are used, as these enable the use of high acceleration factors through their increased parallel imaging (PI) capabilities (Breuer et al., 2005; Larkman et al., 2001; Pruessmann et al., 1999).

The 1.5 T Elekta MR-linac (Unity, Elekta AB, Stockholm, Sweden) currently comes with a clinical receive array that consists of two 4-channel elements. These elements are placed centimeters away from the anatomy: the anterior element is elevated above the patient while the posterior element is placed underneath the table (Hoogcarpsel et al., 2018). The limited channel count, combined with its 1×4 -channel arrangements and distant positioning, limits the signal-to-noise ratio (SNR) and PI performance in all planes.

Previous work (Zijlema et al., 2019a) proposed the design of an 32-channel on-body array that is suitable for MRI-guided radiotherapy (MRIgRT). High impedance coils (HICs) were used, as these exhibit less coupling with neighboring elements, are flexible, and do not require beam-attenuating lumped elements to tune to the resonance frequency. Instead, HICs use the distributed capacitance of the coaxial conductor (Zhang et al., 2018). This way, a radiation transparent, or radiolucent, window was achieved with a double-row layout. It was shown that the materials of the flexible, anterior element did not significantly change the delivered dose and that on-body placement did not significantly increase the surface dose. Finally, an increase of the SNR was shown when comparing the imaging performance of a 5-channel prototype to the clinical array on a phantom.

In this work, we constructed a fully functional 32-channel array for the 1.5 T MR-linac based on the aforementioned design. We discuss the construction process and characterize the array's radiolucency and imaging performance. The dosimetric impact of the array is quantified by assessing the surface dose increase and attenuation of a single beam. The imaging performance of the prototype was compared to the clinical array in terms of visual appearance, signal-to-noise ratio (SNR), and acceleration performance, both in phantom and in-vivo measurements. The latter included T_2 turbo spin echo (TSE) sequences that are clinically used for on-line contouring and 3D cine sequences that can be used for motion tracking.

3.2 Methods

3.2.1 Construction

Based on the design of Zijlema et al. (2019a), the anterior and posterior elements of the 32-channel array contain 16 channels each, which are placed in a 2×8 channel layout (Figure 3.1). As a reference, the design of the clinical array is schematically shown in Figure 3.1e. The high-impedance coil loops of the new array (9×19 cm²) were constructed from AlphaWire (Elizabeth, NJ, USA) 9432 wire to resonate at 63.87 MHz and were sewn onto a 0.5 mm polystyrene sheet (Figure 3.1c). All loops were connected to newly designed matching and detuning circuitry (Figure 3.2), which in turn connected to an interfacing box with the preamplification and digitization hardware. Foam layers were added to cover the electronics and create a conductor-to-surface distance of 15 mm to reduce the bolus effect (Ghila et al., 2016; Zijlema et al., 2019a). Coupling between channels, which occurs when multiple channels are placed in close proximity (Roemer et al., 1990), was limited due to the use of HICs and was further mitigated by overlapping the loops (Figure 3.1c). Coupling of the final layout was assessed on the bench and found to be low (see section 3.7). Coupling values are compared to those of the clinical array in section 3.2.3. The use of light-weight materials resulted in an anterior element that weighs 1.3 kg and a posterior element that weighs 1.5 kg. Cables to and from the interfacing boxes are routed such that none cross through the radiation path, i.e. cable output is required on both sides of the bore. A safety assessment of the full array was performed to ensure volunteer safety by identifying potential risks and implementing design mitigations (Rispoli, 2019).

3.2.2 Dosimetry

Two aspects of the dosimetric impact of the 32-channel receive array were evaluated: (1) the surface dose increase (bolus effect) and (2) the single-beam attenuation.

The bolus effect was quantified by comparing the anterior and posterior surface dose with and without the prototype present. The anterior bolus effect was assessed first. A GAFChromic (Ashland, USA) EBT-3 film (lot: 10241901) was placed on top of a solid water phantom in a 1.5 T MR-linac. A 7 MV, 2000 MU, 20×10 cm² beam was delivered from 0° with and without the anterior element of the prototype directly on top. In order to compare the posterior bolus effect, the phantom was placed on top of the posterior element of the prototype. An EBT-3 film was placed between the prototype and the phantom and a 1000 MU, 20×10 cm² beam was delivered from 180°. Next, the prototype was removed, the thin Elekta-provided couch mattress was placed, and the measurement was repeated to obtain the posterior reference surface dose. The bolus effect was then calculated as the relative difference between the two measurements of each set.

Subsequently, electronic portal imaging device (EPID) dosimetry was used to assess the single-beam attenuation at 10 cm depth, which has been shown to correspond well to

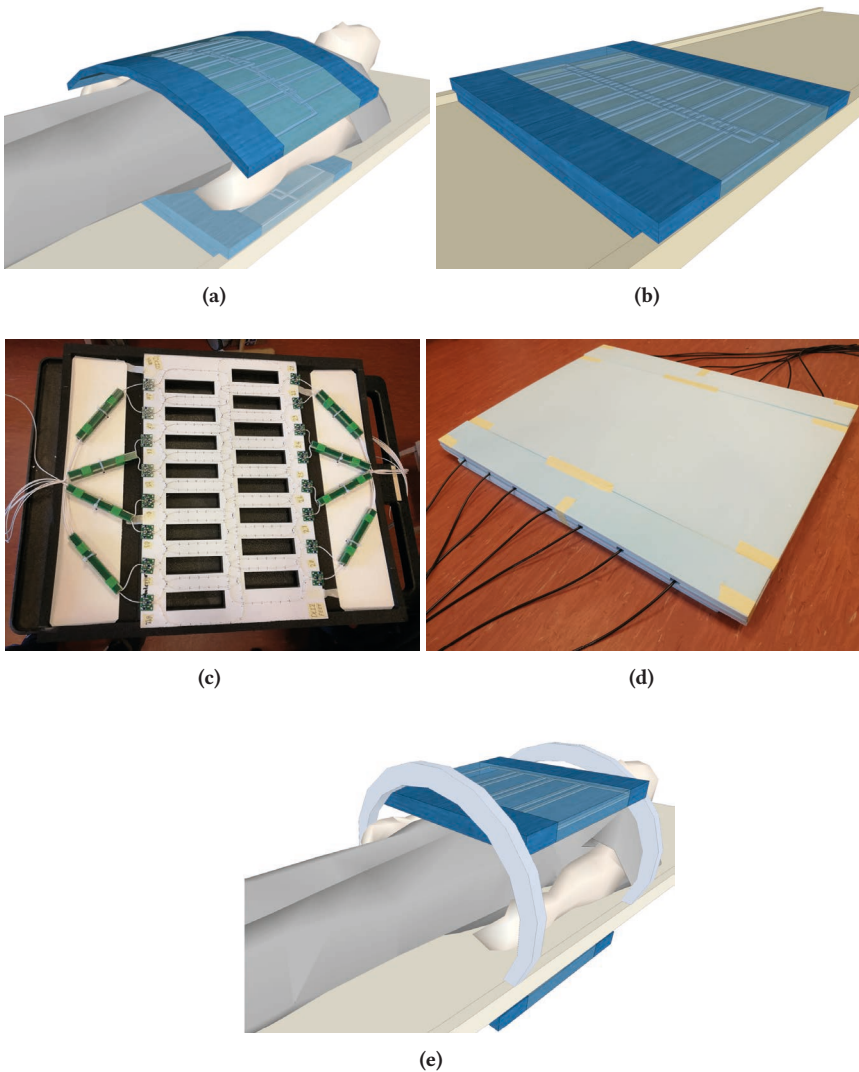


Figure 3.1 (a,b) Schematic views of the positions of the prototype's anterior and posterior elements. (c,d) Photos showing the anterior element without its cover (c) and the full posterior element (d). The electronic layout is the same for both elements. Loops are sewn onto a thin plastic sheet and connected to a matching and detuning board. Signal cables are routed through custom cable traps and connected to interface boxes with preamplification and digitization hardware. The use of light-weight materials resulted in an anterior element that weighs 1.3 kg and a posterior element that weighs 1.5 kg, including cabling and cable traps. (e) Schematic view of the clinical array with the anterior element elevated above the patient using a double-arc bridge and the posterior element below the table.

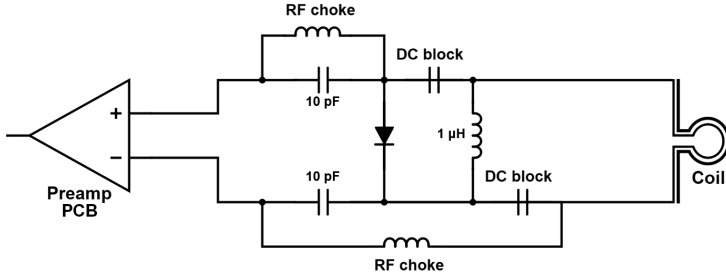


Figure 3.2 Matching and detuning circuitry. At the port side of the HIC, the shield of both ends is connected. The circuitry is connected to a preamplifier PCB via a coaxial cable. On this PCB, the DC detuning current is superimposed onto the signal lines. Furthermore, a T-network is implemented to achieve optimal preamp decoupling with the 1.5 m long signal cables (Roemer et al., 1990).

ionization chamber measurements (Grein et al., 2002; Zijlema et al., 2019a). All EPID measurements were performed on a conventional linac (Synergy, Elekta AB) without a magnetic field and at a gantry angle of 90° so that the setup could be placed directly against the panel. Images were acquired using XIS (PerkinElmer, Waltham, MA, USA) with an acquisition time of 433 ms per frame and with all automatic corrections disabled. The beams (6 MV, 100 MU, $10 \times 10 \text{ cm}^2$) were delivered with a dose rate of 250 MU min^{-1} . 100-frame averages were saved that covered a full beam delivery and 5-minute waiting periods were employed to avoid ghosting effects. Reference images, i.e. beam-off (dark) images and acquisitions without phantom, were acquired and used to process the acquisitions (I_{proc}), as described by McDermott et al. (2004). The dose attenuation fraction due to an array (A_{EPID}) can then be calculated with

$$A_{EPID} = \frac{I_{proc,array} - I_{proc,no\ array}}{I_{proc,no\ array}}. \quad (3.1)$$

3.2.3 Imaging performance

Imaging performance was assessed by measuring the coupling between channels, signal-to-noise ratio (SNR), and parallel imaging (PI) performance. Additionally, the impact of radiation on the SNR is assessed. All imaging was performed on a 1.5 T Elekta Unity MR-linac and compared the performance of the 8-channel clinical array to the 32-channel prototype.

First, raw data were acquired of a pelvis-sized phantom (PVP- and agar-based, 2.6% NaCl) with dielectric properties that are representative of a human body. Noise correlation matrices were generated by calculating the Pearson correlation coefficients from the noise-only pre-scan. SNR maps were generated from 3D acquisitions (Table 3.1) with a noise-only dynamic, as described by Kellman and McVeigh (2005).

Subsequently, the impact of the radiation beam on the SNR was assessed. In previous work, radiation-induced signal spikes in acquired k-space lines have been described when a beam passes through a receive array (Burke et al., 2010; Hoogcarspel et al., 2018). This effect was assessed by calculating the time-course SNR from two dynamic series (Hoogcarspel et al., 2018): one with and one without a large beam ($15 \times 15 \text{ cm}^2$, 430 MU min^{-1}) that crossed the array. The experiment was performed with the full 32-channel prototype and the 8-channel clinical array.

Finally, in-vivo imaging of three volunteers was performed comparing the prototype and clinical array. The quality of the clinically used 3D T_2 -weighted TSE pre-beam acquisitions (Table 3.1) was compared and the sequence was optimized in terms of acquisition speed by taking advantage of the additional channels of the prototype. Furthermore, g-factor maps were generated from 3D in-vivo acquisitions (Table 3.1) to compare the acceleration performance of the two arrays. The g-factor is a spatial measure of the noise amplification that occurs when an unfolded image is reconstructed from undersampled data (Pruessmann et al., 1999). Here, a higher g-factor will lead to more SNR loss and increases the chance of unresolved artifacts. Mean g-factors were calculated within the body contour for all volunteers. Lastly, a 3D bSSFP cine sequence was optimized in terms of speed for each array (Table 3.1).

3.3 Results

3.3.1 Dosimetry

The placement of the prototype array increased the anterior surface dose by 28% (+3% of D_{max}) with respect to the situation without array present. In contrast, the posterior surface dose was reduced by 41% (-16% of D_{max}) when the posterior element was present.

Figure 3.3 shows the attenuation maps that were obtained from the EPID measurements. The anterior element of the prototype has low-attenuating support materials (0.3%). As expected, the HICs attenuate slightly more: 0.8% under a single conductor and 1.5% under a crossing point. The support materials of the posterior element attenuate 0.6% and a single conductor and conductor crossing increase this value to 1.1% and 1.6%, respectively. In comparison, the anterior element of the clinical array attenuates approximately 0.4% (0.5% under conductor) and the posterior element 1.2% (1.3%).

3.3.2 Imaging

Coupling between channels during the MRI acquisitions is shown in Figure 3.4. Coupling between the channels, i.e. the off-diagonal values of the matrix, are lower in the prototype (≤ 0.30 vs. ≤ 0.47), although the loop size is smaller.

Sequence	Phantom (SNR)		In-vivo pre-beam		In-vivo 3D cine	
	Clinical sequence	Prototype-optimized	Clinical-array-optimized	Prototype-optimized		
TR / TE	10.0 / 1.8 ms	1535 / 277 ms	3.7 / 1.8 ms			
FOV	425×250×250 mm ³	425×250×250 mm ³	400×350×193 mm ³			
Voxel size	3×3×10 mm ³	1.5×1.5×2 mm ³	5×5×5 mm ³			
Flip angle	20°	90°	40°			
SENSE [R _{FH} , R _{LR}]	No	[1.0, 3.6] / [1.5, 4.0] / [1.3, 5.0]	[1.0, 3.0]	[1.3, 4.5]		
Partial Fourier [FH, LR]	No	[0.63, 1.0]	[0.63, 1]			
Oversampling	Yes, FH: 1.4×	Yes, FH: 1.5×	Yes, FH: 2.0×	No		
Acq. time	0:41 min	2:09 min / 1:18 min / 1:09 min	5.8 s	1.1 s		

Table 3.1 MRI sequence parameters of several acquisitions. SENSE acceleration factors (R) and partial Fourier factors are reported in the feet-head (FH) and left-right (LR) directions.

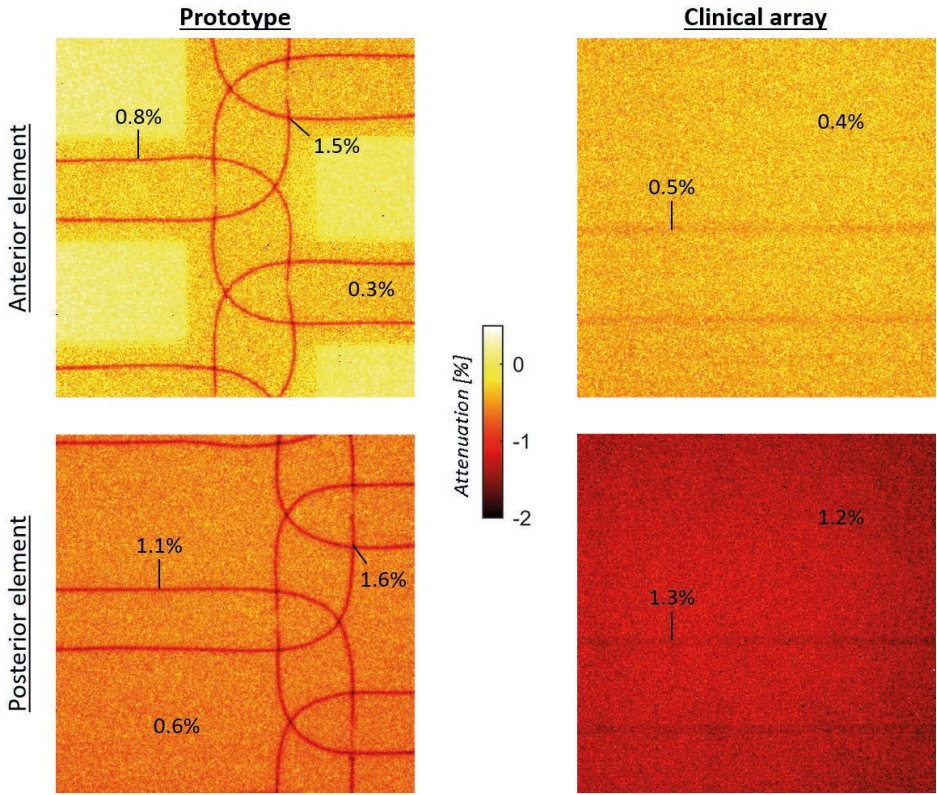


Figure 3.3 Attenuation maps ($10 \times 10 \text{ cm}^2$) comparing the radiolucency of the anterior and posterior elements of the prototype and clinical array. Attenuation values are shown under the support materials, single conductor, and conductor crossing. Other regions of the radiolucent window that are outside the $10 \times 10 \text{ cm}^2$ FOV attenuate similarly.

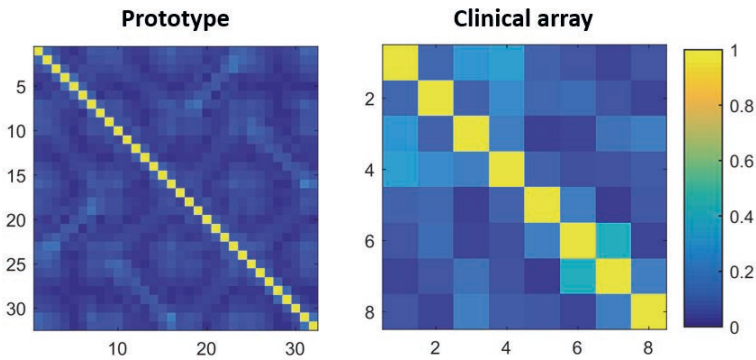


Figure 3.4 Noise correlation matrices of the 32-channel prototype (left) and 8-channel clinical array (right).

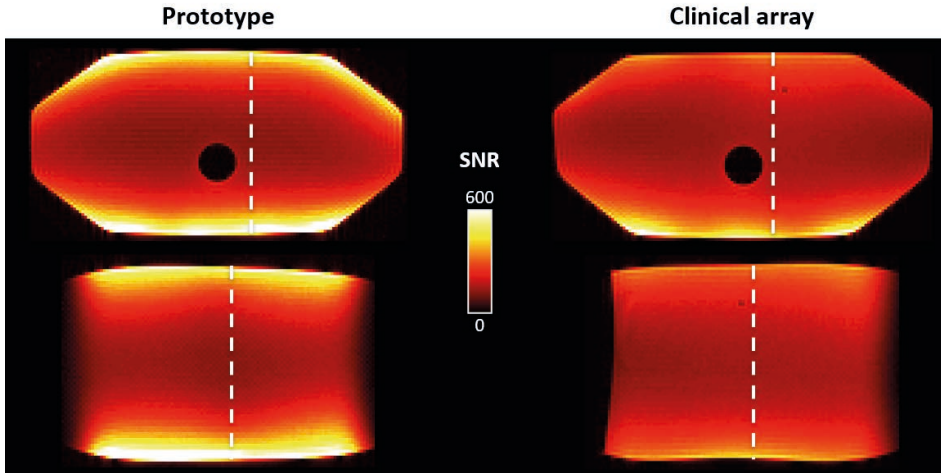


Figure 3.5 Transverse (top) and sagittal (bottom) slices of SNR maps obtained with the 32-channel prototype and clinical array. The white line shows the location of the orthogonal slice. No geometry correction was performed.

SNR maps were generated from scans with the 32-channel prototype and 8-channel clinical array (Figure 3.5). These show an increase of the SNR at the surface when the prototype is used, while the SNR at larger depths is similar.

Figure 3.6 showcases the image quality of a clinically used T_2 TSE sequence with and without acceleration using SENSE. The prototype outperforms the clinical array in terms of SNR, which is best visible in the pubic bone. The reduced SNR, due to the acceleration of the acquisition, is especially pronounced when the scan time is reduced by 40%.

Figure 3.7 attests that the prototype improves the PI performance by reducing g-factors, which in turn reduces SNR loss and minimizes unfolding artifacts. The mean g-factor for several combinations of acceleration factors are shown in Table 3.2.

Figure 3.8 shows that the improved PI performance of the prototype can be used to acquire highly accelerated 3D cine imaging of the abdominal region with a temporal resolution of 1.1 s. The clinical array required a scan time of 5.8 s to achieve a comparable image quality. Videos of these dynamic acquisitions are available in the online version of this article.

3.4 Discussion

In this work, we built a light-weight 32-channel HIC receive array based on the design of Zijlema et al. (2019a). We showed that the full 32-channel on-body array is dosimetrically feasible for use in a 1.5 T MR-linac and significantly improves the image quality and speed compared to the current clinical array.

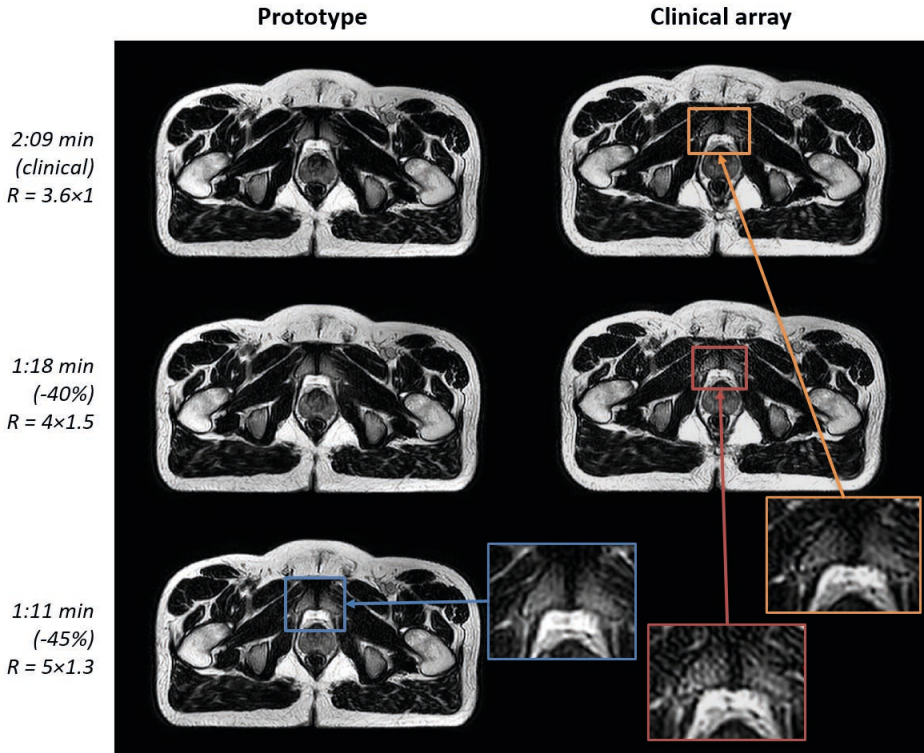


Figure 3.6 In-vivo data of the clinically used T_2 TSE sequence (top row) and accelerated acquisitions. Severe noise amplification in the regions of interest can be seen for the clinical array (red arrow). The fastest scan was not allowed by the scanner software using the clinical array, as the scan used $SENSE_{LR} > 4$.

	Prototype			Clinical		
	$R_{FH} = 1$	1.5	2	$R_{FH} = 1$	1.5	2
$R_{LR} = 1$	1.0±0.0	1.0±0.1	1.2±0.2	1.0±0.0	2.1±1.7	4.7±2.6
2	1.0±0.0	1.1±0.1	1.2±0.2	1.0±0.0	2.3±2	5.5±3.6
3	1.1±0.1	1.1±0.1	1.3±0.2	1.1±0.2	2.9±2.9	7.8±4.9
4	1.3±0.2	1.4±0.2	1.6±0.3	1.4±0.2	5.6±9.2	19.3±20.2
4.5	1.6±0.3	1.6±0.3	1.9±0.4	1.9±0.9	9.4±17.5	32.2±34.4
5	1.8±0.4	1.9±0.4	2.1±0.5	2.6±1.9	11.7±21	34.9±35.8

Table 3.2 Mean and standard deviation of g-factors for several combinations of acceleration factors in feet-head (R_{FH}) and left-right (R_{LR}) direction. All data of three volunteers is combined. Mean g-factors above 2.0 are considered high and are marked in orange.

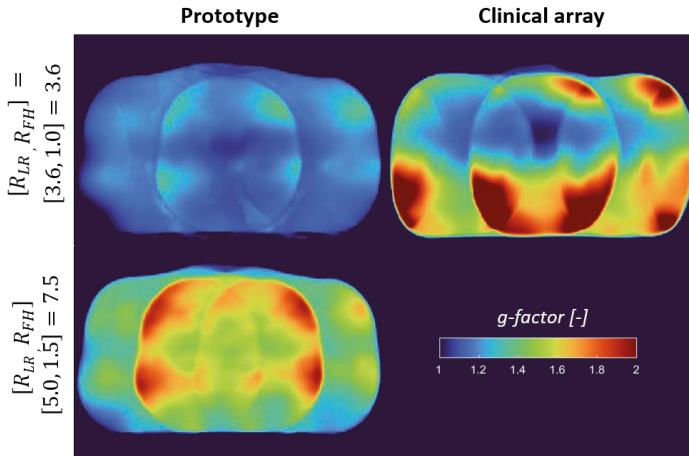


Figure 3.7 In-vivo g-factor maps from the clinically used MRI sequence (top row) and highly accelerated acquisition. Values are substantially lower when the prototype array is used, even when the scan time is reduced by more than half.

On-body placement of the array resulted in a surface dose increase of 3% of D_{\max} . This is even lower than was found by Zijlema et al. (2019a) and deemed acceptable. The difference can be explained by the new support materials and the higher delivered dose, which improves the method's accuracy. The surface dose on the posterior side actually reduced by 16% with the posterior element in place due to its significantly lower (electron) density compared to the treatment couch. The single-beam attenuation values due to the prototype ($\leq 1.5\%$) were in good agreement with the acceptably low values that were reported by Zijlema et al. (2019a). The maximum attenuation values (1.5%) were found directly under two overlapping conductors. Clinical impact of these slight, local underdosages is deemed negligible, as changes from one beam will be smeared out due to physiological motion and the use of multi-angle beam or volumetric arc treatments. Therefore, dose changes are expected to be well below 1%. These results indicate that the anterior element of the 32-channel array can be disregarded in the treatment planning process. The posterior element has a fixed position on the bed and can easily be included in the treatment planning process.

The use of HICs was a key factor to allow for dense placement of 32 channels without dosimetric impact, due to its lack of electronic components in the radiation window. Moreover, dense placement was possible due to the inherently limited coupling between HICs (Zhang et al., 2018). Replacing the single-row with a double-row channel layout provides an additional dimension in coil sensitivity variation (the feet-head direction) and thereby enhances the PI capabilities. Further increasing the number of rows in this direction would again improve the PI performance, but the placement of additional cabling and circuitry will be hindered by the requirement of a radiolucent window during MRIgRT. Two rows therefore seem to be the maximally achievable.

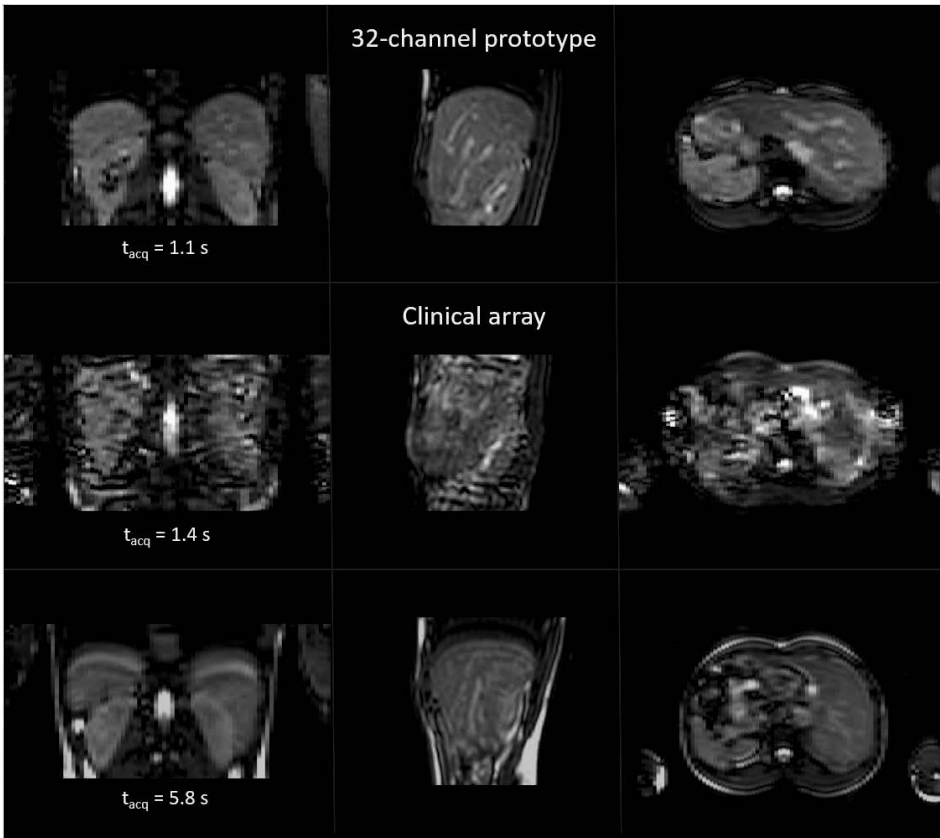


Figure 3.8 Three views (coronal, sagittal, transverse) of the 3D cine imaging volumes using the prototype (top) and clinical array (bottom). The prototype produces 3D images without noticeable artifacts, while the 1.4 s acquisition with the clinical array is unusable. The third acquisition shows severe motion artifacts, e.g. in the liver dome, due to the long acquisition time with respect to the respiratory cycle. Animations of these three dynamic series can be found in the supplementary information. Note that the last acquisition was acquired in a different volunteer.

The imaging performance of the prototype was compared to the current clinical array in several ways. First, its coupling between channels was found to be lower, although the channel size was smaller and each channel is neighbor to more channels due to the double-row layout. As discussed before, the use of HICs enabled dense channel placement with minimal coupling. Furthermore, the SNR of the prototype was found to be higher at the surface and similar at depth. The radiation beam did not seem to impact these findings. Beam-on imaging showed that the radiation did not change the tSNR, as was found by Zijlema et al. (2019a). Previous work by Hoogcarspel et al. (2018) did report a slight change, which could be explained by the larger field size ($22 \times 22 \text{ cm}^2$ vs. $15 \times 15 \text{ cm}^2$) and higher default dose rate (680 MU min^{-1} vs. 430 MU min^{-1}) in comparison to this work.

In-vivo acquisitions of volunteers showed that the g-factors were substantially lower when the prototype was used. Consequently, an approximate two-fold scan time reduction of a clinically used T_2 TSE sequence could be achieved. Current MR-linac protocols include three T_2 TSE scans of 2 or 4 minutes, i.e. total scan times can likely be reduced by up to 6 minutes. The improved acceleration performance may also be used for further optimization of the image quality, e.g. in terms of resolution or SNR. Finally, the temporal resolution of 3D cine imaging has been shown to improve more than five times, from 5.8 s to 1.1 s. Although the latter is still not able to completely avoid intradynamic motion, this constitutes a big step towards the ability to resolve respiratory motion in 3D. Further acceleration should be sought in the acquisition and reconstruction methods, e.g. using deep learning (Mehta & Majumdar, 2017; Terpstra et al., 2020a). Although the acquisition voxel size of $5 \times 5 \times 5 \text{ mm}^3$ is relatively coarse, Glitzner et al. (2015) have shown that subvoxel motion can be detected at up to one third of the voxel size.

The 32-channel array could also improve diffusion weighted imaging (DWI) for treatment response monitoring on the MR-linac. In DWI sequences, echo-planar imaging (EPI) readouts are mostly used, which are prone to geometric distortions due to their long readout trains over which phase errors accumulate (Mansfield, 1977). These distortions are clearly undesired in a radiotherapy (treatment) setting. The ability to use higher acceleration factors with the 32-channel array will reduce the length of the echo trains, which results in fewer geometric distortions. Additionally, shorter echo trains will reduce intrashot T_2^* decay and thus signal blurring.

Now that a radiolucent HIC array has been shown to be feasible, the design concept could be extended to other sites that could benefit from the flexible properties, such as the head and neck. Furthermore, the application of the current array in hybrid PET/MRI systems could be investigated. In PET/MRI, attenuation correction of on-body receive arrays is similarly difficult and significant changes of the measured abdominal activity values can occur (Fürst et al., 2014; Wollenweber et al., 2014). The radiolucent properties of our proposed design could reduce the number of photons that are attenuated or scattered and thus improve the accuracy and SNR.

3.5 Conclusion

The presented receive array improves the imaging performance with respect to the current clinical array. Its 32 channels enable the use of high undersampling factors, which reduced pre-beam and 3D cine scan times by about half and 80%, respectively. All this can be achieved without inducing clinically relevant dose changes.

3.6 Acknowledgements

This work is part of the research program HTSM with project number 15354, which is financed by the Netherlands Organization for Scientific Research (NWO) and Philips Healthcare. Assembled coil mats and anterior support materials were kindly provided by Tesla Dynamic Coils (Zaltbommel, the Netherlands) and Catalina Arteaga de Castro. The authors would like to thank Eveline Alberts for her help with the protocol optimization.

3.7 Appendix: Coupling bench test

The coupling between channels of the prototype was measured on the bench using an in-house developed automated VNA RF switch (Welting et al., 2020) and resulted in a 32×32 S-matrix. Bending of the loops did not significantly affect the tuning, matching and coupling of the array. The bench-measured coupling is displayed in Figure 3.9.

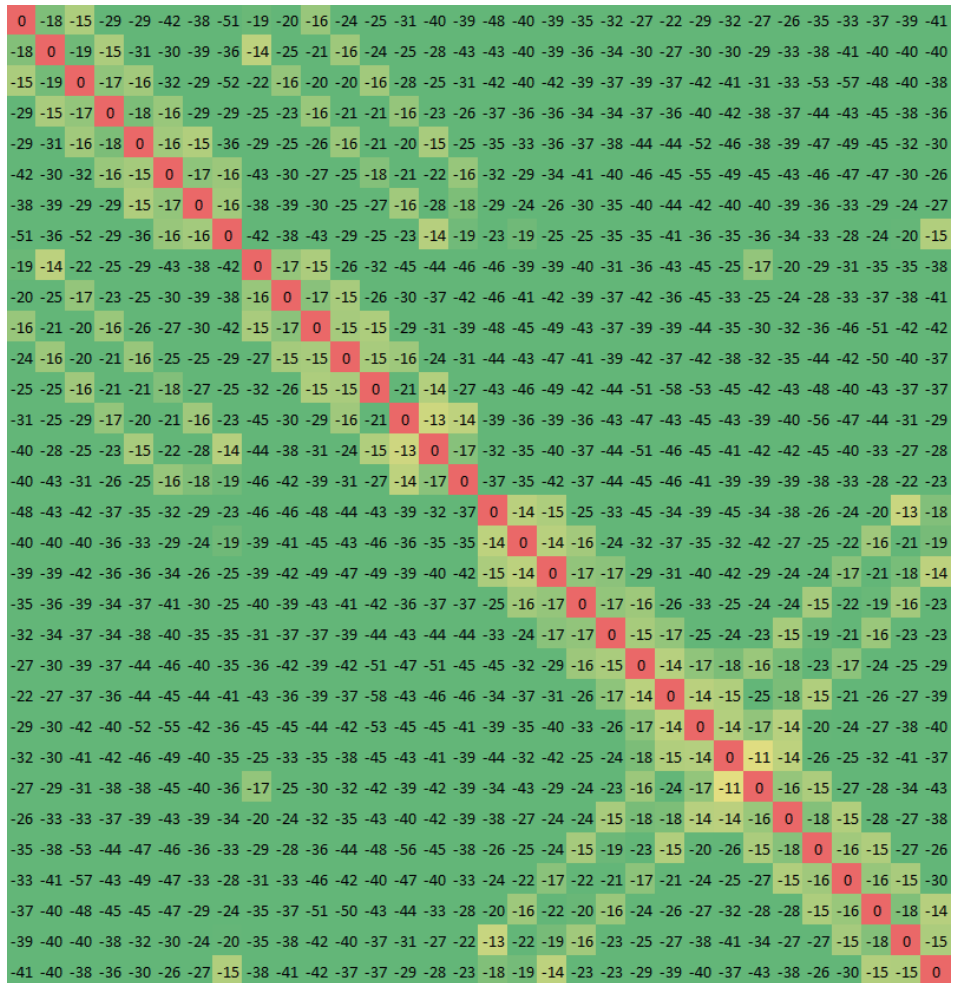


Figure 3.9 Coupling matrix of the prototype in dB during a bench test.

CHAPTER 4

A mask-compatible, radiolucent, 8-channel head and neck receive array for MRI-guided radiotherapy treatments and pre-treatment simulation

The following chapter is based on:

Zijlema, S. E., Breimer, W., Gosselink, W. J. M., Bruijnen, T., Arteaga de Castro, C. S., Tijssen, H. N., Lagendijk, J. J. W., Philippens, M. E. P., & van den Berg, C. A. T.
Submitted to Physics in Medicine & Biology.

Abstract

Background Immobilization masks are used to prevent patient movement during head and neck (H&N) radiotherapy. Motion restriction is beneficial both during treatment, as well as in the pre-treatment simulation phase, where MRI is often used for target definition. However, the shape and size of the immobilization masks hinder the use of regular, close-fitting MRI receive arrays.

Purpose In this work, we developed a mask-compatible 8-channel H&N array that consists of a single-channel baseplate on which the mask can be secured and a flexible 7-channel anterior element that follows the shape of the mask. The latter uses high impedance coils to achieve its flexibility and radiolucency.

Methods A fully-functional prototype was manufactured, its radiolucency was characterized, and the gain in imaging performance with respect to current clinical setups was quantified.

Results Dosimetry measurements showed an overall dose change of -0.3%. Small, local deviations were up to -2.7% but had no clinically significant impact on a full treatment plan, as gamma pass rates (3%/3 mm) only slightly reduced from 97.9% to 97.6% (clinical acceptance criterion: $\geq 95\%$). The proposed H&N array improved the imaging performance with respect to two clinical setups. The H&N array more than doubled (+123%) and tripled (+246%) the signal-to-noise ratio with respect to the clinical MRI-simulation and MR-linac setups, respectively. G-factors were also lower with the proposed H&N array. The improved imaging performance resulted in a clearly visible SNR improvement of clinically used TSE and DWI acquisitions.

Conclusions In conclusion, the 8-channel H&N array improves the imaging performance of MRI-simulation and MR-linac acquisitions, while dosimetry suggests that no clinically significant dose changes are induced.

4.1 Introduction

Magnetic resonance imaging (MRI) has become the gold standard for diagnosis and target definition in the pre-treatment simulation phase of the head and neck (H&N) radiotherapy workflow. More recently, MRI capabilities have also become available during treatments with the introduction of hybrid MRI-radiotherapy machines (Fallone, 2014; Keall et al., 2014; Lagendijk et al., 2014; Mutic & Dempsey, 2014). On these machines, MRI can be used to monitor mobile tumors and organs at risk (OARs) before, during, and after each radiation therapy fraction (MRI-guided radiotherapy, MRIgRT).

In the field of H&N cancer the use of MRI has clear benefits in terms of tumor definition (Chung et al., 2004). Currently, MRI is mostly used during the simulation phase, but the first H&N patients have also been treated with MRIgRT to investigate the benefits (Chen et al., 2017; Henke et al., 2018).

However, the MRI setup can be complicated by the devices that are used for reproducible patient positioning in H&N radiotherapy, i.e. thermoplastic immobilization masks. The shape and size of these masks hamper the use of conventional, close-fitting H&N MRI receive arrays. Current clinical MRI setups for the pre-treatment simulation phase therefore often consist of (multiple) receive arrays with suboptimal geometries and coil positions, which result in a poor fit of the anatomy, i.e. a low filling factor (Mandija et al., 2019; Verduijn et al., 2009). Consequently, the signal-to-noise ratio (SNR) and acceleration performance are relatively low. Moreover, regular receive arrays cannot be used during MRIgRT, as these have not been designed to withstand the radiation and can attenuate the beam (Hoogcarspel et al., 2013). Therefore, special radiation transparent, or radiolucent, MRIgRT-compatible arrays have been developed (Hoogcarspel et al., 2018; Klüter, 2019; Zijlema et al., 2020). However, those arrays are not dedicated to H&N, which again limits the imaging performance, or require adjustment of each individual immobilization mask (Boeke et al., 2021). A fully mask-compatible H&N array for MRIgRT treatments does not exist, thus limiting the image quality in treatment position.

In this work, a dedicated H&N array was developed that is compatible with an immobilization mask and can be used in both the simulation and treatment phases of MRIgRT. The 8-channel array consists of (i) a single-channel baseplate on which the mask is secured and (ii) a flexible 7-channel element following the shape of the mask for an optimal filling factor. Here, we discuss the construction process, characterize the array's radiolucency, and quantify the gain in imaging performance with respect to two clinical reference setups. The design aims to create a radiolucent anterior element that has a negligible impact on the delivered dose to allow exclusion from treatment planning, as its exact position will be unknown.

4.2 Methods

4.2.1 Design and construction

The design of the 8-channel H&N array is shown in Figure 4.1a. The array features a baseplate on which a radiotherapy mask can be secured. This baseplate contains a single, conventional (low impedance coil, $\varnothing 0.8$ mm) channel that is placed around the neck (Figure 4.1b). The 7-channel anterior element is flexible and therefore follows the shape of the immobilization mask. High impedance coils (HICs) were used to achieve the element's flexibility (Zhang et al., 2018), while radiolucency could still be preserved (Zijlema et al., 2019a; Zijlema et al., 2020). The HICs were constructed from a thin coaxial cable (AlphaWire 9432) to resonate at 63.87 MHz and were sewn onto a thin plastic frame in two rows (Figure 4.1c). This way, all electronic circuitry could be placed on the cranial and caudal sides to create a so-called radiolucent window through which can be irradiated. The channels were overlapped to limit coupling interactions with neighboring loops. Finally, a thin protective foam layer was added to cover all electronics, while keeping the attenuation low. The full H&N array (Figure 4.2) was manufactured by Tesla Dynamic Coils (Zaltbommel, the Netherlands).

The array has a (radiolucent) field of view (FOV) that ranges from the nose to the top of the shoulders. This region was chosen to cover relevant anatomies, such as the tongue, larynx, pharynx, and esophagus, where current, mask-compatible, clinical setups struggle to achieve an acceptable SNR. The anterior element of the H&N array is designed to improve the SNR in these target regions, while the posterior element is used to provide a complete body outline for radiotherapy planning and alignment purposes.

4.2.1.1 Interfacing

The array was designed for the MRigRT treatment phase on a 1.5 T MR-linac (Unity, Elekta AB, Stockholm, Sweden) but is also compatible with a 1.5 T diagnostic MRI scanner (Ingenia, Philips, Best, the Netherlands). The latter setup does require an analog-to-digital converter box (dStream, Philips).

All HICs of the H&N array were connected to matching and detuning circuitry (Figure 4.3), which was similar to that of Zijlema et al. (2020). This circuitry was connected to a preamplification board. Here, a phase-shifting network was used for preamp decoupling (Roemer et al., 1990), after which the signal can be amplified before it is forwarded to the system. Additionally, a custom malfunction board (not shown) was added to drive the active protection circuitry and terminate the scan in case of malfunctioning detuning circuitry. All signals are transferred to the system via a single connector (ODU, Mühldorf am Inn, Germany). After construction, several bench tests were performed to characterize the array's performance. These are shown in 4.7.

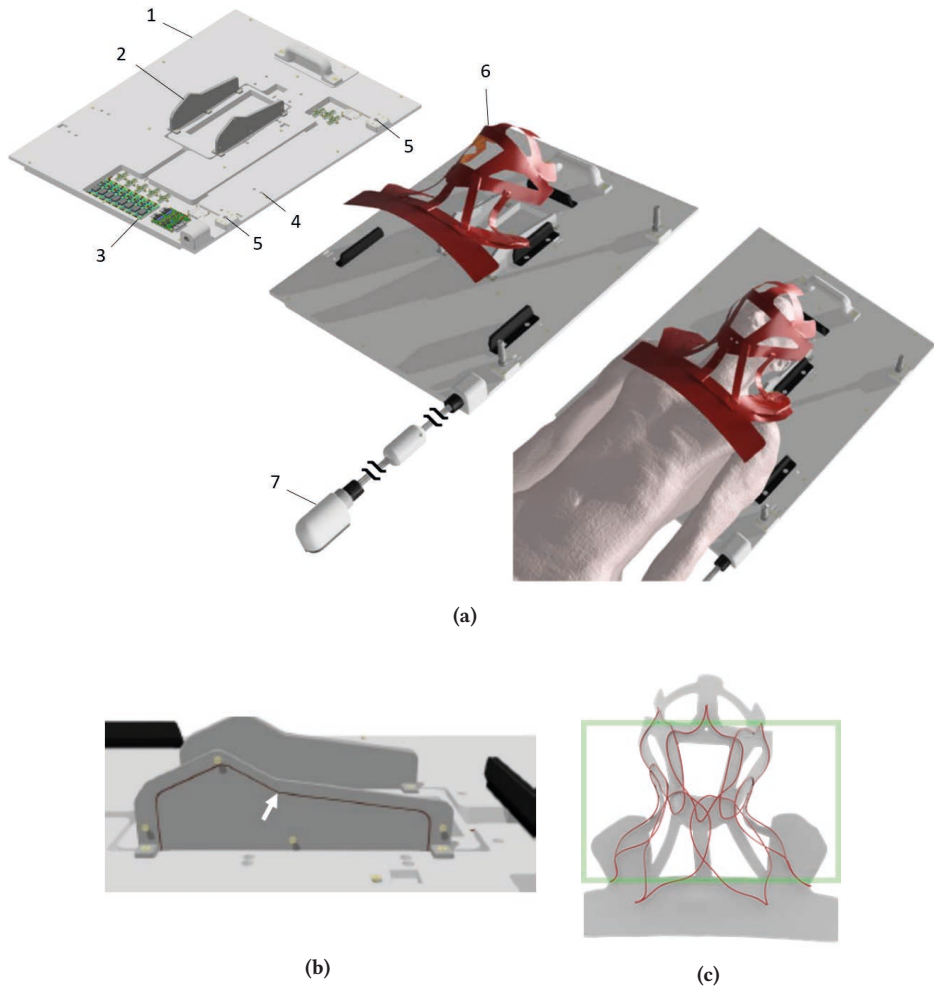


Figure 4.1 (a) Design of the mask-compatible H&N array. The posterior element (1) is a mask-compatible baseplate with one receive channel that is incorporated in the neck support holder (2). Most electronics are incorporated into the baseplate (3). A five-point radiotherapy mask can be attached using the dedicated mask holes (4). Furthermore, there are two cable entry points (5) for the 7-channel anterior element (6). These are used to route the interfacing cables of this element outside the radiolucent window. The flexible anterior element is placed onto the mask and follows its shape. A single connector (7) is connected to the MRI system. (b) Close-up of the single-channel conductor in the neck support holder of the posterior element. The conductor follows the slots between the two neck support holders and connects to its matching and detuning circuitry on the caudal side (left in this view) of the loop. (c) Placement of the seven HICs on the anterior element. The green rectangle denotes the radiolucent window, where no additional electronics are placed.

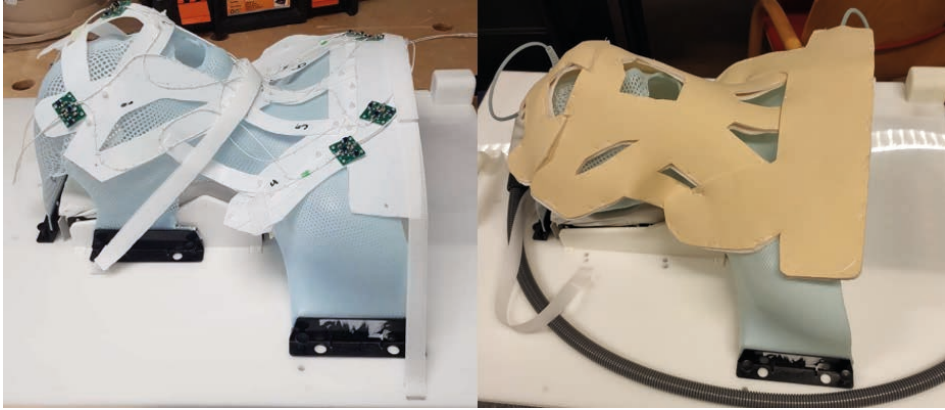


Figure 4.2 The constructed array on a radiotherapy mask without (left) and with (right) the outer foam layer of the flexible anterior element.

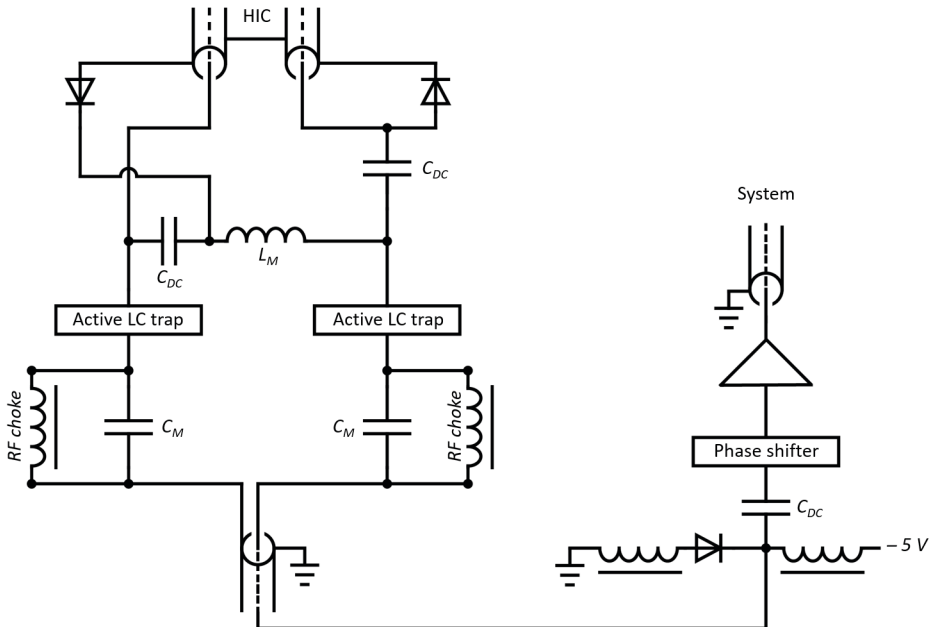


Figure 4.3 Matching, detuning, and preamplification circuitry of each channel using capacitors for matching (C_M) and DC blocking (C_{DC}) and using an inductor for matching (L_M). A total of four PIN diodes is used to detune the channel during RF excitation.

4.2.2 Dosimetry

The posterior baseplate of the array can be fixed on the treatment couch and can therefore simply be included in the treatment planning system (TPS). The anterior element, on the other hand, cannot be included in the TPS, as it is flexible and its exact position is unknown. Beam attenuation by the anterior coil therefore needs to be minimal. Here, the dosimetric impact was evaluated two-fold: single-beam attenuation and the final impact on the delivered dose of a full H&N treatment plan.

Single-beam attenuation was quantified using EPID dosimetry on a conventional linear accelerator without a magnetic field (Synergy, Elekta AB). This method has been shown to be reliable and can find small, local changes (McDermott et al., 2004; Zijlema et al., 2019a; Zijlema et al., 2020). A 90° gantry angle was used so that a 5 cm thick phantom could be placed directly against the EPID panel to simulate the impact at a depth of 5 cm. The anterior and posterior elements were then placed in front of the phantom to assess their respective impact. Beams (6 MV, 10 × 10 cm², 100 MU, 250 MU/min) were delivered and 100-frame averages (433 ms/frame) that covered the full beam delivery were recorded using XIS (PerkinElmer, Waltham, MA, USA) with all automatic corrections disabled. Five-minute waiting periods were employed between beams to avoid ghosting effects. Reference images, i.e. beam-off (dark) images and acquisitions without phantom, were used to correct and process all acquisitions (McDermott et al., 2004). The dose attenuation fraction due to an array could then be calculated per voxel as the relative percentage signal change.

Additionally, a full treatment plan was delivered on an MR-linac to estimate the clinical impact of the dose changes that are induced by the flexible anterior element. A clinical 8-beam treatment plan for a laryngeal tumor was delivered on a Delta4 MR dosimetry phantom (Scandidos AB, Uppsala, Sweden). This phantom allows for accurate dosimetry within an MR-linac and features two orthogonal detector boards that acquire dose data at 1069 locations simultaneously (de Vries et al., 2018). The treatment plan is delivered twice on the phantom alone and twice with the anterior element of the H&N array on top of the phantom. The dose readings were then averaged per setup and two clinically used quality metrics were calculated, i.e. the distance-to-agreement (DTA) pass rate (<3 mm) and gamma pass rate (3% / 3 mm).

A potential bolus effect (Ghila et al., 2016), where the anterior element on the mask significantly increases the surface dose, was considered highly unlikely, as previous work on MR-linac arrays with near-identical materials has shown that this effect is minimal for low-density arrays (Zijlema et al., 2019a). Especially when there is a slight distance between the higher-density coil materials and the patient, such as the H&N array's low-density foam layer and a radiotherapy mask, the bolus effect is minimal. Moreover, the authors showed that the treatment couch has a much larger bolus effect and is not considered problematic. Hence, the surface dose measurements have not been repeated for this specific array.



Figure 4.4 Imaging setups of the 8-channel H&N array (left), clinical MRI-simulation setup (middle), and clinical MR-linac setup (right). The imaging setups are shown on a phantom but data were acquired in-vivo.

	Characterization	Clinical: TSE	Clinical: DWI
Sequence	M2D Spoiled GE	3D TSE without/with fat suppression	Multi slice EPI, $b = [0,30,150,500]$
TR / TE	5.3 / 2.7 ms	2100 / 333 ms	4485 / 180 ms
FOV	432×432×432 mm ³	400×260×200 mm ³	300×300×120 mm ³
Voxel size	3×3×3 mm ³	1.2×1.2×2 mm ³	3.5×3.5×4 mm ³
Flip angle	10°	90°	90°
SENSE	No	Yes, $R_{AP} = 2$	Yes, $R_{AP} = 2.2$
Acq. time	03:46	4:39 / 5:02 min	4:42 min

Table 4.1 MRI sequence parameters of the performance characterization and clinically used sequences.

4.2.3 Imaging performance

The in-vivo imaging performance of the array was assessed in a volunteer after informed consent to a protocol approved by the local medical ethics committee (ID:17-010). The research was conducted in accordance with the principles embodied in the Declaration of Helsinki and consent was given for publication by the participant.

First, characterization measurements were performed on the 1.5 T MR-linac, where the performance of the 8-channel H&N array was compared to the clinical 8-channel body array (Figure 4.4). The same scan was acquired on a 1.5 T MRI-simulation scanner with a clinically used setup that combines two single-channel loop coils, a 16-channel anterior element, and a 12-channel posterior element in the table. Raw data of this characterization sequence (Table 4.1) were saved for offline analysis. The sequence was optimized to have a low sound pressure level, as the setups in the immobilization mask do not allow for the use of headphones. Earbuds (-30 dB) were used.

Additionally, data of clinically used sequences (Table 4.1) were acquired to visualize the potential clinical impact of the new array. These scans were acquired on the MR-linac and compared only the 8-channel H&N array and clinical MR-linac array.

	No coil	With H&N array
DTA pass rate* [<3 mm]	98.0%	97.4%
Gamma pass rate* (3%, 3 mm)	97.9%	97.6%
Dose difference [min, mean, max]		[-1.4%, -0.3%, 0.3%]

Table 4.2 Dosimetry statistics of the full treatment plan deliveries using the MR-compatible Delta4 phantom. All locations with a dose $\geq 20\%$ of D_{max} were included. The two dose readings per setup were averaged to improve accuracy. The dose differences per measurement point were calculated and the minimum, mean, and maximum differences are reported here. *Clinical acceptance criterion is $\geq 95\%$.

Radiation-induced SNR degradation, as described by Burke et al. (2010), is considered not to be an issue for the H&N array, as previous work with the same coil type and near-identical receive circuitry has shown that this effect was negligible (Zijlema et al., 2019a; Zijlema et al., 2020). Hence, these measurements have not been repeated for this specific array.

4.2.3.1 Data analysis

Channel coupling was assessed by calculating the Pearson correlation coefficients from the noise-only pre-scan to create a noise correlation matrix (NCM). SNR maps were generated from 3D acquisitions with a noise-only dynamic, as described by Kellman and McVeigh (2005). Coil sensitivity maps were generated from the data using ESPIRiT (Uecker et al., 2014) and g-factor maps for several acceleration factors were calculated.

4.3 Results

4.3.1 Dosimetry

EPID dosimetry attenuation maps (Figure 4.5) reveal that the anterior element of the H&N array has a relatively low attenuation. Foam packaging alone attenuates 0.1%, while single and dual layers of plastic bring the attenuation to 1.0-2.0%. A conductor wire adds another 0.7%. The posterior element attenuates significantly more: up to 21.5%.

Additionally, the full treatment plan deliveries with and without the anterior element were compared. The resulting DTA pass rates, gamma pass rates, and dose changes are reported in Table 4.2.

4.3.2 Imaging

Coupling between channels during imaging is visualized in a noise correlation matrix (Figure 4.6). Most channels of all arrays are well decoupled, though values are slightly increased for channels 6 and 7 of the clinical MR-linac array. Maximum off-diagonal

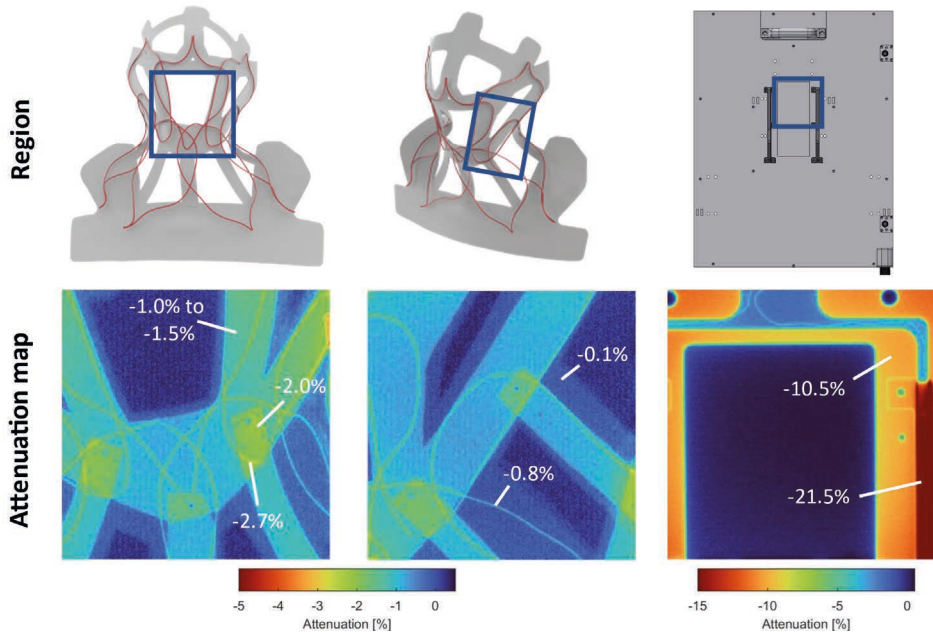


Figure 4.5 EPID attenuation maps of the anterior element (left and middle) and posterior element (right) of the H&N array. The blue rectangle denotes the FOV of the EPID measurement. Attenuation values for specific regions are denoted. Note that the color scales are different between the two elements.

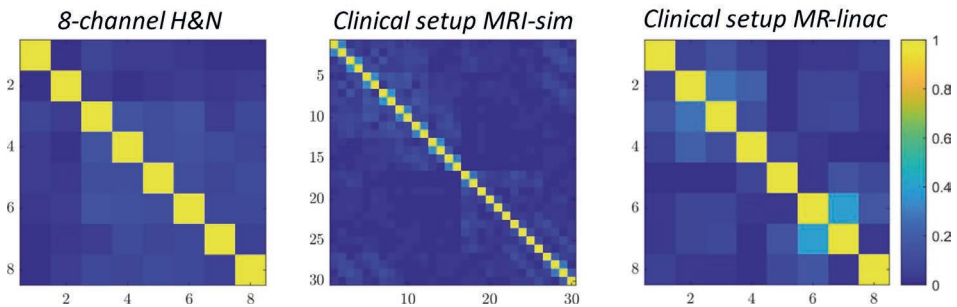
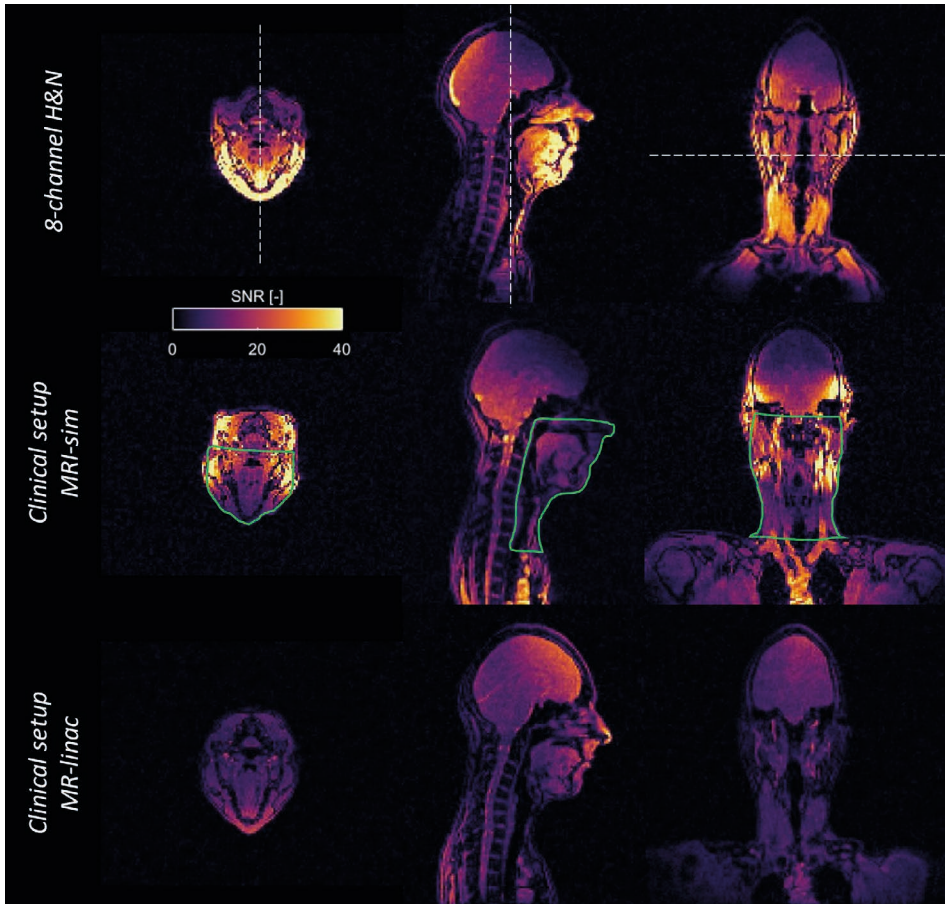


Figure 4.6 NCMs of the H&N array (left), clinical MRI-simulation setup (middle), and clinical MR-linac setup (right).

correlation coefficients were 0.14 (H&N array), 0.36 (clinical MRI-simulation), and 0.40 (clinical MR-linac). The SNR in the full H&N ROI is highest when the 8-channel H&N array is used (Figure 4.7). We found a 123% better SNR than the clinical MRI-simulation setup and 246% better than the clinical MR-linac setup. A detailed comparison for several target regions is also shown in Figure 4.7. Overall, the H&N array improves the SNR in all ROIs with respect to both clinical setups.



Reference setup →	Clinical setup MRI-simulation	Clinical setup MR-linac
Full ROI	+123%	+246%
Oropharynx	+31%	+122%
Larynx	+206%	+296%
Tongue	+159%	+202%

Figure 4.7 SNR maps of the three imaging setups. From left to right, a transverse, sagittal, and coronal slice are shown and their respective slice locations are indicated (dashed line). The full ROI is denoted in green. Slice locations and ROIs are the same for all setups. Underneath, ROI statistics of several clinically relevant ROIs. Values are relative SNR differences between the H&N array and the clinical reference setup.

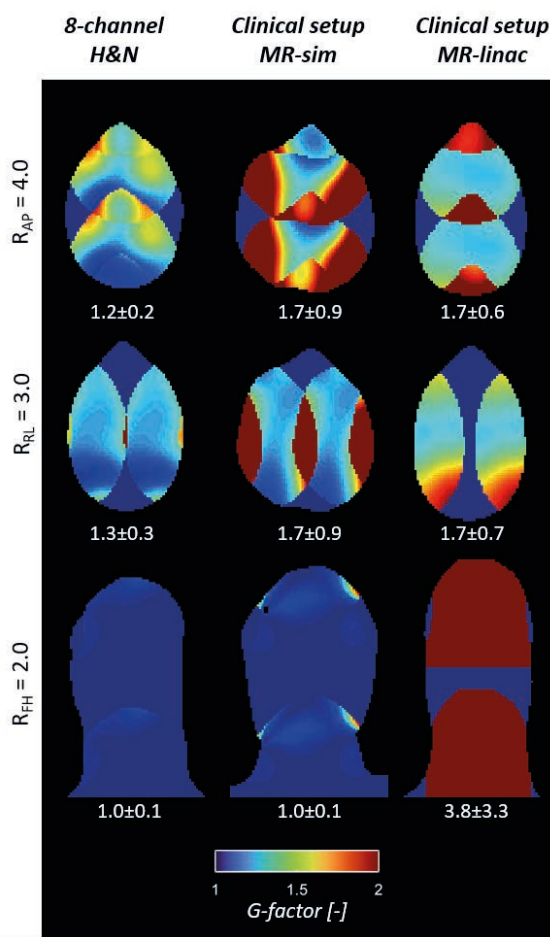


Figure 4.8 G-factor maps. Transverse (top and middle) and coronal (bottom) slices are shown for the three imaging setups. Volume statistics of the full 3D anatomy are reported underneath each slice (mean±SD).

G-factor maps for several acceleration directions are shown in Figure 4.8. G-factors are lower with the H&N array than with the clinical MR-linac setup for acceleration in all directions. The clinical MRI-simulation setup only performs similarly for FH acceleration, but is outperformed by the H&N array for LR and AP acceleration.

Anatomical in-vivo images of several clinical sequences on the MR-linac (Figure 4.9) show a clearly visible increase of the SNR with the proposed H&N array. The ADC map is smoother, which suggests a more accurate ADC fit as a result of the increased SNR.

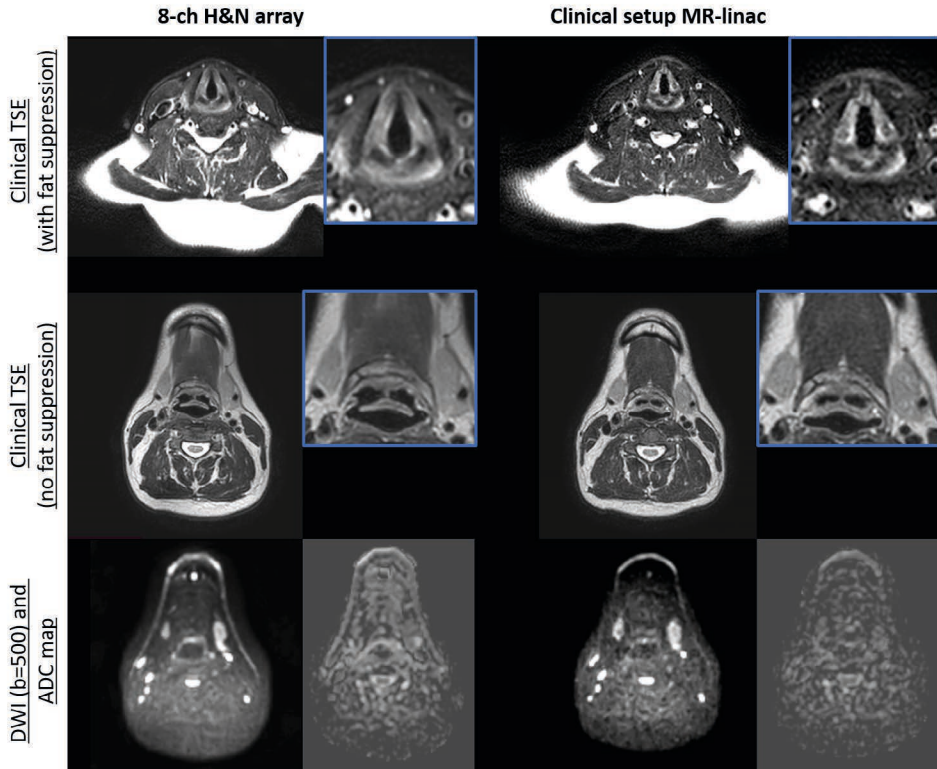


Figure 4.9 In-vivo images for three acquisitions with the 8-channel H&N array (left) and 8-channel clinical MR-linac array (right). The three sequences consisted of a TSE with fat suppression, a TSE without fat suppression, and a DWI sequence. For the latter, the $b=500$ image is shown and the calculated ADC map of that slice.

4.4 Discussion

In this work, an 8-channel H&N array was presented that is compatible with a conventional 1.5 T MRI scanner for MRI-simulation and with an MR-linac for MRI-guided radiotherapy. An immobilization mask can be secured onto the baseplate, after which the flexible anterior element is simply placed on top of the mask. Hence, subject setup with the new H&N array was found to be easy and reproducible.

The H&N array features a radiolucent window where attenuation is low and no electronics are placed. EPID dosimetry measurements confirmed that the design generally has a low attenuation and only small sections of the anterior element attenuated up to 2.7%. These slight, local underdosages from one beam were expected to be compensated by beams from other angles and therefore have no clinical impact. Indeed, a full treatment plan delivery showed that the 3%/3 mm gamma pass rates were almost identical with (97.6%) and without (97.9%) the array in place, where a gamma

pass rate $\geq 95\%$ is deemed clinically acceptable. These results suggest that the anterior element of the array does not need to be included in the treatment planning system. Nonetheless, subsequent developments should aim to further optimize the radiolucency of the support materials by removing the double plastic layers and using a thinner, single-layer mold on which the channels can be secured. Before this array can be used clinically, a more extensive assessment of multiple treatment plans should be conducted.

The imaging performance of the 8-channel H&N array is better than that of both clinical setups as a result of its close-fitting shape around the anatomy. The SNR within the ROI doubled (+123%) with respect to the MRI-simulation setup and tripled (+246%) compared to the clinical MR-linac setup. The MRI-simulation setup theoretically consists of 30 channels, but 12 of the 16 anterior element's channels are hardly used, as these are positioned too far caudally from the ROI. Additionally, the posterior element's distance from the anatomy is relatively large. Consequently, most of the SNR in the ROI comes from the two loop coils at the sides of the head. The clinical MR-linac setup has large loops that are positioned relatively far from the anatomy of interest, which limits its SNR.

The increased SNR of the proposed array resulted in visible improvements of all in-vivo scans (Figure 4.9). Anatomical images have a reduced noise level and the ADC map is smoother, which suggests a more accurate ADC fit. Similarly, other quantitative methods, such as T_1 and T_2 mapping, can also benefit from the improved SNR. More accurate quantitative values are becoming increasingly useful now that clinical trials are investigating the use of such methods to monitor treatment response or to guide dose painting strategies (Liu et al., 2021; Yan et al., 2021). Acquisition of these scans on the MR-linac during each fraction would be ideal. Currently, the MR-linac's DWI capabilities are limited but the proposed array may open up new possibilities. For example, due to the improved SNR, the array may allow for higher b-values than the current limit of 500 s/mm^2 without reaching the noise floor (Kooreman et al., 2020).

In terms of acceleration performance, the 8-channel H&N array also performs best. The clinical MRI-simulation setup only has two loop coils to cover most of the ROI and quickly pays a price in terms of the g-factor when acceleration factors are increased. The clinical MR-linac setup is outperformed by the H&N array in all directions. Therefore, the H&N array is an improvement on both machines. Hence, the array may allow for further improvements of DWI acquisitions, as higher acceleration factors reduce the EPI train length and thereby geometric distortions.

Imaging performance could be further improved by adding more channels. Both scanners allow for easy connection of at least 12 channels without requiring any hardware adaptations to the receive chain. Combined with slightly larger channels, this would allow for an increase of the imaging FOV, e.g. to also include the brain and supraclavicular lymph nodes. The slightly larger channels would also further improve the SNR at depth. Moreover, this approach would increase the radiolucent FOV, which

is currently limited to 22 cm in the craniocaudal direction. Hence, MRIgRT treatments in a larger anatomical region could profit from the improved array.

A limitation of the current prototype is that it is compatible with only one type of mask, as the attachment holes in the baseplate are cut out at specific locations for this mask type only. However, the baseplate could be adapted relatively easily by cutting out additional mask attachment holes. A two-piece mask, i.e. consisting of a separate top and bottom piece, would require more thorough adaptations of the design.

This array is designed for 1.5 T systems, which are most common in imaging centers and suffer less from susceptibility-induced geometrical distortions than 3 T scanners, which is especially beneficial for the radiotherapy application. However, some institutes may use 3 T scanners for MRI-simulation. A 3 T H&N array could be manufactured by adapting the presented design, although the resulting array can be used for MRI-simulation only, as none of the currently available MR-linacs feature a 3 T magnet. This limits the array's applicability but removes the radiolucency constraint, thus relaxing those design restrictions.

As discussed before, future work should aim to increase the H&N array's channel count and FOV, and to further improve and validate its radiolucency. Additionally, other coil types could be investigated, such as screen-printed coils (Corea et al., 2016). These loops can be very thin and can also be tuned without the use of lumped elements. If the array does not need a rigid support structure, this can potentially result in a high radiolucency, albeit at the cost of a slightly reduced SNR and more inter-channel coupling than HICs. Finally, the applicability of the H&N array for PET/MRI could be investigated, as MRIgRT arrays have been shown to be beneficial for hybrid PET/MRI imaging (Zijlema et al., 2021). In PET/MRI, the number of PET tracer photons that are attenuated or scattered should be minimized to optimize the accuracy and SNR. MRIgRT arrays, such as the proposed H&N array, have been designed to be radiolucent and will therefore also attenuate fewer PET tracer photons than a conventional array. Zijlema et al. (2021) also noted that a pre-treatment PET/MRI scan followed by an MR-linac treatment, i.e. an MR-only workflow without CT, could benefit from an array that is compatible with both machines. Image quality will be comparable, which will simplify sequence optimization and inter-scanner image comparison.

4.5 Conclusion

The presented 8-channel H&N array allows for imaging during the pre-treatment MRI-simulation phase and MRI-guided treatment phase on an MR-linac. Imaging performance improved considerably for both applications, while patient setup is easy and robust. Beam attenuation is low and does not seem to have a clinically significant impact.

4.6 Acknowledgements

This work is part of the research program HTSM with project number 15354, which is financed by the Netherlands Organization for Scientific Research (NWO) and Philips Healthcare.

4.7 Appendix: Bench measurements

Methods

The performance of the new 8-channel H&N array was assessed using bench measurements. A phantom was placed in the coil and a full S-parameter matrix was measured. Furthermore, the loaded and unloaded Q-factors were measured by capping off the coaxial signal cable from the matching board with 50Ω . The channel numbers are shown in Figure 4.10.

Results and discussion

The results of the bench measurements are shown in Table 4.3. $S_{1,1}$ values were at least -27 dB, which indicates a successful tuning and matching. Inter-channel coupling was also well resolved, as $S_{i,j}$ values were generally low and slight bending of the array did not notably affect these values. The measured loaded Q-factors ranged from 15 to 17, while the unloaded Q-factors ranged from 17 to 19. Hence, the array is not very sensitive to load changes. Q-factors are relatively low due to the 50Ω caps.

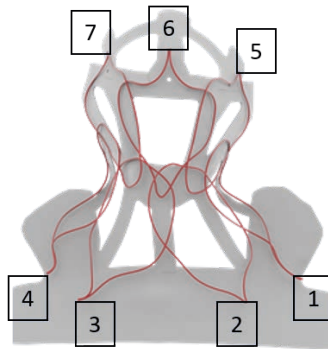


Figure 4.10 Channel layout of the anterior element of the H&N array. The eight channel is the channel in the baseplate, as shown in Figure 4.1.

	1	2	3	4	5	6	7	8
1	-27	-18	-22	-23	-14	-14	-23	-24
2	-18	-32	-37	-19	-22	-17	-18	-26
3	-22	-36	-27	-14	-17	-16	-20	-31
4	-23	-19	-14	-31	-28	-19	-25	-30
5	-14	-22	-17	-29	-32	-28	-17	-20
6	-14	-17	-16	-19	-29	-37	-22	-31
7	-23	-18	-20	-26	-17	-22	-37	-22
8	-27	-27	-31	-30	-20	-30	-23	-32

Table 4.3 S-parameter matrix of the 8-channel H&N array. Values on the diagonal are $S_{1,1}$ measurements and off-diagonal values are $S_{i,j}$ measurements. All values are in dB.

CHAPTER 5

Minimizing the need for coil attenuation correction in integrated PET/MRI at 1.5 T using low-density MR-linac receive arrays

The following chapter is based on:

Zijlema, S. E., Branderhorst, W., Bastiaannet, R., Tijssen, R. H. N., Lagendijk, J. J. W., & van den Berg, C. A. T.. (2021). Minimizing the need for coil attenuation correction in integrated PET/MRI at 1.5 T using low-density MR-linac receive arrays. *Physics in Medicine & Biology*, 66(20), 20NT01.

Abstract

Background The simultaneous use of positron emission tomography (PET) and magnetic resonance imaging (MRI) requires attenuation correction (AC) of photon-attenuating objects, such as MRI receive arrays. However, AC of flexible, on-body arrays is complex and therefore often omitted. This can lead to significant, spatially varying PET signal losses when conventional MRI receive arrays are used. Only few dedicated, photon transparent PET/MRI arrays exist, none of which are compatible with our new, wide-bore 1.5 T PET/MRI system dedicated to radiotherapy planning.

Purpose In this work, we investigated the use of 1.5 T MR-linac (MRL) receive arrays for PET/MRI, as these were designed to have a low photon attenuation for accurate dose delivery and can be connected to the new 1.5 T PET/MRI scanner.

Methods Three arrays were assessed: an 8-channel clinically-used MRL array, a 32-channel prototype MRL array, and a conventional MRI receive array. We experimentally determined, simulated, and compared the impact of these arrays on the PET sensitivity and image reconstructions. Furthermore, MRI performance was compared.

Results Overall coil-induced PET sensitivity losses were reduced from 8.5% (conventional) to 1.7% (clinical MRL) and 0.7% (prototype MRL). Phantom measurements showed local signal errors of up to 32.7% (conventional) vs. 3.6% (clinical MRL) and 3.5% (prototype MRL). Simulations with data of eight cancer patients showed average signal losses were reduced from 14.3% (conventional) to 1.2% (clinical MRL) and 1.0% (prototype MRL). MRI data showed that the signal-to-noise ratio of the MRL arrays was slightly lower at depth (110 versus 135). The parallel imaging performance of the conventional and prototype MRL arrays was similar, while the clinical MRL array's performance was lower.

Conclusions MRL arrays reduce in-vivo PET signal losses $>10\times$, which decreases, or eliminates, the need for coil AC on a new 1.5 T PET/MRI system. The prototype MRL array allows flexible coil positioning without compromising PET or MRI performance. One limitation of MRL arrays is their limited radiolucent PET window (field of view) in the craniocaudal direction.

5.1 Introduction

The simultaneous use of positron emission tomography (PET) and magnetic resonance imaging (MRI) requires attenuation correction (AC) of photon-attenuating objects to avoid PET reconstruction errors. However, AC of on-body (surface) arrays is complex, as the positions of the array's attenuating structures are variable and in general unknown. Several methods have been proposed to solve this issue but these left residual errors or required external hardware (Eldib et al., 2015; Frohwein et al., 2018; Kartmann et al., 2013; Paulus et al., 2012). Therefore, AC of surface arrays is often omitted, even though this can lead to significant, spatially varying, PET signal losses when conventional MRI receive arrays are used (Fürst et al., 2014; Tellmann et al., 2011). Consequently, the accuracy of quantitative measurements can be greatly reduced, e.g. when PET imaging is used to reconstruct the delivered dose of a radioembolization treatment (Bastiaannet et al., 2018; Braat et al., 2018). Moreover, the resulting reconstruction errors could result in misdiagnoses, e.g. when the signal of a small lesion, such as a metastasis, is reduced such that it is lost in the noise, or when a patient's treatment response is wrongly classified due to a lower measured activity (Wahl et al., 2009).

Hence, it would be preferable to use a receive array that is designed to have a low photon attenuation and avoid all aforementioned issues. A limited number of dedicated PET/MRI arrays have been developed (Dregely et al., 2015; Farag et al., 2019; Sander et al., 2015) but dedicated arrays are not available for all systems, hence photon attenuating conventional arrays are used.

An example of a system for which no dedicated PET/MRI arrays are available is the new 1.5 T PET/MRI system that is currently being developed and constructed at our institute. This wide-bore system is designed for use as a single-exam planning tool for MRI-guided radiotherapy (MRIgRT) treatments on the 1.5 T MR-linac (MRL), thereby eliminating the need for separate MRI and PET/CT scans and improving the geometric accuracy compared to 3 T systems (Branderhorst et al., 2020; UMC Utrecht, 2021). Interestingly, receive arrays of the MRL can also be connected to the new PET/MRI system and these arrays have been designed for optimal photon transparency (radiolucency) to limit dose deviations during MRIgRT treatments. Hence, there is a clear synergy between the (radiolucency) requirements for MRL and PET/MRI receive arrays. One major difference between the two techniques is the lower photon energy of PET: 511 keV versus a 7 MV spectrum for the MRL. The lower photon energy of PET may increase the photon attenuation fractions with respect to MRIgRT. Nonetheless, attenuation of MRL arrays is still expected to be significantly lower than of conventional MRI arrays.

Using the same receive arrays on the MRL and PET/MRI system would also be advantageous for the MRIgRT workflow. It would ensure a consistent image quality between the pre-treatment stage (PET/MRI) and the treatment delivery stage (MRL), especially as both systems feature the same 1.5 T field strength, split-gradient coil design, and software platform. This will allow the use of identical MRI sequences, which will simplify MRI protocol development and can improve the accuracy of image registration.

In this work, we investigated if MRL arrays are indeed suitable for use on a new 1.5 T PET/MRI system. We evaluated two MRL arrays and compared their performance to a conventional surface array. We experimentally determined, simulated, and compared the impact of two MRL arrays and one conventional MRI array on the PET sensitivity and image reconstructions. Furthermore, we compared the MRI performance. We intended to assess if MRL arrays can reduce PET reconstruction errors to a level that coil AC is not required for most applications, while imaging performance remains similar.

5.2 Methods

5.2.1 Receive arrays

The two MRL receive arrays were developed for use on a 1.5 T MR-linac (Unity, Elekta AB, Stockholm, Sweden), which is built on the Philips (Best, the Netherlands) MRI platform. The first array is the 8-channel clinical array (Hoogcarspel et al., 2018), which is elevated above the patient and features a 40 cm window with low-attenuative properties, i.e. the radiolucent PET window (Figure 5.1). The second array is a flexible 32-channel surface array (Zijlema et al., 2020), which was developed in collaboration with Tesla Dynamic Coils (Zaltbommel, the Netherlands) to enhance the MR-linac's imaging capabilities in terms of signal-to-noise ratio (SNR) and parallel imaging (acceleration) performance. As a reference, a conventional (non-PET) diagnostic MRI receive array (Philips dStream Torso) is tested.

5.2.2 Impact on PET reconstructions

All PET scans were performed on a PET/CT system (Biograph mCT 40, Siemens Healthcare, Erlangen, Germany), as the 1.5 T PET/MRI scanner at our institute was not operational yet. This way, CT information of the MRI receive arrays was available and could be used for AC. Conversion of CT scans to μ -maps and all PET image reconstructions were performed using E7 tools (Siemens Molecular Imaging, Knoxville, USA). First, phantom data were acquired and the arrays' impact was quantified. Lastly, patient data were used to simulate the in-vivo impact of the arrays.

5.2.2.1 Phantom scans

A cylindrical Ge-68 source (\varnothing 20 cm, total activity: 74.55 MBq) was placed on a wooden frame on the PET/CT patient bed. The wooden frame allowed for placement of the arrays on top and below the phantom without changing the phantom's position. A reference PET/CT scan was made with this setup. Then, the scan was repeated for each array in two configurations: anterior element-only and anterior and posterior element combined (Figure 5.2). The posterior element of the conventional array could not be studied, as it is fixed in the patient couch of the MRI scanner. The conventional array induced major streaking artifacts in the CT scan, hence a metal artifact reduction algorithm from the

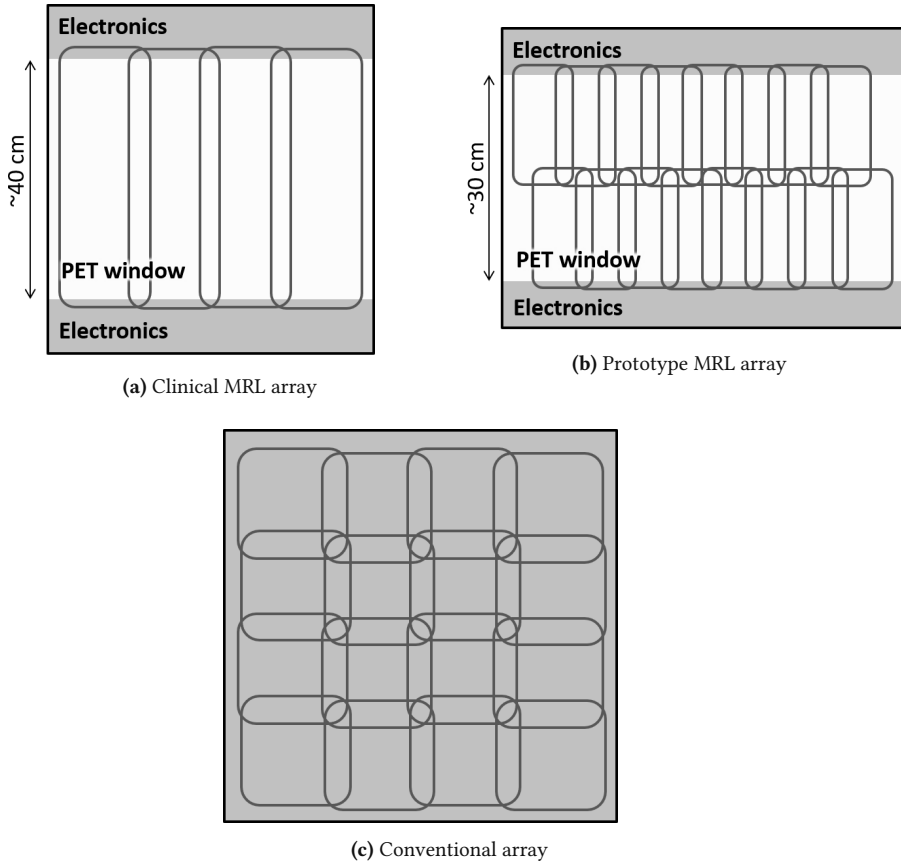


Figure 5.1 (a) Design of the 4-channel anterior element of the clinical MRL array, which features a 40 cm radiolucent PET window that does not contain electronic components. (b) The prototype MRL array. The depicted 16-channel element features a 30 cm radiolucent PET window. (c) The 16-channel anterior element of a conventional MRI scanner. Electronics are distributed all over its surface, i.e. there is no radiolucent PET window. Relative image sizes approximate the size differences between the arrays. The widths of the arrays are ~40 cm (clinical MRL), ~60 cm (prototype MRL), and ~55 cm (conventional).

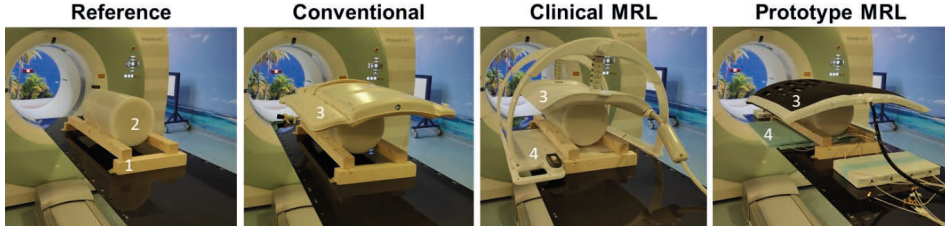


Figure 5.2 Setup of the PET/CT measurements. A wooden frame is positioned (1) on which the cylindrical source (2) is placed. Anterior (3) and posterior (4) elements could be placed without position changes of the source. The reference scan is performed without a receive array present. The anterior element-only setups of the clinical MRL and prototype MRL arrays are not shown but were also tested.

manufacturer was used for this scan. The raw PET data of the phantom measurements were saved and analyzed.

Overall PET sensitivity loss due to coil placement was estimated using the raw data. For each scan, the number of true coincidences was extracted. The sensitivity loss was then calculated as the percentage reduction between each configuration of the source with receive array(s) and the reference scan without a receive array (Figure 5.2).

Then, the impact of each of the anterior elements on the reconstructed PET activity distribution was quantified spatially. Inter-scan differences of the PET signal per voxel were up to 10%, too large to do a voxel-wise comparison between a scan with and a scan without each array. Therefore, a single-scan approach was used, where the same PET data were reconstructed twice, but with a different CT for AC. This method is visualized in Figure 5.3. A copy of the original CT with array (CT_{original}) was created in which the coil was manually segmented and masked to be air (CT_{masked}). Then, two PET reconstructions with time-of-flight and point spread function modeling (PSF-TOF) were performed: once using CT_{original} ($I_{\text{coil AC}}$) and once using CT_{masked} ($I_{\text{no coil AC}}$) for AC. The relative difference per voxel between these two reconstructions represents the spatial impact of each anterior element:

$$\Delta = \frac{I_{\text{no coil AC}} - I_{\text{coil AC}}}{I_{\text{coil AC}}} \times 100 \quad (5.1)$$

If this coil-induced difference is sufficiently low, i.e. only a few percent, most applications will not require AC. The impact of the posterior elements was not studied in this analysis, since their geometries and positions are fixed and known, thus allowing for accurate template-based AC.

The impact of the receive array setups is studied by simulating acquisitions with and without the anterior element on the patient using E7 tools. Similar to the phantom measurements, the impact of the posterior elements was not studied, as these allow for accurate template-based AC.

The workflow of the patient scan simulations is shown in Figure 5.4. First, the original PET image was reconstructed using the original CT and sinogram to obtain the “PET image as acquired” (1). Subsequently, the receive arrays were extracted from the phantom CTs of section 5.2.2.1 and added to the original patient CT using MATLAB (Mathworks, Inc., Natick, USA) to generate the patient “CT with coil added”. These new CT images and the original sinograms were transferred to the E7 tools environment and converted to μ -maps. Subsequently, a PET acquisition was simulated by forward projecting the original PET activity distribution with attenuation based on the CT with coil. The result is a sinogram as if we would have prospectively scanned a patient with the array present (2).

The simulation process included modeling of spatial resolution, scattered events, and Poisson noise. This implementation was similar to that described by Pfaehler et al. (2018), except that randoms information was used from the original patient data. Scatter data were generated using a 5 cm FWHM Gaussian kernel and a scatter fraction of 20%. This fraction was chosen relatively low to compensate for the fact that each bed position was simulated separately, which reduced the scatter component from outside the field of view (FOV).

This simulation process resulted in a new sinogram that was then used in two PSF-TOF reconstructions: one where the original CT without coil was used for AC (no coil AC) (3) and one where the CT with coil was used (4). Standardized uptake value (SUV) images were obtained by normalizing to the body weight and injected dose. The relative change between these two PET reconstructions was again calculated with Equation 5.1 (5). Finally, the primary tumor was manually segmented and the relative signal change within this volume was determined. These last three steps are identical to the experimental method from Figure 5.3.

The full method that is shown in Figure 5.4 was validated with experimental data from phantom measurements in 5.6. Here, the projection (patient) method is compared to the experimental (phantom) method from Figure 5.3, which is used as the gold standard.

5.2.3 MRI performance assessment

The following three setups were compared: (i) the 8-channel clinical MR-linac (MRL) array, (ii) the 32-channel prototype MRL array, and (iii) the 28-channel conventional array. All setups consisted of an anterior and posterior element.

The MRI performance was assessed by comparing the SNR and parallel imaging (acceleration) performance of the setups. SNR maps were generated from phantom

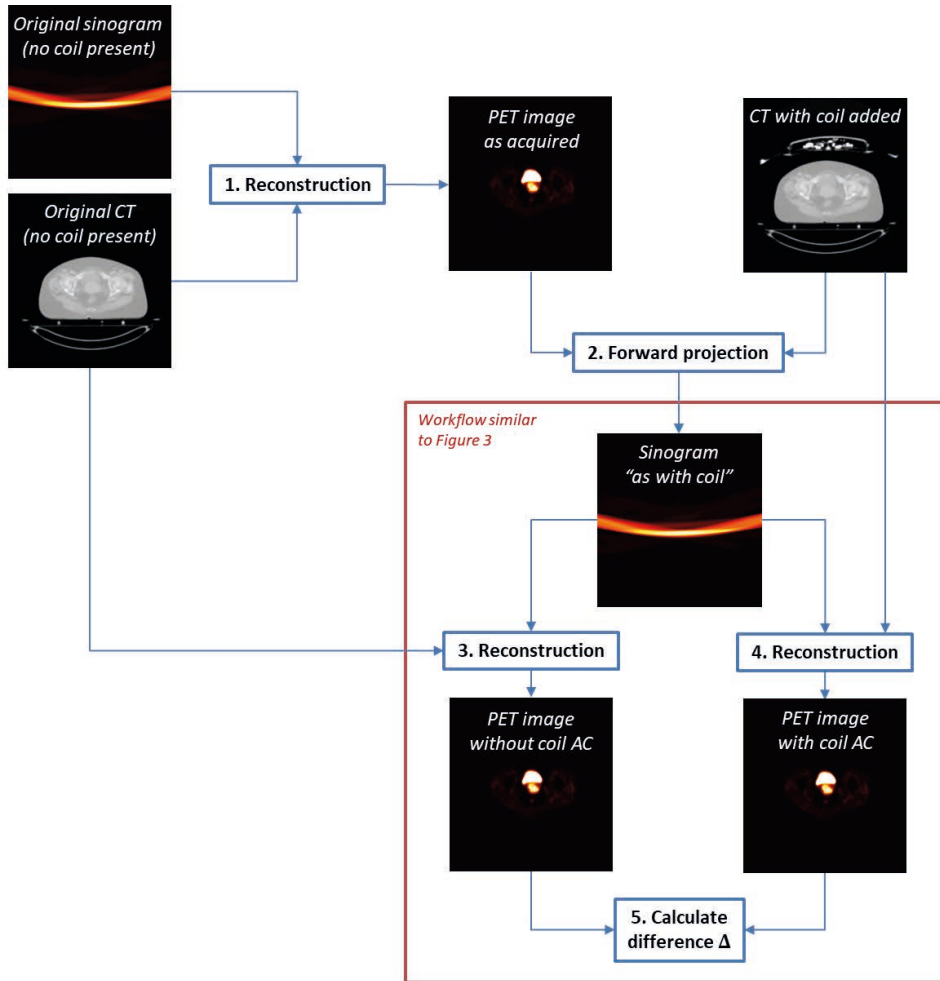


Figure 5.4 Workflow of receive array impact analysis. (1) The original PET image was reconstructed using the clinical PET/CT data. (2) A receive array was added to the original CT to create a CT with coil. Then, a PET acquisition was simulated by forward projecting the original PET activity distribution with attenuation based on the CT with coil. The resulting sinogram is the sinogram as it would have been detected if a coil were present. In other words, this is the PET sinogram data as if a patient was prospectively scanned with an array. (3,4) Reconstructions of this new sinogram were performed, both without (3) and with (4) the coil in the AC-CT. (5) From these two reconstructions, a difference map can be calculated that shows the influence of a receive array on the reconstructed PET images. After step 2, this method is identical to the experimental method from Figure 5.3.

(PVP- and agar-based, 2.6% NaCl) scans (3D spoiled gradient echo, FOV = 450×250×250 mm³, TR/TE = 10.0/1.8 ms, FA = 20°), including a noise-only scan (Kellman & McVeigh, 2005). The coil sensitivity maps were used to assess the acceleration performance of the arrays by obtaining g-factor maps (Pruessmann et al., 1999) on the scanner for several undersampling factors and directions. Due to interfacing differences between the three arrays, data of the MRL arrays were acquired on a 1.5 T MR-linac, whereas data of the conventional array were acquired on a conventional MRI scanner (Ingenia, Philips, Best, the Netherlands). However, the systems have very similar characteristics and perform approximately equally.

5.3 Results

5.3.1 PET studies

5.3.1.1 Impact on phantom scans

The overall sensitivity loss due to the anterior element of the conventional array was 8.5%, as determined by comparing the true coincidences with and without the element present. This loss was reduced to 1.7% and 0.7% when the anterior elements of the clinical and prototype MRL arrays were used, respectively. When both anterior and posterior elements of the MRL arrays were used, these sensitivity losses increased to 4.0% and 2.3%.

The spatial impact of each array's anterior element on the reconstructed activity in a homogeneous phantom is shown in Figure 5.5. The relative changes vary in space, with greater changes in regions closer to the array (positioned on top of the phantom). Relative differences up to 32.7% were found for the conventional array, versus 3.6% and 3.5% for the clinical and prototype MRL arrays, respectively. Overall, the MRL arrays reduced errors by 8.5 to 10×.

5.3.1.2 Impact on patient scans

An example of the impact of the arrays on a patient's scan is shown in Figure 5.6. A severe reduction of the PET signal is visible under the conventional array, while the MRL arrays only induce minor changes. Within the tumor (25 cc), the conventional array reduces the signal by 17.2%, while the clinical and prototype MRL arrays bring this back to 1.4% and 0.2%, respectively. Statistics of the signal (SUV) changes in the primary tumor of all patients are presented in Table 5.2.

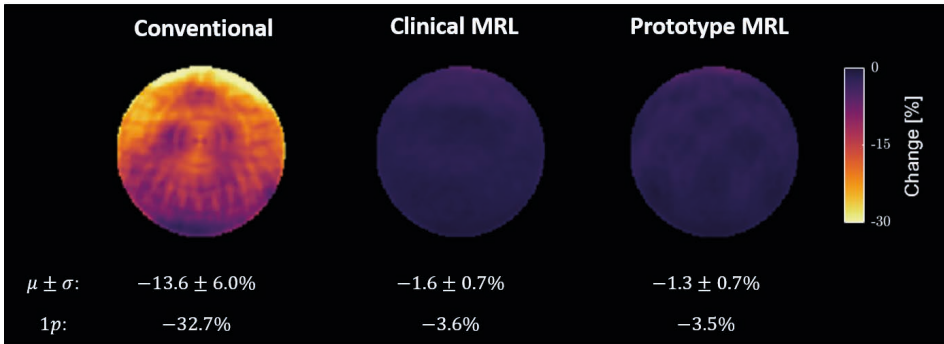


Figure 5.5 Spatial PET activity changes Δ in the transverse plane due to the conventional, clinical MRL, and prototype MRL arrays on top of the phantom (anterior elements only). The mean (μ), standard deviation (σ), and first percentile (1p) are calculated in the whole phantom.

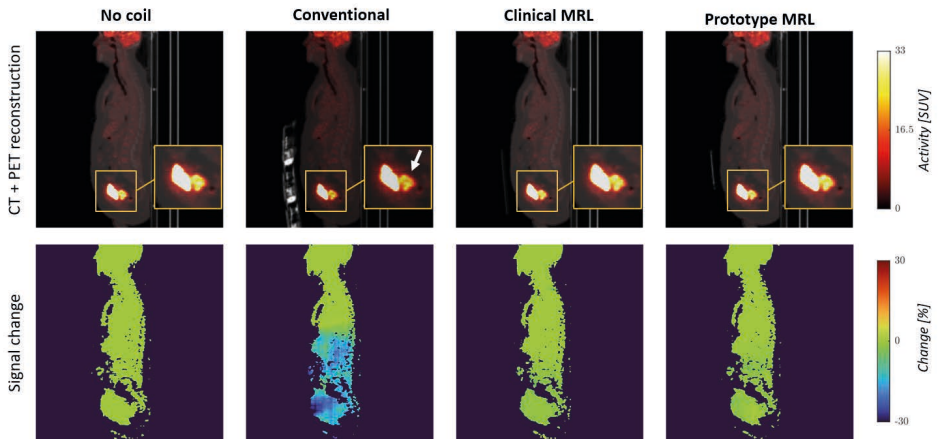


Figure 5.6 Example of each coil's impact on the PET reconstructions of a representative prostate cancer patient (patient 1). Top row: PET reconstructions displayed on top of the CT with coil. The conventional array visibly reduces the PET signal in the tumor (white arrow), while the signal was similar when the MRL arrays are used. The bright structure to the left of the tumor is the bladder. Bottom row: relative change of the PET signal. Only regions with sufficient PET signal are shown to avoid noise amplification.

Patient	Conventional	Clinical MRL	Prototype MRL
1	-17.2±2.9 %	-1.4±0.2 %	-0.2±0.6 %
2	-15.1±3.6 %	-1.5±0.2 %	-1.5±0.6 %
3	-12.7±1.9 %	-1.3±0.1 %	-0.8±0.2 %
4	-15.8±4.9 %	-1.2±0.2 %	-1.8±0.5 %
5	-14.1±2.1 %	-1.3±0.3 %	-0.2±0.7 %
6	-10.7±1.6 %	-1.1±0.2 %	-0.8±0.3 %
7	-13.1±2.5 %	-0.7±0.3 %	-1.2±0.3 %
8	-16.0±1.3 %	-1.4±0.1 %	-1.3±0.3 %
Population:	-14.3±2.1 %	-1.2±0.3 %	-1.0±0.6 %

Table 5.2 SUV changes within the primary tumor due to the anterior element of a receive array. Changes are reported per patient and for the whole population (mean±SD).

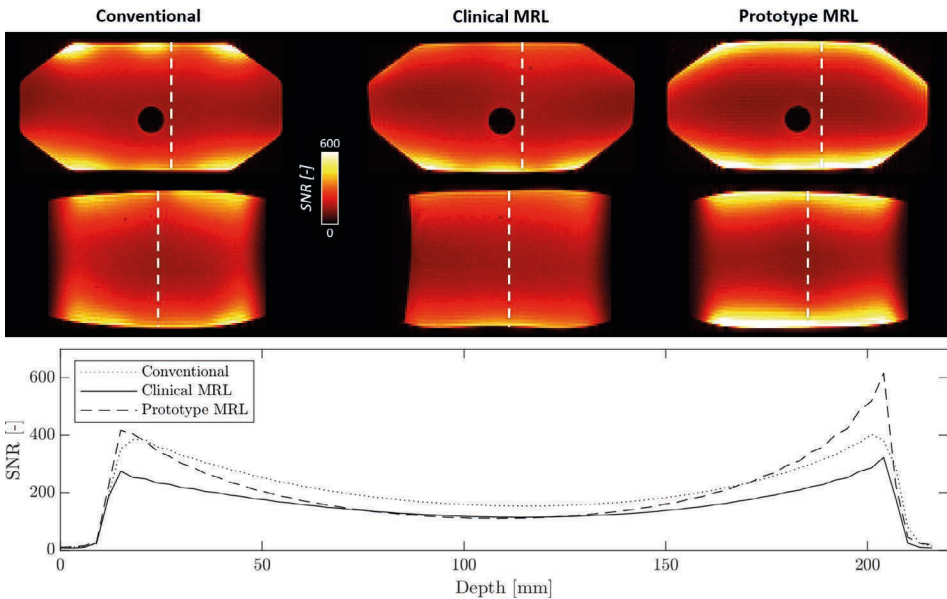


Figure 5.7 Top: MRI SNR maps of the 3D phantom scans. The SNR maps from the MRL arrays are adapted from Zijlema et al. (2020). The white line represents the location of the orthogonal slice. Bottom: SNR profiles through the phantom.

5.3.2 MRI performance

Figure 5.7 shows the SNR maps that were obtained using the three arrays. The SNR is highest at the surface, where the conventional and prototype MRL perform best. At depth, the SNR of the conventional array is approximately 135, whereas both MRL arrays produce an SNR of around 110.

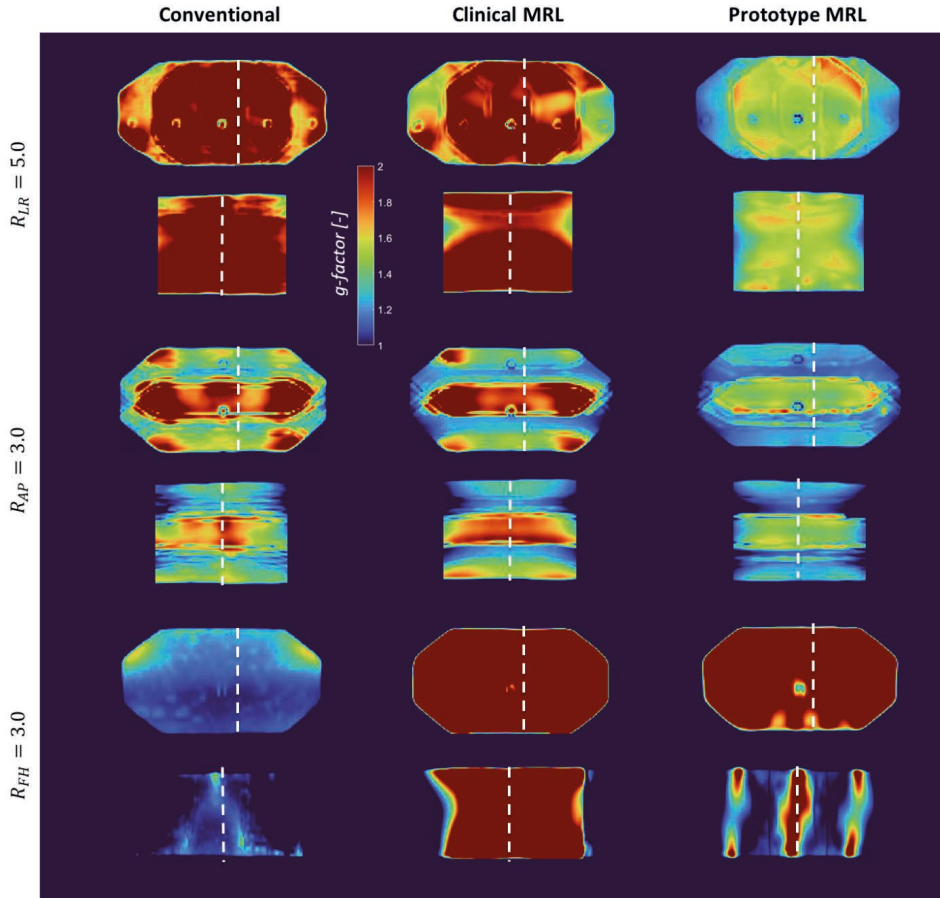


Figure 5.8 G-factor maps comparing the acceleration performance of the three arrays for several acceleration factors R . Transverse and sagittal slices are shown. The white line represents the location of the orthogonal slice. Note that the g-factor map of the prototype MRL array at $R_{FH} = 3.0$ is elevated especially in the chosen transverse slice but not in most other slices.

Figure 5.8 displays the g-factors maps for several acceleration factors. Acceleration performance of the prototype is slightly better in LR-direction, whereas the conventional array produces lower g-factors when acceleration is applied in FH-direction.

5.4 Discussion

In this work, we investigated the impact and feasibility of using MR-linac (MRL) arrays on a new 1.5 T PET/MRI system. Three MRI receive arrays were compared: one conventional diagnostic array and two arrays that were developed for MRigRT on an MRL.

First, the impact of the arrays on the PET sensitivity was assessed. Phantom measurements showed that placement of the MRL arrays resulted in an overall sensitivity loss that was up to 12× lower than with the conventional array (0.7% and 1.7% vs. 8.5%). Similar differences were observed when the impact was quantified spatially: the conventional array led to changes of up to 32.7% while the prototype and clinical MRL arrays induced maximal signal changes of only 3.5% and 3.6%, respectively. The distribution of signal changes is non-uniform, where the largest changes are induced near the surface on which the array was placed. This finding is in agreement with Kartmann et al. (2013) and was to be expected, as the number of affected lines of response is largest close to the array. Photon attenuation of the prototype MRL array was lower than with the clinical MRL array, even though the channel count was higher, which can be explained by the different support structure. The anterior element of the prototype MRL array is flexible and therefore does not require a strong support structure, while the clinical MRL array is rigid and, consequently, its support structure attenuates more. However, its rigid and immobile design may allow for template-based AC, which can further reduce its impact, albeit at the cost of workflow complexity.

Analysis of in-vivo data of eight cancer patients confirmed these findings. The conventional array induced large errors, while the MRL arrays kept these to a minimum. Within the primary tumor, errors were reduced from 14.3% (conventional) to 1.2% (clinical MRL) and 1.0% (prototype MRL), i.e. a more than ten-fold reduction. These findings are in accordance with literature, e.g. with the findings from Deller et al. (2021), whose lightweight array also reduced signal errors, albeit only by half (9.0% to 4.3%). These residual errors are still >3× (phantom) or >4× (in-vivo) higher than we achieved with the prototype MRL array. This difference is likely due to the fact that their lightweight array is not specifically developed with radiolucency in mind. Consequently, the array contains more attenuating structures, such as electronics, in the PET window.

Finally, the MRI performance was compared between the three arrays. The SNR was highest at the surface, where the conventional and prototype MRL performed best. At depth, the SNR of the conventional array was slightly higher than the SNR of the MRL arrays (135 versus 110). This difference may partially be due to the fact that data were acquired on two different MRI systems, as explained in section 5.2.3. Parallel imaging (acceleration) performance, which is essential to fast imaging for motion correction, was similar for the conventional and prototype MRL arrays, although results varied per acceleration axis. Acceleration performance in LR-direction was better with the prototype MRL array, while the conventional array produced lower g-factors when acceleration was applied in FH-direction. The different channel layouts (Figure 5.1b,c) explain this finding: more channels in a certain direction generally allow for higher acceleration factors. As the clinical MRL array features relatively few channels, its acceleration performance was lower than the other arrays. However, the array still significantly reduced PET photon attenuation and is capable of capturing 2D motion or slower 3D motion (de Muinck Keizer et al., 2019).

Our findings have several consequences for clinical practice using a 1.5 T PET/MRI system. We confirmed that conventional arrays have a severe impact on the PET signal. The high signal errors, e.g. within tumors, degrade the reliability for any application that requires (semi)quantitative values, such as diagnosis, disease staging, treatment response monitoring, or radioembolization dose reconstructions. The use of an MRL array significantly reduces signal errors to a level that is safer to disregard, hence AC will not be necessary for most applications. As a result, clinical workflows can remain simple, while PET sensitivity is drastically improved. In addition to the improved PET sensitivity, the ability to perform motion correction using the MRI data may improve the detection of small lymph nodes and metastases, which is beneficial for e.g. radiotherapy planning (Freitag et al., 2016; Samołyk-Kogaczewska et al., 2019). Especially in mobile sites with (respiration-induced) motion, motion correction could correct uptake values that would otherwise end up considerably lower, or even disappear in the background, due to motion blurring. This way, detection of small lesions, e.g. metastases and lymph nodes, will be more accurate. Fast (3D) motion correction is especially important for respiratory motion, which is possible with the prototype MRL array.

To sum up, the conventional receive array can scan fast enough to correct for motion but its placement can induce spatially varying reconstruction errors of up to 32.7%. In comparison, both MRL arrays bring errors down to under 4%. While this is the case for both MRL arrays, only the 32-channel MRL prototype combines a low attenuation with fast imaging capabilities and therefore performs best overall.

One limitation of the current MRL arrays is their limited radiolucent coverage in craniocaudal direction. The current PET window (field of view) is limited to 30-40 cm, which is mainly an issue for full-body acquisitions. Future work should attempt to increase the size of this window or investigate the attenuation of the regions with electronics to allow for the use of multiple arrays in craniocaudal direction.

As described in the introduction, the new 1.5 T PET/MRI is being developed for the MRIGRT planning stage, where it enables a single-scan treatment planning workflow. The CT scan, that is traditionally used to provide electron density information for dose planning, can be replaced by the MRI-based synthetic CT (Arabi et al., 2018; Spadea et al., 2021) that is already generated for AC of the PET/MRI reconstruction. The PET and MRI data can be combined to perform motion correction and delineate structures of interest, such as tumors, metastases, and organs at risk. Hence, all required information for MRIGRT can be obtained from a single PET/MRI scan, which eliminates the need for (imperfect) image registrations to align scans of different machines or modalities. In this context, the use of an MRIGRT array for PET/MRI would also have an additional benefit for the workflow of an MRIGRT treatment: the same receive hardware and setup can be used during the pre-treatment PET/MRI scan and the MRL treatment. As the systems also feature the same 1.5 T field strength, split-gradient coil design, and software platform, image quality between the two systems will be nearly identical, which simplifies MRI protocol development and improves image registration.

In this work, we showed that MRL receive arrays are suitable for use on a new 1.5 T PET/MRI system but for PET/MRI systems at other field strengths lessons can be learned from the MRL coil design as well. A similar design can be used to manufacture receive arrays for, e.g., 3 T. Electronics will need to be adapted to be suitable for 3 T but the same layout, PET window, and support structure can in principle be used. Consequently, PET photon attenuation is expected to be comparable at other field strengths.

Future work may also try to translate the radiolucent design of the MRL arrays to other sites. Especially sites with varying anatomies, such as the head and neck (Zijlema et al., 2019b), could benefit from the flexible properties to obtain an optimal imaging performance, while the PET performance is warranted.

5.5 Conclusion

The use of MR-linac receive arrays for PET/MRI at 1.5 T is feasible and significantly reduces PET reconstruction errors with respect to a conventional diagnostic array, as the radiolucent design attenuates fewer photons. The 32-channel MRL prototype combines a low attenuation with fast imaging capabilities and therefore performs best overall.

Acknowledgements

This work is part of the research program HTSM with project number 15354, which is financed by the Netherlands Organization for Scientific Research (NWO) and Philips Healthcare. The authors acknowledge Tesla Dynamic Coils for providing the prototype MRL array that is used in this work. Additionally, the authors would like to thank Bastiaan van Nierop for his help with the experiments and Arthur Braat for his input on the clinical perspective of this work. Finally, the authors wish to thank Judd Jones for his help with Siemens data processing and the use of E7 tools.

5.6 Appendix: Forward projection validation

The forward projection method, which is used to assess the coil-induced reconstruction changes in-vivo (section 5.2.2.2), was validated using experimental phantom data.

5.6.1 Methods

Two methods are compared:

- The experimental method, as described in Figure 5.3 and applied to the phantom data.
- The projection method, as shown in Figure 5.4, but now applied to the phantom data.

The first method uses the PET/CT data with coil and masks the array in the CT to obtain a CT without array. The original PET sinogram is then used for the reconstructions. The second method uses the PET/CT data without coil and adds the coil to the CT to obtain a CT with array. Here, the PET sinogram is simulated using the new CT with array. Both methods produce a coil-induced signal difference map Δ , where the first (experimental) method is used as the gold standard, as explained in section 5.2.2.1. These two difference maps Δ are compared to validate the projection method's performance. This comparison is performed for all three MRI arrays that are assessed in this article. The experimental phantom data from section 5.2.2.1 was used.

5.6.2 Results and discussion

A comparison of the projection and experimental methods is shown in Figure 5.9. The difference maps are very similar for all three arrays, which confirms the accuracy of the projection method for our purpose.

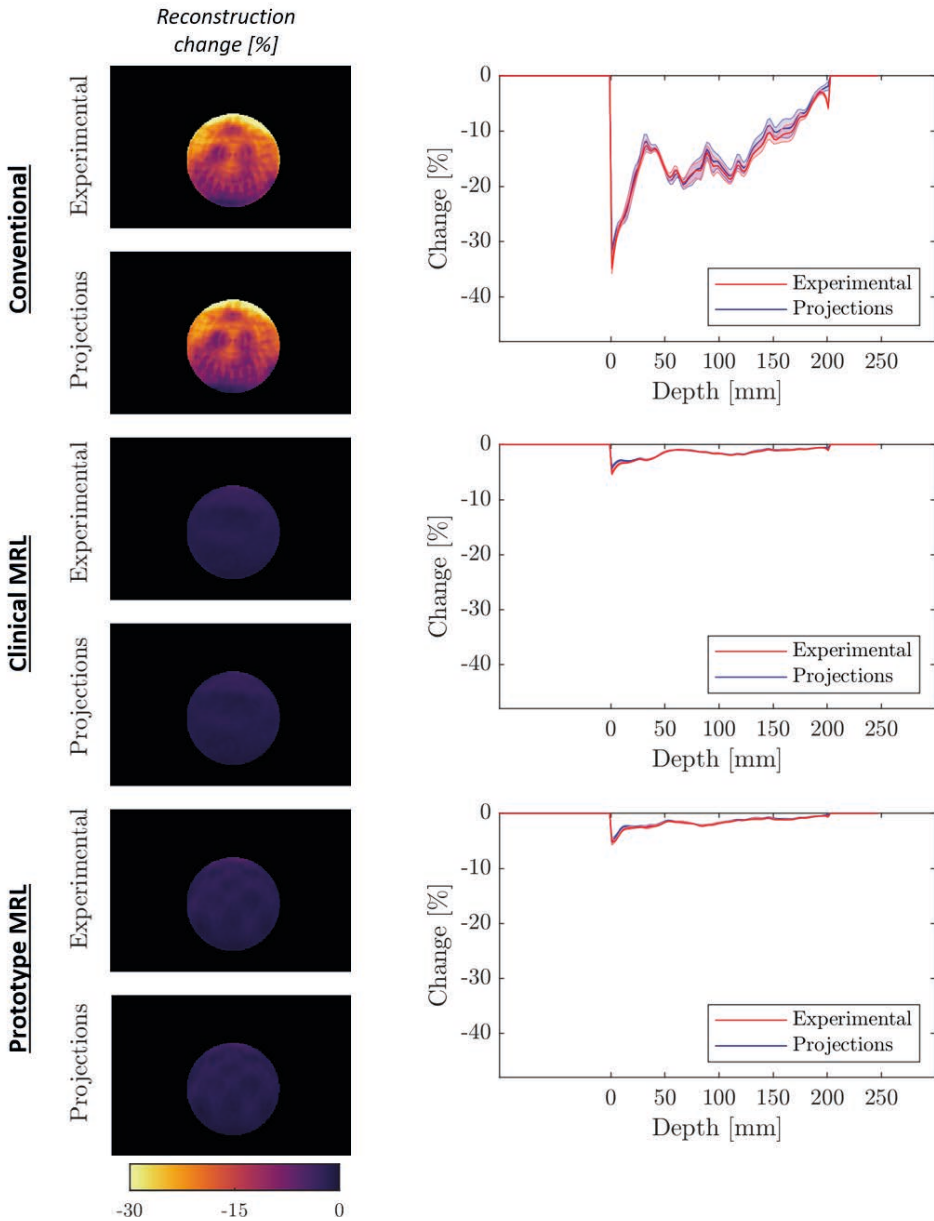


Figure 5.9 Comparison of the difference maps obtained with the projections and experimental methods. For all three arrays, the coil-induced reconstruction changes are shown (left). On the right, a profile is plotted to compare the two methods. The profiles represent the mean (line) and standard deviation (shading) of the 10 middle columns of the reconstruction change maps. Mean absolute differences between the two methods were 0.8% (conventional), 0.1% (clinical MRL), and 0.1% (prototype MRL) within the whole phantom.

CHAPTER 6

Summary and Discussion

MRI plays a major role in the current radiotherapy workflow and is becoming more important every year, especially now that hybrid MRI-radiotherapy machines are available for clinical use. These machines allow for daily MRI scans before, during, and after each treatment fraction.

6.1 Receive arrays for MRIGRT

The availability of MRI during radiotherapy treatments creates new possibilities but also poses new (technical) challenges. Conventional MRI receive arrays are not compatible with MRI-guided radiotherapy (MRIGRT), as their beam-attenuating electronics are distributed over their surface. Receive arrays for MRIGRT are therefore redesigned to have a radiation transparent, or radiolucent, window that has low attenuative properties (Hoogcarspel et al., 2018).

The current, clinical receive array of the 1.5 T MR-linac is designed for general-purpose body imaging. It allows for 3D imaging for position verification and fast 2D or slow 3D cine imaging. Faster imaging would be desirable, especially in regions with rapid (respiratory) motion, but is not possible due to the array's limited parallel imaging (acceleration) performance and SNR. These are caused by the array's limited number of receive channels, its placement centimeters away from the patient, and the required modifications of the coil loops to achieve radiolucency.

In this thesis, a novel design for radiolucent receive arrays was introduced to improve the imaging performance of the MR-linac without significantly affecting the delivered dose. Based on this design, two fully functional receive arrays were manufactured and evaluated: one for general-purpose body imaging and one for the head and neck (H&N) region.

6.1.1 Body array

In **Chapter 2**, the novel design was proposed and described. This design fulfilled several requirements: (1) a flexible design with low attenuative properties that can be disregarded in treatment planning, (2) a large number of receive channels (32), and (3) on-body placement.

A flexible and radiolucent design was achieved by switching from conventional, low impedance coils (LICs) to high impedance coils (HICs). Unlike LICs, HICs do not require beam-attenuating capacitors that LICs use to tune the loop to the desired frequency. Instead, the distributed capacitance of the coaxial conductor is used for tuning. Hence, a radiolucent design with multiple rows was possible. Additionally, HICs are flexible and exhibit limited coupling interactions with neighboring loops, even when they are deformed (Zhang et al., 2018). A HIC receive array therefore requires less-critical overlap optimization than LICs and consequently does not demand dense, highly-attenuating support materials to firmly secure the geometry.

Using these HICs, the number of channels was maximized to 32 by designing a 16-channel anterior and 16-channel posterior receive element. A double-row layout was proposed to maximize the number of channels while cabling could still be routed away without crossing the radiation window. HICs were crucial to achieving a radiolucent array with a high channel count, limited coupling interactions, and flexibility to follow the shape of the patient for optimal sensitivity.

The new array was placed directly onto the patient, again for optimal sensitivity, but on-body coil placement during MRigRT can lead to an increased surface dose (Ghila et al., 2016). In **Chapter 2**, it was shown that this effect could be counteracted with a layer of foam between the dense materials (i.e. plastic and copper) and the patient. This allowed the secondary electrons that are generated in the dense materials to curve away before they can deposit their dose into the patient.

Based on the design and preliminary tests, a fully functional 32-channel prototype was manufactured and tested in **Chapter 3**. Characterization of its radiolucency revealed only minor changes to the delivered dose of single beams ($\leq 1.5\%$). The clinical impact of this slight, highly localized attenuation was deemed negligible, as the use of multi-angle beam or volumetric arc treatments strongly reduces the impact of single beams on the final dose distribution. Additionally, physiological motion will blur underdosages within each beam.

Scanning with the prototype improved the SNR at the surface substantially, while the SNR at depth was similar to that of the clinical array. Irradiating while scanning did not impact the SNR, in contrast to reports in literature (Burke et al., 2010; Burke et al., 2012). G-factors were reduced considerably so that clinically used pre- and post-beam sequences could be accelerated up to 45% without a visible loss of image quality. Abdominal 3D cine imaging could be accelerated even further: the maximally

achievable temporal resolution was found to be 1.1 s, which was $>5\times$ faster than could be achieved with the clinical array. These speed increases were achieved using only a simple, clinically available parallel imaging technique (SENSE).

Clinical impact

The new 32-channel array, with its improved acquisition speed, has a large potential impact for clinical imaging on the MR-linac. First of all, shorter acquisition times of pre- and post-beam scans can reduce treatment times by several minutes, which could result in shorter treatment slots, improved patient comfort, and less patient movement. Alternatively, scan parameters can be optimized for a better target definition, e.g. using higher resolutions.

The five-fold speed gain for beam-on cine imaging may make it possible to switch from (multi-slice) 2D to 3D tracking sequences in certain anatomies using only simple parallel imaging techniques. Fast 3D tracking can enable 3D dose accumulation to monitor the delivered dose and possibly allow real-time adaptations of the treatment plan, i.e. real-time adaptive radiotherapy (Kontaxis et al., 2017a; Kontaxis et al., 2020). If the new array would enable the use of real-time adaptive radiotherapy for a specific application, treatment margins may be reduced, which could reduce the toxicity in organs at risk (OARs). Some applications may require even faster 3D cine imaging, e.g. 3D respiratory monitoring. For these applications, further optimizations of acquisitions and reconstructions will be required, which are discussed in section 6.3.1.

6.1.2 Head and neck array

MRI of the head and neck (H&N) region can be complicated by the radiotherapy-specific patient setup. The patient is immobilized by a radiotherapy mask, of which the shape hampers the use of conventional, close-fitting H&N MRI receive arrays. Currently, a dedicated H&N array for MRIgRT that is fully mask-compatible does not exist.

In **Chapter 4**, the findings from the previous chapters were used to design and manufacture a mask-compatible H&N array for the 1.5 T MR-linac and a 1.5 T MRI-simulation scanner. The design of this 8-channel H&N array consists of a single-channel baseplate on which the mask can be secured and a flexible 7-channel anterior element that follows the shape of the mask for an optimal SNR. For the latter, HICs were used again to achieve flexibility and radiolucency.

Dosimetry measurements of the array showed a mean coil-induced dose change of -0.3%. Small, local deviations directly under conductor wires and support structures were up to -2.7% for a single beam but had no clinically significant impact on a full treatment plan: gamma pass rates only slightly reduced from 97.9% to 97.6%, which was still well above the clinically required 95%.

The new H&N array improved the imaging performance with respect to two clinical setups. As a result of the H&N array's close fit of the anatomy, the SNR doubled (+123%) and tripled (+246%) with respect to the MRI-simulation and MR-linac setups, respectively. G-factors were also lower with the proposed H&N array, i.e. the acceleration performance improved as well. The improved imaging performance resulted in a clearly visible SNR improvement of clinically used TSE and DWI scans.

Clinical impact

The mask-compatible H&N array is a potential game-changer for MRI of patients in an immobilization mask. First of all, the image quality is improved with respect to the current clinical setups. SNR within the region of interest is greatly improved, as well as the acceleration performance. Together, these allow for a range of protocol optimizations, which can reduce scan times or improve image quality. As with the body array, shortened pre- and post-beam scans can reduce the fraction duration on the MR-linac. Additionally, the improved acceleration performance could be exploited to increase the tracking frequency of dynamic imaging sequences for treatment gating or tracking purposes, or extend the tracking sequences from 2D to 3D.

Alternatively, scan times could be kept equal to improve the quality of scans that are currently limited by the clinical receive setups. Especially SNR-demanding acquisitions, such as DWI or quantitative parameter mapping, could greatly benefit. For example, the increased SNR can reduce underestimations of ADC values (Kooreman et al., 2020) and may also improve the precision by allowing the use of higher b-values without reaching the noise floor. It may even be possible to switch to DWI-SPLICE sequences that have a higher geometrical accuracy but an intrinsically lower SNR (Schakel et al., 2017). Other quantitative MRI (qMRI) methods, such as parameter mapping, may use the higher SNR for longer TEs to better fit $T_2^{(*)}$ values before reaching the noise floor. Furthermore, the improved acceleration performance of the H&N array may reduce geometric distortions in EPI sequences. In other words, the H&N array can improve the accuracy and precision of qMRI methods to make them more clinically feasible and useful. The improved scans may be able to improve target definitions and thereby reduce the required treatment margins to minimize side effects without affecting the treatment's efficacy. Additionally, the improved DWI/qMRI acquisitions may be acquired (daily) on the MR-linac to predict early response to the treatment (Nejad-Davarani et al., 2020; Yan et al., 2021). In case of a poor efficacy, the treatment can then be adapted or terminated.

Finally, the H&N array's new design can also simplify setup procedures and reduce operator-dependent variations, especially with respect to the MRI-simulation setup. The mask is simply mounted onto the baseplate and the anterior element is placed on top. Moreover, imaging performance with the H&N array will be nearly identical on the MRI-simulation scanner and the MR-linac, which simplifies protocol development and subsequent (automated) image analyses.

6.2 Receive arrays for PET/MRI

The designs of the newly developed MRIGRT receive arrays in this thesis were adapted for optimal radiolucency. Interestingly, receive arrays for simultaneous PET/MRI have very similar requirements, as PET photons, originating from the patient's body, can be attenuated by an MRI receive array before reaching the PET detectors. This spatially varying photon attenuation can introduce distortions in the reconstructed image. Therefore, simultaneous PET/MRI requires attenuation correction (AC) of photon-attenuating objects, such as MRI receive arrays. However, AC of flexible, on-body arrays is complex and therefore often omitted, as the positions of the array's attenuating structures are variable and in general unknown. This can lead to significant, spatially varying, PET signal losses when conventional MRI receive arrays are used.

In **Chapter 5**, it was investigated if the use of radiolucent MRIGRT receive arrays reduces PET signal losses to a clinically insignificant level on a new 1.5 T PET/MRI system. However, PET's photon energy is lower (511 keV versus a 7 MV spectrum for MRIGRT), which could increase an array's PET photon attenuation fraction compared to MRIGRT. Two arrays of the 1.5 T MR-linac (MRL) were assessed: the 8-channel clinical array and the 32-channel prototype array from **Chapter 3**. A conventional 28-channel MRI receive array was used as a reference. The impact of these arrays on the PET sensitivity and image reconstructions was experimentally determined, simulated, and compared. Furthermore, the MRI performance of the three arrays was assessed.

PET acquisitions of a phantom revealed that significant, spatially-varying signal errors are induced by the conventional array. The MRL arrays were able to reduce the maximum signal errors from 32.7% (conventional) to 3.6% (clinical MRL) and 3.5% (prototype MRL). Simulations with data from eight cancer patients showed that average reconstruction errors in the primary tumor were reduced from 14.3% (conventional) to 1.2% (clinical MRL) and 1.0% (prototype MRL). This means that MRIGRT arrays of the MRL reduced PET signal losses $>10\times$, which decreases, or even eliminates, the need for coil AC.

MRI data showed that the SNR of the MRL arrays was slightly lower at depth compared to the conventional array (110 versus 135). The parallel imaging (acceleration) performance of the conventional and prototype MRL arrays was similar, while the clinical MRL array's acceleration performance was lower. Considering these performance metrics, the prototype MRL array performs approximately as well as the conventional array.

As a result, the prototype MRL array could replace the conventional array to significantly reduce PET reconstruction errors on the new 1.5 T PET/MRI system, while MRI performance is not compromised significantly compared to the conventional array. In case MRI performance is not critical, but PET performance is, the clinical MRL array could also be used. These arrays can easily be connected to the 1.5 T PET/MRI scanner that is currently being developed and installed. For PET/MRI systems at other field strengths, lessons can be learned from the MRIGRT coil design to manufacture similar

receive arrays. Internally, electronics will need to be adapted to the field strength but the same layout, PET window, and support structure can be used. Consequently, PET photon attenuation will be comparably low at other field strengths.

One limitation of the MRIgRT arrays is their limited radiolucent PET window in the craniocaudal direction. This is mainly an issue when full-body PET/MRI scans are desired. One could place multiple MRIgRT arrays craniocaudally but this would result in sections with very low attenuation (within an array's PET window) and sections with slightly higher attenuation (outside the PET windows). The impact of such an approach was not studied in this thesis and has limited clinical impact, as radiotherapy treatments rarely cover more than 30-40 cm craniocaudally. Nonetheless, this effect should be studied before use for larger treatment areas.

Clinical impact

MRIgRT arrays reduce signal losses by $>10\times$ and therefore significantly improve the precision of PET reconstructions on the new 1.5 T PET/MRI scanner. As noted before, this is beneficial for all acquisitions but especially for quantitative measurements. With the conventional array, these would suffer from significant errors of which the exact (spatial) impact is dependent on the placement of the array. The errors could lead to incorrect conclusions about a patient's treatment response or the delivered dose of a radioembolization treatment. By contrast, the MRIgRT arrays reduced these errors to only $\sim 1\%$ in the primary tumors of eight patients. These errors will be (much more) acceptable for all clinical applications.

On the MRI side, no significant impact is to be expected when the prototype MRL array is used, as its MRI performance is similar to that of the conventional array. Motion-compensated PET reconstructions that require fast dynamic (3D) imaging, e.g. in the abdomen or thorax, are therefore expected to be equally good. Conversely, the clinical MRL array does reduce the acceleration performance and is therefore less suitable for motion-compensated PET reconstructions.

The advantages of using MRIgRT arrays on the 1.5 T PET/MRI system are especially clear when PET/MRI is used for pre-treatment (simulation) imaging before an MRIgRT treatment on the MR-linac. In this case, the same receive arrays can be used during the PET/MRI scan and the MR-linac treatment. As the systems also feature the same 1.5 T field strength, split-gradient coil design, and software platform, image quality between the two systems will be nearly identical, which simplifies MRI protocol development and improves image registration.

6.3 Future perspectives

In **Chapters 3 and 4**, designs of radiolucent receive arrays have been presented and their feasibility has been demonstrated with fully functional prototypes. From here, translation towards clinical implementation should be pursued. The prototypes and concepts should be converted into robust, industrial-grade products that are ready for clinical use. But what are the necessary steps to make this possible and which future applications can be pursued?

6.3.1 Body array

In terms of radiolucency and imaging performance, the 32-channel body array is close to clinical readiness, as demonstrated in **Chapter 3**. However, interfacing of the array, i.e. connection to the system, is currently cumbersome and impractical for clinical use. The setup requires four interface boxes with ADC hardware on the table and each receive channel needs to be connected to a box separately, which is time-consuming. Ideally, a future version of the array would connect directly to the table with a single connector. Additionally, the posterior element could be incorporated into the table to reduce setup complexity.

In terms of imaging capabilities, the 32-channel body array has been designed to accelerate 3D imaging and allow for 3D tracking of the anatomy. Dynamic acquisition times of ~1 second were achieved with standard reconstruction techniques, which was >5× faster than the clinical array could achieve. However, another five-fold speed increase is needed to achieve the 5 Hz that is required for tracking of respiratory motion (Keall et al., 2006). This will likely be difficult to achieve by only further optimizing the receive array. Namely, placement of more channels, to achieve a higher acceleration performance, is complicated by the radiation window that does not allow more than two rows craniocaudally. Therefore, further improvements should be sought in advanced image reconstruction techniques, such as compressed sensing (CS), that allow for extreme undersampling and thus (ultra)short acquisition times (Lustig et al., 2007). Unfortunately, reconstruction times are often in the order of minutes or hours, which makes CS unusable for real-time tracking purposes. Recently, deep learning has been introduced as an alternative to quickly reconstruct (3D) images and motion fields with short acquisition *and* reconstruction times (Ilg et al., 2017; Schlemper et al., 2018; Terpstra et al., 2020b). The feasibility of applying this technique to the 32-channel data should be explored to achieve the desired 5 Hz. When speeds can be pushed even further than required for respiratory motion, application of the array for cardiac radio-ablation procedures can be considered, which would require an even higher temporal resolution.

6.3.2 H&N array

As discussed before, the H&N array will require finetuning before clinical readiness, i.e. the use of attenuating support materials should be reduced for optimal radiolucency.

For example, the multi-piece, overlapping support structure should be replaced by an ultrathin, single-piece mold. Attenuation by the exterior foam layers is already minimal and should continue to be that way.

Interfacing to the system is simple for this array, as it was designed to connect directly to the MR-linac. The design could even be upgraded to 12 channels and interfacing would still be equally simple. This way, it would be possible to create a larger field of view that also covers the brain and/or shoulders. Connection to the MRI-simulation system does require an analog-to-digital converter box (dStream, Philips) but this box was already available at our department.

As discussed before, several applications could benefit from the improved imaging performance compared to the current clinical array. Especially qMRI techniques, such as DWI, would benefit and could potentially be used for improved target definition and (early) treatment response monitoring. Once a clinical version of the H&N array is available, clinical studies should be started to investigate the value of (daily) qMRI for treatment response assessment.

Furthermore, the array's compatibility with PET/MRI should be investigated. Its radiolucency for 511 keV photons should be assessed, as described in **Chapter 5** of this thesis, after which it may be used for a full MRIgRT workflow on the 1.5 T PET/MRI system and MR-linac.

6.3.3 Towards product development and clinical implementation

Now that all necessary steps for further development are described, valorization of these results can occur. The experimental phase has been performed in this thesis: from simple builds to fully functional prototypes. However, these prototypes must ultimately be translated into industrial-grade products, preferably by a vendor. Only then can clinical implementation be realized and can the new arrays prove their worth in patients and other institutes.

The tangible result of this thesis is that a vendor has started collaborating with us to translate our research into a first version of a product, i.e. the H&N array. Moreover, this vendor has expressed its intention to further develop the body array and H&N array into clinical products. Hence, this thesis is a great example of what can be accomplished by collaborations between academia and industry.

6.4 The ultimate MRIgRT workflow(s)

If one would have to define the ultimate MRIgRT workflow, one would probably describe an outpatient treatment on a single day and using a single machine. A patient would enter with a cancer diagnosis and would be placed into the MR-linac. Pre-treatment imaging is acquired, regions of interest are (automatically) contoured, an MRI-based

synthetic CT is generated, and a treatment plan is (automatically) calculated. The treatment consists of a single fraction with very small error margins, as real-time treatment adaptations are facilitated by fast 3D anatomy tracking in the beam-on phase. After delivery, the patient is taken out of the MR-linac, which completes the radiotherapy treatment. Such a treatment would greatly improve efficiency and reduce the patient burden. This complete workflow is currently not possible (yet) but steps have been taken to reduce the number of fractions (hypofractionation), reduce margins, perform real-time motion quantification, and perform real-time plan adaptation (Finazzi et al., 2020; Keall et al., 2019; Kontaxis et al., 2017b; Winkel et al., 2021).

A modality that is not included in this MR-linac-only workflow is PET, which could provide enhanced visualization of metabolic activity, e.g. of small lesions or lymph nodes. A different MRIgRT workflow that includes PET would start with one pre-treatment (simulation) PET/MRI scan, after which the MR-linac is used for treatment delivery based on these images. This would make for a simple radiotherapy workflow with fewer (cross-modality) registration steps and accompanying registration errors. This workflow is becoming especially realistic once the development and installation of the new 1.5 T PET/MRI scanner have been completed.

There are multiple ways in which this thesis contributes towards realizing these ultimate workflows. First of all, the new MRIgRT arrays from **Chapters 3 and 4** allow for more precise and faster imaging of the anatomy of interest. Consequently, target definition can be improved or acquisition times reduced. **Chapter 3** showed a five-fold reduction of the dynamic acquisition times of 3D volumes on the MR-linac, which is a major step towards the ability to track (and adapt the treatment for) respiratory motion in real-time. Additionally, **Chapter 5** demonstrated the feasibility of using the same receive hardware on the MR-linac and PET/MRI systems. This will ensure a consistent image quality between both systems, which will simplify and improve the spatial registration of scans.

All aforementioned steps will reduce uncertainties and are therefore expected to allow for reduced tumor margins. Consequently, the dose to the OARs will be lower, as well as the related toxicity, which opens the door to hypofractionation.

6.5 Concluding remarks

Receive arrays for MRIgRT are currently not fully optimized to have the best MRI performance but are rather a compromise between image quality and radiolucency. This thesis showed that no concessions are needed on either end when a suitable design is chosen. HICs were crucial to achieving these radiolucent arrays with a high channel count, limited coupling interactions, and structural flexibility. Furthermore, these radiolucent MRIgRT arrays can be used in PET/MRI scanners to reduce PET reconstruction errors. Current developments aim to combine the PET/MRI and MR-linac machines into a simple radiotherapy workflow with fewer (cross-modality) registration steps and accompanying registration errors. This thesis has confirmed the synergy

between the two systems and has shown that the MRI receive hardware could be interchangeable, which makes the development of receive hardware for both machines more attractive. Conventional MRI already makes use of its diverse supply of dedicated receive arrays and the fields of MRIGRT and PET/MRI would benefit if the same could be achieved.

CHAPTER 7

Samenvatting

Tijdens een radiotherapiebehandeling wordt ioniserende straling gebruikt om kankercellen te doden, waarbij het doel is om zoveel mogelijk dosis in een tumor te krijgen, terwijl de dosis in gezonde weefsels minimaal blijft. Bij de behandeling wordt gebruik gemaakt van het feit dat gezond weefsel zich beter en sneller herstelt dan tumorweefsel. Om maximaal gebruik te maken van dit gegeven worden behandelingen opgedeeld in behandelfracties om het gezonde weefsel tussendoor te laten herstellen. Voor iedere patiënt wordt een individueel bestralingsplan gemaakt en geoptimaliseerd. Hiervoor is het van belang om een goed beeld te hebben van de locaties en vormen van de tumor en de omliggende organen. Om dit te bereiken, wordt gebruik gemaakt van verscheidene beeldvormende technieken, zoals CT, MRI en PET. MRI krijgt hierbij een steeds prominentere rol vanwege diens flexibiliteit en goede contrast van weke delen.

Recentelijk zijn er zelfs hybride systemen ontwikkeld die het mogelijk maken om MRI-beelden op te nemen *tijdens* de bestraling, bijvoorbeeld de 1.5 T MR-linac. Deze machines kunnen tegelijkertijd bestralen en MRI-scans acquireren, waardoor de tumorlocatie tijdens de behandeling kan worden bepaald. Met deze informatie wordt het mogelijk om de behandeling te pauzeren (gating) of sturen (tracking) als er (on)verwachte bewegingen plaatsvinden. Daardoor kan er nauwkeuriger bestraald worden en kunnen veiligheidsmarges om tumoren verkleind worden, waardoor er minder dosis in gezonde weefsels belandt en de kans op bijwerkingen wordt verkleind. Deze toepassing wordt MRI-gestuurde radiotherapie (MRIgRT) genoemd.

MRI gebruikt ontvangspoelen om het signaal mee op te vangen. Spoelen voor MRIgRT vereisen echter wel aanpassingen, omdat de elektronica en constructie van conventionele spoelen veel straling tegenhouden (attenueren). De huidige klinische ontvangspoel van de MR-linac heeft daarom een radiolucent stralingsvenster: een deel van de spoel dat weinig straling tegenhoudt. Hierbinnen bevindt zich vrijwel geen elektronica, waardoor er zonder problemen doorheen gestraald kan worden. Deze spoel heeft echter suboptimale beeldvormingsprestaties vanwege zijn ontwerp dat weinig ontvangtkanalen bevat, waardoor weinig scantijdverkortening mogelijk is, en op centimeters afstand van de patiënt geplaatst wordt, wat de sensitiviteit verlaagt. Een

spoel die het mogelijk maakt om sneller te scannen, zou daardoor betere tumorlokalisatie mogelijk kunnen maken voor de eerdergenoemde toepassingen.

Dit proefschrift beschrijft daarom de ontwikkeling van verbeterde radiolucente ontvangspoelen voor MRIgRT. Daarnaast wordt ook de toepassing van deze spoelen voor PET/MRI onderzocht, welke ook kan profiteren van een lagere fotonattenuatie.

In **Hoofdstuk 2** wordt een nieuw ontwerp voor een MR-linac ontvangspoel getoond en getest. Deze voldoet aan alle eisen: (1) plaatsing direct op het lichaam voor optimale sensitiviteit, (2) een flexibel design dat weinig straling tegenhoudt en niet meegenomen hoeft te worden in het behandelplan, (3) een groot aantal ontvangstkanalen (32).

Een nadeel van plaatsing direct op het lichaam is dat dit de huiddosis kan verhogen doordat de secundaire elektronen, die worden gegenereerd in de spoel, hun dosis afgeven in de huid. In dit hoofdstuk is aangetoond dat een verhoogde huiddosis kan worden voorkomen door een laag schuim te plaatsen tussen de zwaardere materialen (plastic en koper) en de patiënt. Hierdoor kunnen de elektronen worden afgebogen door het magnetisch veld voordat deze de patiënt bereiken.

Het ontwerp van de ontvangspoel is flexibel en radiolucent gemaakt door hoog-impedante spoelen (HIC's) te gebruiken in plaats van de reguliere laag-impedante spoelen (LIC's). HIC's maken gebruik van dunne coaxiale geleiders en zijn zeer flexibel zonder hun prestatievermogen te verliezen. Ook hebben ze weinig last van elektromagnetische koppelingseffecten met aangrenzende kanalen. Daardoor is het maken van een array eenvoudiger en hebben HIC's een minder stevige, en dus minder stralingsverzwakkende, constructie nodig. Bovendien hebben HIC's geen stralingsverzwakkende condensatoren nodig die LIC's gebruiken om de spoel af te stemmen op de gewenste frequentie. Met behulp van HIC's is het aantal kanalen gemaximaliseerd tot 32 door een 16-kanaals anterior en 16-kanaals posterior ontvangstelement te ontwerpen. De lay-out van beide elementen bestaat uit twee rijen om het aantal kanalen te maximaliseren zonder bekabeling door het stralingsvenster te leiden.

Op basis van dit ontwerp en de eerste tests is een volledig functioneel 32-kanaals prototype vervaardigd en getest in **Hoofdstuk 3**. Karakterisering van de radiolucentie laat slechts kleine veranderingen zien in de afgegeven dosis van een enkele bundel ($\leq 1.5\%$). De klinische impact van deze kleine, lokale dosisreductie wordt verwaarloosbaar geacht, omdat behandelplannen met bundels vanuit meerdere hoeken de impact van een enkele bundel op de uiteindelijke dosisverdeling verminderen. De MRI-prestaties verbeteren aanzienlijk, zowel qua SNR alsook qua snelheid. Klinisch gebruikte sequenties kunnen tot wel 45% worden versneld en de maximaal haalbare temporele resolutie van abdominale 3D-cine-MRI is verbeterd tot 1.1 s, wat $>5\times$ sneller is dan met de klinische spoel behaald kon worden.

De ontvangspoelen die tot hier besproken zijn, zijn ontworpen voor scans van de thorax, abdomen en pelvis. MRI wordt ook vaak gebruikt voor beeldvorming

van het hoofd-halsgebied (HH-gebied). Echter, deze wordt bemoeilijkt door het radiotherapiemasker waarmee patiënten worden geïmmobiliseerd om beweging tijdens en tussen behandelfracaties te voorkomen. De vorm van deze maskers belemmert het gebruik van conventionele, nauwsluitende HH-ontvangstspoelen. Daarnaast bestaat er geen speciale HH-spoel voor MRIgRT dat volledig compatibel is met maskers. In **Hoofdstuk 4** worden de bevindingen uit de voorgaande hoofdstukken daarom gebruikt om een masker-compatibele HH-spoel te ontwerpen voor de 1.5 T MR-linac en een 1.5 T MRI-simulatiescanner.

Het ontwerp van deze 8-kanaals HH-spoel bestaat uit een enkelkanaals “baseplate”, waarop het masker direct kan worden bevestigd, en een flexibel 7-kanaals anterior ontvangstelement dat de vorm van het masker volgt. Voor de laatstgenoemde zijn opnieuw HIC's gebruikt om flexibiliteit en radiolucentie te realiseren. Een volledig functioneel prototype is vervaardigd en gekarakteriseerd.

Dosimetriemetingen laten kleine dosisveranderingen zien. Kleine, lokale afwijkingen zijn tot -2.7% voor een enkele bundel, maar hebben geen klinisch significante impact op een volledig behandelplan. De voorgestelde HH-spoel verbetert de beeldvormingsprestaties met betrekking tot de twee klinische opstellingen. De SNR verdubbelt (+123%) en verdrievoudigt (+246%) vergeleken met, respectievelijk, de MRI-simulatie en MR-linac-opstellingen. G-factoren zijn ook lager met de voorgestelde HH-spoel, dat wil zeggen de acceleratieprestaties verbeteren met minder degradatie van de beeldkwaliteit. De verbeterde prestaties resulteren in een duidelijk zichtbare SNR-verbetering van klinisch gebruikte anatomische en diffusie-gewogen scans.

Zoals in de eerste hoofdstukken beschreven is, zijn de nieuwe MRIgRT ontvangspoelen uit dit proefschrift aangepast voor optimale radiolucentie. Interessant is dat PET/MRI zeer vergelijkbare vereisten voor ontvangspoelen heeft als MRIgRT. PET-fotonen, afkomstig uit het lichaam van de patiënt, kunnen worden verzwakt door een MRI-ontvangstspoel voordat ze de PET-detectoren bereiken. Dit kan zorgen voor fouten in het gereconstrueerde beeld. Attenuatiecorrectie (AC) kan worden gebruikt om te corrigeren voor verzwakkende structuren, maar wordt amper gedaan voor flexibele ontvangspoelen die op het lichaam liggen, omdat de posities van de verzwakkende structuren variabel en meestal onbekend zijn.

In **Hoofdstuk 5** is daarom onderzocht of MRIgRT ontvangspoelen ook geschikt zijn voor PET/MRI. Er zijn twee ontvangspoelen van de MR-linac (MRL) beoordeeld: de 8-kanaals klinische spoel en de 32-kanaals prototype-spoel uit **Hoofdstuk 3**. Een conventionele 28-kanaals MRI-ontvangstspoel is als referentie gebruikt. Analyses van fantoom- en patiëntdata lieten zien dat PET-signaalfouten $>10\times$ lager zijn wanneer een MRIgRT ontvangspoel werd gebruikt.

Uit MRI-scans blijkt vervolgens dat de prestaties van de prototype MRL-spoel en conventionele spoel vergelijkbaar zijn, terwijl de klinische MRL-spoel iets minder presteert. Het is dus mogelijk om de conventionele spoel te vervangen door de

prototype MRL-spoel om PET-reconstructiefouten aanzienlijk te verminderen, terwijl de MRI-prestaties ongeveer gelijk blijven.

Conclusies

In dit proefschrift zijn meerdere radiolucente ontvangspoelen beschreven die gebruikt kunnen worden voor MRI-gestuurde radiotherapie en PET/MRI. Deze spoelen verbeteren de beeldkwaliteit en acquisitiesnelheid ten opzichte van de klinische opstellingen, terwijl ze amper straling tegenhouden. De betere prestaties kunnen worden gebruikt om behandel tijden te verkorten of om tijdens de behandeling (real-time) planaanpassingen mogelijk te maken op basis van de MRI-beelden. De ontvangspoelen zouden daarom zo snel mogelijk klaargemaakt moeten worden voor gebruik in de kliniek. Hiervoor zouden de ontwerpen geprofessionaliseerd en uitvoeriger getest moeten worden, bijvoorbeeld om de betrouwbaarheid en veiligheid bij langdurig gebruik te kunnen garanderen.

Bibliography

- Arabi, H., Dowling, J. A., Burgos, N., Han, X., Greer, P. B., Koutsouvelis, N., & Zaidi, H. (2018). Comparative study of algorithms for synthetic CT generation from MRI: Consequences for MRI-guided radiation planning in the pelvic region. *Medical Physics*, *45*(11), 5218–5233. <https://doi.org/10.1002/mp.13187>
- Bastiaannet, R., Kappadath, S. C., Kunnen, B., Braat, A. J. A. T., Lam, M. G. E. H., & de Jong, H. W. A. M. (2018). The physics of radioembolization. *EJNMMI physics*, *5*(1), 22. <https://doi.org/10.1186/s40658-018-0221-z>
- Boeke, S., Mönnich, D., van Timmeren, J. E., & Balermipas, P. (2021). MR-guided radiotherapy for head and neck cancer: Current developments, perspectives, and challenges. *Frontiers in Oncology*, *11*. <https://doi.org/10.3389/fonc.2021.616156>
- Borman, P. T. S., Raaymakers, B. W., & Glitzner, M. (2019). ReconSocket: A low-latency raw data streaming interface for real-time MRI-guided radiotherapy. *Physics in Medicine & Biology*, *64*(18), 185008. <https://doi.org/10.1088/1361-6560/ab3e99>
- Borman, P. T. S., Tijssen, R. H. N., Bos, C., Moonen, C. T. W., Raaymakers, B. W., & Glitzner, M. (2018). Characterization of imaging latency for real-time MRI-guided radiotherapy. *Physics in Medicine & Biology*, *63*(15), 155023. <https://doi.org/10.1088/1361-6560/aad2b7>
- Braat, A. J. A. T., Prince, J. F., van Rooij, R., Bruijnen, R. C. G., van den Bosch, M. A. A. J., & Lam, M. G. E. H. (2018). Safety analysis of holmium-166 microsphere scout dose imaging during radioembolisation work-up: A cohort study. *European Radiology*, *28*(3), 920–928. <https://doi.org/10.1007/s00330-017-4998-2>
- Branderhorst, W., Steensma, B. R., Beijst, C., Huijting, E. R., Alborahal, C., Versteeg, E., Weissler, B., Schug, D., Gebhardt, P., Gross-Weege, N., Mueller, F., Krueger, K., Dey, T., Radermacher, H., Lips, O., Lagendijk, J., Schulz, V., Jong, H. W. A. M. d., & Klomp, D. W. J. (2020). Evaluation of the radiofrequency performance of a wide-bore 1.5 T positron emission tomography/magnetic resonance imaging body coil for radiotherapy planning. *Physics and Imaging in Radiation Oncology*, *17*, 13–19. <https://doi.org/10.1016/j.phro.2020.12.002>
- Breuer, F. A., Blaimer, M., Heidemann, R. M., Mueller, M. F., Griswold, M. A., & Jakob, P. M. (2005). Controlled aliasing in parallel imaging results in higher acceleration (CAIPIRINHA) for multi-slice imaging. *Magnetic Resonance in Medicine*, *53*(3), 684–691. <https://doi.org/10.1002/mrm.20401>
- Burke, B., Fallone, B. G., & Rathee, S. (2010). Radiation induced currents in MRI RF coils: Application to linac/MRI integration. *Physics in Medicine & Biology*, *55*(3), 735. <https://doi.org/10.1088/0031-9155/55/3/013>

-
- Burke, B., Wachowicz, K., Fallone, B. G., & Rathee, S. (2012). Effect of radiation induced current on the quality of MR images in an integrated linac-MR system. *Medical Physics*, 39(10), 6139–6147. <https://doi.org/10.1118/1.4752422>
- CBS. (2020). *Overzicht belangrijkste doodsoorzaken in 2019*. Retrieved March 5, 2021, from https://opendata.cbs.nl/statline/#/CBS/nl/dataset/7052_95/table?ts=1614947426392
- Chen, A. M., Cao, M., Hsu, S., Lamb, J., Mikaeilian, A., Yang, Y., Agazaryan, N., Low, D. A., & Steinberg, M. L. (2017). Magnetic resonance imaging guided reirradiation of recurrent and second primary head and neck cancer. *Advances in Radiation Oncology*, 2(2), 167–175. <https://doi.org/10.1016/j.adro.2017.02.002>
- Cherry, S. R., Sorenson, J. A., & Phelps, M. E. (2012). *Physics in nuclear medicine* (4th ed.). Elsevier Health Sciences.
- Chung, N.-N., Ting, L.-L., Hsu, W.-C., Lui, L. T., & Wang, P.-M. (2004). Impact of magnetic resonance imaging versus CT on nasopharyngeal carcinoma: Primary tumor target delineation for radiotherapy. *Head & Neck*, 26(3), 241–246. <https://doi.org/10.1002/hed.10378>
- Corea, J. R., Flynn, A. M., Lechêne, B., Scott, G., Reed, G. D., Shin, P. J., Lustig, M., & Arias, A. C. (2016). Screen-printed flexible MRI receive coils. *Nature Communications*, 7(1), 10839. <https://doi.org/10.1038/ncomms10839>
- Dale, B. M., Brown, M. A., & Semelka, R. C. (2015). *MRI: Basic principles and applications* (5th ed.). John Wiley & Sons, Ltd.
- Delaney, G., Jacob, S., Featherstone, C., & Barton, M. (2005). The role of radiotherapy in cancer treatment. *Cancer*, 104(6), 1129–1137. <https://doi.org/10.1002/cncr.21324>
- Deller, T. W., Mathew, N. K., Hurley, S. A., Bobb, C. M., & McMillan, A. B. (2021). PET image quality improvement for simultaneous PET/MRI with a lightweight MRI surface coil [Publisher: Radiological Society of North America]. *Radiology*, 298(1), 166–172. <https://doi.org/10.1148/radiol.2020200967>
- de Muinck Keizer, D. M., Kerkmeijer, L. G. W., Maspero, M., Andreychenko, A., van der Voort van Zyp, J. R. N., van den Berg, C. A. T., Raaymakers, B. W., Lagendijk, J. J. W., & de Boer, J. C. J. (2019). Soft-tissue prostate intrafraction motion tracking in 3D cine-MR for MR-guided radiotherapy. *Physics in Medicine & Biology*, 64(23), 235008. <https://doi.org/10.1088/1361-6560/ab5539>
- de Vries, J. H. W., Seravalli, E., Houweling, A. C., Woodings, S. J., van Rooij, R., Wolthaus, J. W. H., Lagendijk, J. J. W., & Raaymakers, B. W. (2018). Characterization of a prototype MR-compatible Delta4 QA system in a 1.5 Tesla MR-linac. *Physics in Medicine & Biology*, 63(2), 02NT02. <https://doi.org/10.1088/1361-6560/aa9d26>
- Dregely, I., Lanz, T., Metz, S., Mueller, M. F., Kuschan, M., Nimbalkar, M., Bundschuh, R. A., Ziegler, S. I., Haase, A., Nekolla, S. G., & Schwaiger, M. (2015). A 16-channel MR coil for simultaneous PET/MR imaging in breast cancer. *European Radiology*, 25(4), 1154–1161. <https://doi.org/10.1007/s00330-014-3445-x>
- Ekberg, L., Holmberg, O., Wittgren, L., Bjelkengren, G., & Landberg, T. (1998). What margins should be added to the clinical target volume in radiotherapy treatment

- planning for lung cancer? *Radiotherapy and Oncology*, 48(1), 71–77. [https://doi.org/10.1016/S0167-8140\(98\)00046-2](https://doi.org/10.1016/S0167-8140(98)00046-2)
- Eldib, M., Bini, J., Robson, P. M., Calcagno, C., Faul, D. D., Tsoumpas, C., & Fayad, Z. A. (2015). Markerless attenuation correction for carotid MRI surface receiver coils in combined PET/MR imaging. *Physics in Medicine and Biology*, 60(12), 4705–4717. <https://doi.org/10.1088/0031-9155/60/12/4705>
- Elekta. (2018, August 24). *Australia's largest provider of #radiotherapy treatment, GenesisCare, orders Elekta Unity MR-linac to increase access to cutting edge #cancer treatment* [#ElektaANZ #MRLinac #cancercare](https://t.co/ajRZwu9aml) [@elekta]. Retrieved March 5, 2021, from <https://twitter.com/elekta/status/1032752069839663104>
- Fallone, B. G. (2014). The rotating biplanar linac–magnetic resonance imaging system. *Seminars in Radiation Oncology*, 24(3), 200–202. <https://doi.org/10.1016/j.semradonc.2014.02.011>
- Farag, A., Thompson, R. T., Thiessen, J. D., Butler, J., Prato, F. S., & Théberge, J. (2019). Assessment of a novel 32-channel phased array for cardiovascular hybrid PET/MRI imaging: MRI performance. *European Journal of Hybrid Imaging*, 3(1), 13. <https://doi.org/10.1186/s41824-019-0061-7>
- Ferreira, E. d. S., & Souza, J. S. (2017). Gamma radiation in ceramic capacitors: A study for space missions. *Journal of Physics: Conference Series*, 911, 012004. <https://doi.org/10.1088/1742-6596/911/1/012004>
- Finazzi, T., van Sörnsen de Koste, J. R., Palacios, M. A., Spoelstra, F. O. B., Slotman, B. J., Haasbeek, C. J. A., & Senan, S. (2020). Delivery of magnetic resonance-guided single-fraction stereotactic lung radiotherapy. *Physics and Imaging in Radiation Oncology*, 14, 17–23. <https://doi.org/10.1016/j.phro.2020.05.002>
- Freitag, M. T., Radtke, J. P., Hadaschik, B. A., Kopp-Schneider, A., Eder, M., Kopka, K., Haberkorn, U., Roethke, M., Schlemmer, H.-P., & Afshar-Oromieh, A. (2016). Comparison of hybrid 68ga-PSMA PET/MRI and 68ga-PSMA PET/CT in the evaluation of lymph node and bone metastases of prostate cancer. *European Journal of Nuclear Medicine and Molecular Imaging*, 43(1), 70–83. <https://doi.org/10.1007/s00259-015-3206-3>
- Frohwein, L. J., s, M. H., Schlicher, D., Bolwin, K., Büther, F., Jiang, X., & Schäfers, K. P. (2018). PET attenuation correction for flexible MRI surface coils in hybrid PET/MRI using a 3D depth camera. *Physics in Medicine & Biology*, 63(2), 025033. <https://doi.org/10.1088/1361-6560/aa9e2f>
- Fürst, S., Souvatzoglou, M., Martinez-Möller, A., Schwaiger, M., Nekolla, S. G., & Ziegler, S. I. (2014). Impact of flexible body surface coil and patient table on PET quantification and image quality in integrated PET/MR. *Nuklearmedizin. Nuclear Medicine*, 53(3), 79–87. <https://doi.org/10.3413/Nukmed-0608-13-07>
- Ghila, A., Fallone, B. G., & Rathee, S. (2016). Influence of standard RF coil materials on surface and buildup dose from a 6 MV photon beam in magnetic field. *Medical Physics*, 43(11), 5808–5816. <https://doi.org/10.1118/1.4963803>
- Glitzner, M., Denis de Senneville, B., Legendijk, J. J. W., Raaymakers, B. W., & Crijs, S. P. M. (2015). On-line 3D motion estimation using low resolution MRI. *Physics*

-
- in *Medicine and Biology*, 60(16), N301–N310. <https://doi.org/10.1088/0031-9155/60/16/N301>
- Glitzner, M., Woodhead, P. L., Borman, P. T. S., Lagendijk, J. J. W., & Raaymakers, B. W. (2019). Technical note: MLC-tracking performance on the Elekta unity MRI-linac. *Physics in Medicine & Biology*, 64(15), 15NT02. <https://doi.org/10.1088/1361-6560/ab2667>
- Grein, E. E., Lee, R., & Luchka, K. (2002). An investigation of a new amorphous silicon electronic portal imaging device for transit dosimetry. *Medical Physics*, 29(10), 2262–2268. <https://doi.org/10.1118/1.1508108>
- Griswold, M. A., Jakob, P. M., Heidemann, R. M., Nittka, M., Jellus, V., Wang, J., Kiefer, B., & Haase, A. (2002). Generalized autocalibrating partially parallel acquisitions (GRAPPA). *Magnetic Resonance in Medicine*, 47(6), 1202–1210. <https://doi.org/10.1002/mrm.10171>
- Haacke, E. M., Brown, R. W., Thompson, M. R., & Venkatesan, R. (1999, June 10). *Magnetic resonance imaging: Physical principles and sequence design*. Wiley.
- Hamman, D. J. H. (1971). *Radiation effects design handbook. section 3 - electrical insulating materials and capacitors*. Retrieved July 17, 2019, from <https://ntrs.nasa.gov/search.jsp?R=19710020300>
- Henke, L. E., Contreras, J. A., Green, O. L., Cai, B., Kim, H., Roach, M. C., Olsen, J. R., Fischer-Valuck, B., Mullen, D. F., Kashani, R., Thomas, M. A., Huang, J., Zoberi, I., Yang, D., Rodriguez, V., Bradley, J. D., Robinson, C. G., Parikh, P., Mutic, S., & Michalski, J. (2018). Magnetic resonance image-guided radiotherapy (MRIgRT): A 4.5-year clinical experience. *Clinical Oncology*, 30(11), 720–727. <https://doi.org/10.1016/j.clon.2018.08.010>
- Hoogcarspel, S. J., Crijns, S. P. M., Lagendijk, J. J. W., van Vulpen, M., & Raaymakers, B. W. (2013). The feasibility of using a conventional flexible RF coil for an online MR-guided radiotherapy treatment. *Physics in Medicine and Biology*, 58(6), 1925–1932. <https://doi.org/10.1088/0031-9155/58/6/1925>
- Hoogcarspel, S. J., Zijlema, S. E., Tijssen, R. H. N., Kerkmeijer, L. G. W., Jürgenliemk-Schulz, I. M., Lagendijk, J. J. W., & Raaymakers, B. W. (2018). Characterization of the first RF coil dedicated to 1.5 T MR guided radiotherapy. *Physics in Medicine & Biology*, 63(2), 025014. <https://doi.org/10.1088/1361-6560/aaa303>
- Hoskin, P. (2012). *External beam therapy*. OUP Oxford.
- ICRU 50. (1993). *Prescribing, recording and reporting photon beam therapy*. International Commission on Radiation Units & Measures. Bethesda, Maryland, USA.
- ICRU 62. (1999). *Prescribing, recording and reporting photon beam therapy (supplement to ICRU report 50)*. International Commission on Radiation Units & Measures. Bethesda, Maryland, USA.
- Ilg, E., Mayer, N., Saikia, T., Keuper, M., Dosovitskiy, A., & Brox, T. (2017). FlowNet 2.0: Evolution of optical flow estimation with deep networks. *Proceedings of the IEEE Conference on Computer Vision and Pattern Recognition (CVPR)*.
- Kartmann, R., Paulus, D. H., Braun, H., Aklan, B., Ziegler, S., Navalpakkam, B. K., Lentschig, M., & Quick, H. H. (2013). Integrated PET/MR imaging: Automatic

- attenuation correction of flexible RF coils. *Medical Physics*, 40(8), 082301. <https://doi.org/10.1118/1.4812685>
- Kawrakow, I., & W.O. Rogers, D. (2000, January 1). *The EGSnrc code system: Monte carlo simulation of electron and photon transport*. National Research Council Canada. Ottawa, Canada.
- Keall, P., Poulsen, P., & Booth, J. T. (2019). See, think, and act: Real-time adaptive radiotherapy. *Seminars in Radiation Oncology*, 29(3), 228–235. <https://doi.org/10.1016/j.semradonc.2019.02.005>
- Keall, P. J., Barton, M., & Crozier, S. (2014). The Australian magnetic resonance imaging–linac program. *Seminars in Radiation Oncology*, 24(3), 203–206. <https://doi.org/10.1016/j.semradonc.2014.02.015>
- Keall, P. J., Mageras, G. S., Balter, J. M., Emery, R. S., Forster, K. M., Jiang, S. B., Kapatoes, J. M., Low, D. A., Murphy, M. J., Murray, B. R., Ramsey, C. R., Van Herk, M. B., Vedam, S. S., Wong, J. W., & Yorke, E. (2006). The management of respiratory motion in radiation oncology report of AAPM task group 76. *Medical Physics*, 33(10), 3874–3900. <https://doi.org/10.1118/1.2349696>
- Kellman, P., & McVeigh, E. R. (2005). Image reconstruction in SNR units: A general method for SNR measurement. *Magnetic Resonance in Medicine*, 54(6), 1439–1447. <https://doi.org/10.1002/mrm.20713>
- Klüter, S. (2019). Technical design and concept of a 0.35 T MR-linac. *Clinical and Translational Radiation Oncology*, 18, 98–101. <https://doi.org/10.1016/j.ctro.2019.04.007>
- Kontaxis, C., Bol, G. H., Stemkens, B., Glitzner, M., Prins, F. M., Kerkmeijer, L. G. W., Lagendijk, J. J. W., & Raaymakers, B. W. (2017a). Towards fast online intrafraction replanning for free-breathing stereotactic body radiation therapy with the MR-linac. *Physics in Medicine & Biology*, 62(18), 7233–7248. <https://doi.org/10.1088/1361-6560/aa82ae>
- Kontaxis, C., Bol, G. H., Kerkmeijer, L. G. W., Lagendijk, J. J. W., & Raaymakers, B. W. (2017b). Fast online replanning for interfraction rotation correction in prostate radiotherapy. *Medical Physics*, 44(10), 5034–5042. <https://doi.org/10.1002/mp.12467>
- Kontaxis, C., de Muinck Keizer, D. M., Kerkmeijer, L. G. W., Willigenburg, T., den Hartogh, M. D., van der Voort van Zyp, J. R. N., de Groot-van Breugel, E. N., Hes, J., Raaymakers, B. W., Lagendijk, J. J. W., & de Boer, H. C. J. (2020). Delivered dose quantification in prostate radiotherapy using online 3D cine imaging and treatment log files on a combined 1.5T magnetic resonance imaging and linear accelerator system. *Physics and Imaging in Radiation Oncology*, 15, 23–29. <https://doi.org/10.1016/j.phro.2020.06.005>
- Kooreman, E. S., van Houdt, P. J., Keesman, R., Pos, F. J., van Pelt, V. W. J., Nowee, M. E., Wetscherek, A., Tijssen, R. H. N., Philippens, M. E. P., Thorwarth, D., Wang, J., Shukla-Dave, A., Hall, W. A., Paulson, E. S., & van der Heide, U. A. (2020). ADC measurements on the Unity MR-linac – a recommendation on behalf of the Elekta Unity MR-linac consortium. *Radiotherapy and Oncology*, 153, 106–113. <https://doi.org/10.1016/j.radonc.2020.09.046>

-
- Lagendijk, J. J. W., Raaymakers, B. W., & van Vulpen, M. (2014). The magnetic resonance imaging–linac system. *Seminars in Radiation Oncology*, 24(3), 207–209. <https://doi.org/10.1016/j.semradonc.2014.02.009>
- Larkman, D. J., Hajnal, J. V., Herlihy, A. H., Coutts, G. A., Young, I. R., & Ehnholm, G. (2001). Use of multicoil arrays for separation of signal from multiple slices simultaneously excited. *Journal of Magnetic Resonance Imaging*, 13(2), 313–317. [https://doi.org/10.1002/1522-2586\(200102\)13:2<313::AID-JMRI1045>3.0.CO;2-W](https://doi.org/10.1002/1522-2586(200102)13:2<313::AID-JMRI1045>3.0.CO;2-W)
- Li, Z., & Conti, P. S. (2010). Radiopharmaceutical chemistry for positron emission tomography. *Advanced Drug Delivery Reviews*, 62(11), 1031–1051. <https://doi.org/10.1016/j.addr.2010.09.007>
- Liu, F., Fu, S., Chen, Y., Yan, O., He, L., Jiang, C., Wu, X., Han, Y., & Wang, H. (2021). A randomized phase II trial of diffusion-weighted MR imaging-guided radiotherapy plus chemotherapy versus standard chemoradiotherapy in locoregional advanced nasopharyngeal carcinoma. *Journal of Clinical Oncology*, 39(15), 6018–6018. https://doi.org/10.1200/JCO.2021.39.15_suppl.6018
- Lustig, M., Donoho, D., & Pauly, J. M. (2007). Sparse MRI: The application of compressed sensing for rapid MR imaging. *Magnetic Resonance in Medicine*, 58(6), 1182–1195. <https://doi.org/10.1002/mrm.21391>
- Malkov, V. N., & Rogers, D. W. O. (2016). Charged particle transport in magnetic fields in EGSnrc. *Medical Physics*, 43(7), 4447–4458. <https://doi.org/10.1118/1.4954318>
- Mandija, S., D’Agata, F., Navest, R. J. M., Sbrizzi, A., Tijssen, R. H. N., Philippens, M. E. P., Raaijmakers, C. P. J., Seravalli, E., Verhoeff, J. J. C., Lagendijk, J. J. W., & van den Berg, C. A. T. (2019). Brain and head-and-neck MRI in immobilization mask: A practical solution for MR-only radiotherapy. *Frontiers in Oncology*, 9, 647. <https://doi.org/10.3389/fonc.2019.00647>
- Mansfield, P. (1977). Multi-planar image formation using NMR spin echoes. *Journal of Physics C: Solid State Physics*, 10(3), L55–L58. <https://doi.org/10.1088/0022-3719/10/3/004>
- McDermott, L. N., Louwe, R. J. W., Sonke, J. J., van Herk, M. B., & Mijnheer, B. J. (2004). Dose-response and ghosting effects of an amorphous silicon electronic portal imaging device. *Medical Physics*, 31(2), 285–295. <https://doi.org/10.1118/1.1637969>
- McRobbie, D. W. (2003). *MRI from picture to proton* (2nd ed.). Cambridge University Press.
- Mehta, J., & Majumdar, A. (2017). RODEO: Robust DE-aliasing autoencoder for real-time medical image reconstruction. *Pattern Recognition*, 63, 499–510. <https://doi.org/10.1016/j.patcog.2016.09.022>
- Mollaie, M. S. M., van Leeuwen, C. C., Raaijmakers, A. J. E., & Simovski, C. R. (2020). Analysis of high impedance coils both in transmission and reception regimes. *IEEE Access*, 8, 129754–129762. <https://doi.org/10.1109/ACCESS.2020.3009367>
- Moszyńska-Zielińska, M., Chałubińska-Fendler, J., Gottwald, L., Żytko, L., Bigos, E., & Fijuth, J. (2014). Does obesity hinder radiotherapy in endometrial cancer patients? the implementation of new techniques in adjuvant radiotherapy –

- focus on obese patients. *Przegląd Menopauzalny - Menopause Review*, 13(2), 96–100. <https://doi.org/10.5114/pm.2014.42710>
- Mutic, S., & Dempsey, J. F. (2014). The ViewRay system: Magnetic resonance-guided and controlled radiotherapy. *Seminars in Radiation Oncology*, 24(3), 196–199. <https://doi.org/10.1016/j.semradonc.2014.02.008>
- Nejad-Davarani, S. P., Zakariaei, N., Chen, Y., Haacke, E. M., Hurst, N. J., Siddiqui, M. S., Schultz, L. R., Snyder, J. M., Walbert, T., & Glide-Hurst, C. K. (2020). Rapid multicontrast brain imaging on a 0.35T MR-linac. *Medical Physics*, 47(9), 4064–4076. <https://doi.org/10.1002/mp.14251>
- Paulus, D. H., Braun, H., Aklan, B., & Quick, H. H. (2012). Simultaneous PET/MR imaging: MR-based attenuation correction of local radiofrequency surface coils. *Medical Physics*, 39(7), 4306–4315. <https://doi.org/10.1118/1.4729716>
- Pfaehler, E., de Jong, J. R., Dierckx, R. A. J. O., van Velden, F. H. P., & Boellaard, R. (2018). SMART (SiMulAtion and ReconsTruction) PET: An efficient PET simulation-reconstruction tool. *EJNMMI Physics*, 5(1), 16. <https://doi.org/10.1186/s40658-018-0215-x>
- Pruessmann, K. P., Weiger, M., Scheidegger, M. B., & Boesiger, P. (1999). SENSE: Sensitivity encoding for fast MRI. *Magnetic Resonance in Medicine*, 42(5), 952–962.
- Purdy, J. A. (1992). Photon dose calculations for three-dimensional radiation treatment planning. *Seminars in Radiation Oncology*, 2(4), 235–245. [https://doi.org/10.1016/1053-4296\(92\)90021-C](https://doi.org/10.1016/1053-4296(92)90021-C)
- Raaijmakers, A. J. E., Raaymakers, B. W., & Lagendijk, J. J. W. (2005). Integrating a MRI scanner with a 6 MV radiotherapy accelerator: Dose increase at tissue-air interfaces in a lateral magnetic field due to returning electrons. *Physics in Medicine and Biology*, 50(7), 1363–1376. <https://doi.org/10.1088/0031-9155/50/7/002>
- Rispoli, J. V. (2019). Best practices for safety testing of experimental RF hardware: Report from the ISMRM working group. *Procs. ISMRM Workshop on MR Safety*. <https://cds.ismrm.org/protected/Safety19/program/syllabi/Rispoli.pdf>
- Roemer, P. B., Edelstein, W. A., Hayes, C. E., Souza, S. P., & Mueller, O. M. (1990). The NMR phased array. *Magnetic Resonance in Medicine*, 16(2), 192–225. <https://doi.org/10.1002/mrm.1910160203>
- Ruytenberg, T., Webb, A., & Zivkovic, I. (2020). Shielded-coaxial-cable coils as receive and transceive array elements for 7T human MRI. *Magnetic Resonance in Medicine*, 83(3), 1135–1146. <https://doi.org/10.1002/mrm.27964>
- Samolýk-Kogaczewska, N., Sierko, E., Zuzda, K., Gugnacki, P., Szumowski, P., Mojsak, M., Burzyńska-Śliwowska, J., Wojtukiewicz, M. Z., Szczecina, K., & Jurgilewicz, D. H. (2019). PET/MRI-guided GTV delineation during radiotherapy planning in patients with squamous cell carcinoma of the tongue. *Strahlentherapie und Onkologie*, 195(9), 780–791. <https://doi.org/10.1007/s00066-019-01480-3>
- Sander, C. Y., Keil, B., Chonde, D. B., Rosen, B. R., Catana, C., & Wald, L. L. (2015). A 31-channel MR brain array coil compatible with positron emission tomography.

-
- Magnetic Resonance in Medicine*, 73(6), 2363–2375. <https://doi.org/10.1002/mrm.25335>
- Schakel, T., Hoogduin, J. M., Terhaard, C. H. J., & Philippens, M. E. P. (2017). Technical note: Diffusion-weighted MRI with minimal distortion in head-and-neck radiotherapy using a turbo spin echo acquisition method. *Medical Physics*, 44(8), 4188–4193. <https://doi.org/10.1002/mp.12363>
- Schlemper, J., Caballero, J., Hajnal, J. V., Price, A. N., & Rueckert, D. (2018). A deep cascade of convolutional neural networks for dynamic MR image reconstruction. *IEEE Transactions on Medical Imaging*, 37(2), 491–503. <https://doi.org/10.1109/TMI.2017.2760978>
- Sijbers, J., den Dekker, A. J., van Audekerke, J., Verhoye, M., & van Dyck, D. (1998). Estimation of the noise in magnitude MR images. *Magnetic Resonance Imaging*, 16(1), 87–90. [https://doi.org/10.1016/S0730-725X\(97\)00199-9](https://doi.org/10.1016/S0730-725X(97)00199-9)
- Spadea, M. F., Maspero, M., Zaffino, P., & Seco, J. (2021). Deep learning-based synthetic-CT generation in radiotherapy and PET: A review [Accepted Author Manuscript]. *Medical Physics*, 1–30. <https://doi.org/10.1002/mp.15150>
- Tellmann, L., Quick, H. H., Bockisch, A., Herzog, H., & Beyer, T. (2011). The effect of MR surface coils on PET quantification in whole-body PET/MR: Results from a pseudo-PET/MR phantom study. *Medical Physics*, 38(5), 2795–2805. <https://doi.org/10.1118/1.3582699>
- Terpstra, M. L., d'Agata, F., Stemkens, B., Lagendijk, J. J. W., van den Berg, C. A. T., & Tijssen, R. H. N. (2020a). Reconstructing non-cartesian acquisitions using dAUTOMAP. *Procs ISMRM 28*.
- Terpstra, M. L., Maspero, M., d'Agata, F., Stemkens, B., Intven, M. P. W., Lagendijk, J. J. W., Berg, C. A. T. v. d., & Tijssen, R. H. N. (2020b). Deep learning-based image reconstruction and motion estimation from undersampled radial k-space for real-time MRI-guided radiotherapy. *Physics in Medicine & Biology*, 65(15), 155015. <https://doi.org/10.1088/1361-6560/ab9358>
- Uecker, M., Lai, P., Murphy, M. J., Virtue, P., Elad, M., Pauly, J. M., Vasanawala, S. S., & Lustig, M. (2014). ESPIRiT—an eigenvalue approach to autocalibrating parallel MRI: Where SENSE meets GRAPPA. *Magnetic Resonance in Medicine*, 71(3), 990–1001. <https://doi.org/10.1002/mrm.24751>
- Uijtewaal, P., Borman, P. T. S., Woodhead, P. L., Hackett, S. L., Raaymakers, B. W., & Fast, M. F. (2021). Dosimetric evaluation of MRI-guided multi-leaf collimator tracking and trailing for lung stereotactic body radiation therapy. *Medical Physics*, 48(4), 1520–1532. <https://doi.org/10.1002/mp.14772>
- UMC Utrecht. (2021, March 19). *MRI/PET kan uitgezaaide tumoren beter beheersen*. Retrieved July 22, 2021, from <https://www.umcutrecht.nl/nieuws/mri-pet-kan-uitgezaaide-tumoren-beter-beheersen>
- van Herk, M. (2004). Errors and margins in radiotherapy. *Seminars in Radiation Oncology*, 14(1), 52–64. <https://doi.org/10.1053/j.semradonc.2003.10.003>
- Vaughan, J. T., & Griffiths, J. R. (Eds.). (2012, December 19). *RF coils for MRI* (1st ed.). Wiley.

- Vaughan, J. T., Hetherington, H. P., Otu, J. O., Pan, J. W., & Pohost, G. M. (1994). High frequency volume coils for clinical NMR imaging and spectroscopy. *Magnetic Resonance in Medicine*, 32(2), 206–218. <https://doi.org/10.1002/mrm.1910320209>
- Verduijn, G. M., Bartels, L. W., Raaijmakers, C., Terhaard, C., Pameijer, F. A., & van den Berg, C. (2009). Magnetic resonance imaging protocol optimization for delineation of gross tumor volume in hypopharyngeal and laryngeal tumors. *International Journal of Radiation Oncology, Biology, Physics*, 74(2), 630–636. <https://doi.org/10.1016/j.ijrobp.2009.01.014>
- Wahl, R. L., & Beanlands, R. S. B. (Eds.). (2008, November 25). *Principles and practice of PET and PET/CT* (2nd ed.). Lippincott Williams & Wilkins.
- Wahl, R. L., Jacene, H., Kasamon, Y., & Lodge, M. A. (2009). From RECIST to PERCIST: Evolving considerations for PET response criteria in solid tumors. *Journal of Nuclear Medicine: Official Publication, Society of Nuclear Medicine*, 50 Suppl 1, 122S–50S. <https://doi.org/10.2967/jnumed.108.057307>
- Webb, A. G., & Balcom, B. (Eds.). (2016, May 11). *Magnetic resonance technology*. Royal Society of Chemistry. <https://doi.org/10.1039/9781782623878>
- Welting, D., van Leeuwen, C., Raaijmakers, A., & Klomp, D. (2020). An automated 32 channel VNA RF switch for high density coil prototyping. *Procs ISMRM 2020*.
- Winkel, D., Werensteijn-Honingh, A. M., Eppinga, W. S. C., Intven, M. P. W., Hes, J., Snoeren, L. M. W., Visser, S. A., Bol, G. H., Raaymakers, B. W., Jürgenliemk-Schulz, I. M., & Kroon, P. S. (2021). Dosimetric feasibility of hypofractionation for SBRT treatment of lymph node oligometastases on the 1.5T MR-linac. *Radiotherapy and Oncology*, 154, 243–248. <https://doi.org/10.1016/j.radonc.2020.09.020>
- Wollenweber, S. D., Delso, G., Deller, T., Goldhaber, D., Hüllner, M., & Veit-Haibach, P. (2014). Characterization of the impact to PET quantification and image quality of an anterior array surface coil for PET/MR imaging. *Magma*, 27(2), 149–159. <https://doi.org/10.1007/s10334-013-0388-1>
- Wulff, J., Zink, K., & Kawrakow, I. (2008). Efficiency improvements for ion chamber calculations in high energy photon beams. *Medical Physics*, 35(4), 1328–1336. <https://doi.org/10.1118/1.2874554>
- Xia, P., Godley, A., Shah, C., Videtic, G. M. M., Suh, J. H., Xia, P., Godley, A., Mastroianni, A., Suh, J. H., Donaghue, J., Xia, P., Yu, N., Greskovich, J., Suh, J. H., Zickefoose, L., Godley, A., Vassil, A., Shah, C., Kolar, M., ... Suh, J. H. (2018). *Strategies for radiation therapy treatment planning*. Springer Publishing Company. Retrieved March 26, 2021, from <https://connect.springerpub.com/content/book/978-0-8261-2267-4>
- Yan, L., Wang, H., Du, X., & Feng, M. (2021). Early efficacy prediction of nasopharyngeal carcinoma based on 3D-ADC value acquired during radiotherapy: A phase II prospective study. *Journal of Clinical Oncology*, 39(15), e18018–e18018. https://doi.org/10.1200/JCO.2021.39.15_suppl.e18018
- Zhang, B., Sodickson, D. K., & Cloos, M. A. (2018). A high-impedance detector-array glove for magnetic resonance imaging of the hand. *Nature Biomedical Engineering*, 2(8), 570–577. <https://doi.org/10.1038/s41551-018-0233-y>

-
- Zijlema, S. E., Branderhorst, W., Bastiaannet, R., Tijssen, R. H. N., Lagendijk, J. J. W., & van den Berg, C. A. T. (2021). Minimizing the need for coil attenuation correction in integrated PET/MRI at 1.5 T using low-density MR-linac receive arrays [Publisher: IOP Publishing]. *Physics in Medicine & Biology*, 66(20), 20NT01. <https://doi.org/10.1088/1361-6560/ac2a8a>
- Zijlema, S. E., Tijssen, R. H. N., Malkov, V. N., van Dijk, L., Hackett, S. L., Kok, J. G. M., Lagendijk, J. J. W., & van den Berg, C. A. T. (2019a). Design and feasibility of a flexible, on-body, high impedance coil receive array for a 1.5 T MR-linac. *Physics in Medicine & Biology*, 64(18), 185004. <https://doi.org/10.1088/1361-6560/ab37a8>
- Zijlema, S. E., Tijssen, R. H. N., van Dijk, L., Hackett, S. L., Wolthaus, J. W. H., Breimer, W., Lagendijk, J. J. W., & van den Berg, C. A. T. (2020). Improving the imaging performance of the 1.5 T MR-linac using a flexible, 32-channel, on-body receive array. *Physics in Medicine & Biology*, 65(21), 215008. <https://doi.org/10.1088/1361-6560/aba87a>
- Zijlema, S. E., van Dijk, L., Westlund Gotby, L. E., Italiaander, M. G., Tijssen, R. H. N., Lagendijk, J. J. W., & van den Berg, C. A. T. (2019b). A mask-compatible, radiolucent head and neck receive array for MRI-guided radiotherapy treatments and pre-treatment simulation. *Procs 7th MR in RT*, 23.

Publications

Published articles

- S.J. Hoogcarpsel, **S.E. Zijlema**, R.H.N. Tijssen, L.G.W. Kerkmeijer, I.M. Jürgenliemk-Schulz, J.J.W. Lagendijk, & B.W. Raaymakers (2018). Characterization of the first RF coil dedicated to 1.5 T MR guided radiotherapy. *Physics in Medicine & Biology*, 63(2), 025014.
- S.E. Zijlema**, R.H.N. Tijssen, V.N. Malkov, L. van Dijk, S.L. Hackett, J.G.M. Kok, J.J.W. Lagendijk, & C.A.T. van den Berg (2019). Design and feasibility of a flexible, on-body, high impedance coil receive array for a 1.5 T MR-linac. *Physics in Medicine & Biology*, 64(18), 185004.
- R.J.M. Navest, S. Mandija, **S.E. Zijlema**, B. Stemkens, A. Andreychenko, J.J.W. Lagendijk, & C.A.T. van den Berg (2020). The noise navigator for MRI-guided radiotherapy: An independent method to detect physiological motion. *Physics in Medicine and Biology*, 65(12), 12NT01.
- S.E. Zijlema**, R.H.N. Tijssen, L. van Dijk, S.L. Hackett, J.W.H. Wolthaus, W. Breimer, J.J.W. Lagendijk, & C.A.T. van den Berg (2020). Improving the imaging performance of the 1.5 T MR-linac using a flexible, 32-channel, on-body receive array. *Physics in Medicine & Biology*, 65(21), 215008.
- S.E. Zijlema**, W. Branderhorst, R. Bastiaannet, R.H.N. Tijssen, J.J.W. Lagendijk, & C.A.T. van den Berg (2021). Minimizing the need for coil attenuation correction in integrated PET/MRI at 1.5 T using low-density MR-linac receive arrays. *Physics in Medicine & Biology*, 66(20), 20NT01.

Submitted article

- S.E. Zijlema**, W. Breimer, W.J.M. Gosselink, T. Bruijnen, C.S. Arteaga de Castro, R.H.N. Tijssen, M.E.P. Philippens, J.J.W. Lagendijk, & C.A.T. van den Berg. A mask-compatible, radiolucent, 8-channel head and neck receive array for MRI-guided radiotherapy treatments and pre-treatment simulation. *Physics in Medicine & Biology*, submitted.

Conference proceedings

- S.E. Zijlema**, L. van Dijk, S.L. Hackett, J.J.W. Lagendijk, R.H.N. Tijssen, C.A.T. van den Berg. *Development of a radiolucent 64-channel on-body receive array for the MR-linac*. Proc. ImagO conference, Utrecht, 2017 (oral presentation)
- S.E. Zijlema**, L. van Dijk, S.L. Hackett, J.J.W. Lagendijk, R.H.N. Tijssen, C.A.T. van den Berg. *Development of a radiolucent 64-channel on-body receive array to enhance image quality of the MR-linac*. Proc. ISMRM Benelux, Antwerp, 2018 (oral presentation)
- S.E. Zijlema**, L. van Dijk, S.L. Hackett, J.J.W. Lagendijk, R.H.N. Tijssen, C.A.T. van den Berg. *Dosimetric feasibility of on-body receive array placement to enhance image quality in the MR-linac*. Proc. ESTRO, Barcelona, 2018 (oral presentation)
- S.E. Zijlema**, L. van Dijk, S.L. Hackett, J.J.W. Lagendijk, R.H.N. Tijssen, C.A.T. van den Berg. *Development of a radiolucent 64-channel on-body receive array to enhance the image quality of the MR-linac*. Proc. ISMRM, Paris, 2018 (traditional poster)
- S.E. Zijlema**, L. van Dijk, S.L. Hackett, J.J.W. Lagendijk, R.H.N. Tijssen, C.A.T. van den Berg. *Development of a radiolucent 64-channel on-body receive array to enhance the image quality of the MR-linac*. Proc. ImagO conference, Utrecht, 2018 (oral presentation)
- S.E. Zijlema**, L. van Dijk, S.L. Hackett, J.J.W. Lagendijk, R.H.N. Tijssen, C.A.T. van den Berg. *Dosimetric feasibility of on-body receive array placement to enhance image quality in the MR-linac*. Proc. MR in RT, Utrecht, 2018 (traditional poster)
- S.E. Zijlema**, L. van Dijk, S.L. Hackett, J.J.W. Lagendijk, R.H.N. Tijssen, C.A.T. van den Berg. *A radiolucent and flexible high impedance coil array to increase the imaging performance on a 1.5T MR-linac*. Proc. I2I workshop, New York, 2018 (power pitch)
- S.E. Zijlema**. *Radiolucent and flexible MR-linac coil design*. Proc. NVKF Kringdag radiotherapie, Utrecht, 2019 (oral presentation)
- S.E. Zijlema**, L. van Dijk, J.J.W. Lagendijk, R.H.N. Tijssen, C.A.T. van den Berg. *A radiolucent and flexible high impedance coil array to increase the imaging performance of a 1.5T MR-linac*. Proc. ISMRM Benelux Chapter, Leiden, 2019 (traditional poster)
- S.E. Zijlema**, L. van Dijk, J.J.W. Lagendijk, R.H.N. Tijssen, C.A.T. van den Berg. *A radiolucent and flexible high impedance coil array to increase the imaging performance of a 1.5T MR-linac*. Proc. 27th ISMRM, Montreal, 2019 (electronic poster)
- S.E. Zijlema**, W. Branderhorst, L. van Dijk, D.W.J. Klomp, H.W.A.M. de Jong, R.H.N. Tijssen, C.A.T. van den Berg. *A low-density receive array to improve PET sensitivity in integrated PET/MRI*. Proc. PSMR, Munich, 2019 (oral presentation)

- S.E. Zijlema**, W. Branderhorst, L. van Dijk, D.W.J. Klomp, H.W.A.M. de Jong, R.H.N. Tijssen, C.A.T. van den Berg. *Usability of radiolucent MRI-guided radiotherapy receive arrays in hybrid PET/MRI systems*. Proc. MR in RT, Toronto, 2019 (oral presentation)
- S.E. Zijlema**, L. van Dijk, L.E.L. Westlund Gotby, M.G.M. Italiaander, J.J.W. Lagendijk, R.H.N. Tijssen, C.A.T. van den Berg. *A mask-compatible, radiolucent head and neck receive array for MRI-guided radiotherapy treatments and pre-treatment simulation*. Proc. MR in RT, Toronto, 2019 (oral presentation)
- S.E. Zijlema**, L. van Dijk, L.E.L. Westlund Gotby, M.G.M. Italiaander, J.J.W. Lagendijk, R.H.N. Tijssen, C.A.T. van den Berg. *Radiolucency of a 32-channel high impedance coil receive array for the 1.5T MR-linac*. Proc. MR in RT, Toronto, 2019 (traditional poster)
- S.E. Zijlema**, L. van Dijk, J.J.W. Lagendijk, R.H.N. Tijssen, C.A.T. van den Berg. *A radiolucent and flexible high impedance coil array to increase the imaging performance of a 1.5T MR-linac*. Proc. ImagO conference, Utrecht, 2019 (oral presentation)
- S.E. Zijlema**, L. van Dijk, J.J.W. Lagendijk, D.W.J. Klomp, C.S. Arteaga de Castro, R.H.N. Tijssen, and C.A.T. van den Berg. *A radiolucent 32-channel high impedance coil receive array to accelerate 3D imaging on hybrid 1.5 T MR-linac systems*. Proc. ISMRM, 2020 (electronic poster)
- S.E. Zijlema**, L. van Dijk, J.J.W. Lagendijk, D.W.J. Klomp, C.S. Arteaga de Castro, R.H.N. Tijssen, and C.A.T. van den Berg. *A radiolucent 32-channel high impedance coil receive array to accelerate 3D imaging on hybrid 1.5 T MR-linac systems*. Proc. ISMRM Benelux, Arnhem, 2020 (oral presentation)
- S.E. Zijlema**, L. van Dijk, J.J.W. Lagendijk, R.H.N. Tijssen, C.A.T. van den Berg. *Reducing scan times using a 32-channel, on-body receive array for the 1.5T MR-linac*. Proc. MR in RT, 2020 (oral presentation)
- S.E. Zijlema**, W. Breimer, W.J.M. Gosselink, T. Bruijnen, C.S. Arteaga de Castro, R.H.N. Tijssen, M.E.P. Philippens, J.J.W. Lagendijk, and C.A.T. van den Berg. *A dedicated head and neck array for improved image quality on a 1.5 T MR-linac (and MRI-simulator)*. Proc. Elekta MR-linac Consortium Meeting, 2021 (oral presentation)
- B.R. Steensma, **S.E. Zijlema**, A.J.E. Raaijmakers, C.C. van Leeuwen, C.A.T. van den Berg. *The (un)expected benefits of coaxial antennas for MRI*. Proc. ICEAA, 2021

Awards

Best presentation award, ImagO conference, 2018

Dankwoord

In totaal heeft mijn UMC-carrière ruim vijf jaar geduurd. In deze jaren heeft de inhoud van mijn projecten zich uitgestrekt van MRI tot (PET-)CT en van beeldregistratie tot dosimetrie. Deze projecten waren niet mogelijk geweest zonder de hulp van de vele experts en behulpzame collega's die de afdeling telt.

Om chronologisch te beginnen wil ik Bas, Sjoerd en Markus bedanken. Bas, jij inspireerde mij met je presentatie over de MR-linac om mijn afstudeerproject in Utrecht te komen doen. Zo maakte ik kennis met deze mooie afdeling en gezellige groep onderzoekers. Sjoerd en Markus, in jullie dagelijkse begeleiding lieten jullie mij kennismaken met de vele interessante onderzoeksrichtingen van de afdeling. Die brede kennis heeft mij tijdens mijn promotie geholpen om alle consequenties van een nieuwe ontvangstspoel voor de MR-linac te kunnen begrijpen.

Vervolgens wil ik Nico en Rob bedanken. Allereerst voor het aannemen, maar ook voor de prettige begeleiding waarbij ik vrij werd gelaten of juist actief werd geholpen, afhankelijk van wat ik nodig had.

Nico, met jouw vriendelijke, empathische en kalme manier van leidinggeven ben je voor mij een groot voorbeeld. Ondanks je drukke agenda wist je altijd een moment vrij te maken om mijn voortgang en problemen te bespreken. Ook in mindere tijden tijdens mijn PhD was je vol begrip en empathie. Je kennis is ongelooflijk breed, maar je bent nog even leergierig als een beginnend promovendus. Elke nieuwe analyse of methode die in beeld komt, wil je begrijpen en daardoor kun je altijd inhoudelijk meepraten of meedenken over oplossingen. Ik vind het dan ook volledig terecht dat je inmiddels professor bent en dat ik onder jou mag promoveren.

Rob, ons contact was net iets minder intensief, maar daardoor niet minder waardevol. Jouw scherpe blik en klinische ervaring waren erg belangrijk als Nico en ik weer eens iets hadden bedacht wat in theorie een goed idee was, maar in de praktijk niet zou werken. Jouw sociale vaardigheden zijn eindeloos, een eigenschap die prettig is op de afdeling en volledig tot zijn recht komt tijdens congressen. Ik heb onze trip naar NYC voor de i2i Workshop, en de contacten die we daar hebben gelegd, dan ook erg gewaardeerd. Des te meer vond ik het jammer dat je besloot om dichterbij huis te gaan werken, maar ook vanuit het Catharina vond je het belangrijk om op de hoogte te blijven en bleef je van toegevoegde waarde voor het project.

Jan, niets van het werk uit deze thesis was mogelijk geweest zonder jouw baanbrekende werk aan de MR-linac. Tijdens mijn promotie waren je feedback op abstracts/artikelen en boeiende gesprekken (tijdens RESOLVE user meetings of borrels) erg waardevol. Ik ben erg benieuwd naar de ontwikkelingen in de komende jaren: meer doelgebieden, meer real-time toepassingen.

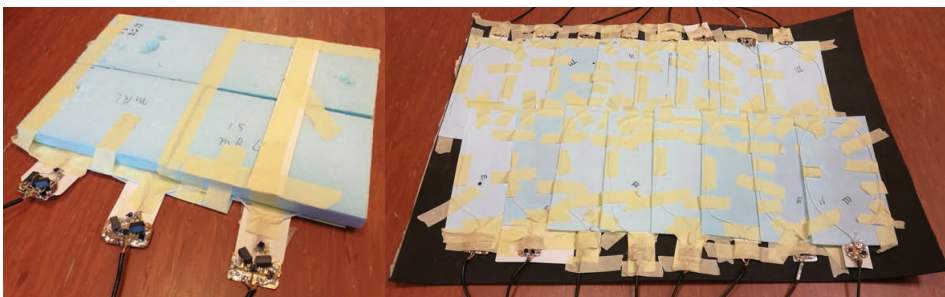
De voorzitter en leden van de Beoordelingscommissie: prof. dr. Chris Terhaard, prof. dr. Bas Raaymakers, prof. dr. Andrew Webb, prof. dr. Dennis Klomp en prof. dr. ir. Hugo de Jong, graag wil ik jullie bedanken voor het lezen en beoordelen van dit proefschrift.

Alle (ex-)RESOLVE'ers: Luca, Tom, Maarten, Matteo, Niek, Alessandro, Bjorn, Gabrio, Federico. Onze wekelijkse meetings waren altijd waardevol om tot nieuwe inzichten te komen, maar waren ook gewoon gezellig. Binnen de groep stond iedereen altijd klaar om een ander te helpen, bijvoorbeeld door scripts te delen of door te helpen met experimenten of analyses. Bedankt hiervoor!

Luca, onze RESOLVE-afgevaardigde in het coil lab. Jouw hulp was onmisbaar bij het maken van prototypes en het bijsturen van onze plannen als deze elektrotechnisch onhaalbaar waren. Bedankt voor de soldeerlessen waardoor ik uiteindelijk zelf ook kon helpen met het in elkaar zetten van een nieuw prototype (HIC's FTW). Onze soldeerkunsten hebben zelfs de andere RESOLVE'ers geïnspireerd om de soldeerbout op te pakken om mij een schitterende ketting te schenken tijdens mijn bruiloft. Ook Dimitri, Caesar, Erik, Aidin, Ingmar en de andere coil-lab engineers: bedankt voor jullie hulp bij het bouwen van de prototypes.

Bij Tesla DC wil ik de (onvermoeibaar enthousiaste) Martino, Catalina, Wico en andere medewerkers aan het MR-linac coil project bedanken. Zonder jullie hulp hingen de prototypes nu nog steeds met plakband aan elkaar (zie Figuur 1). Het is mooi om te zien hoe jullie de ontwerpen uit deze thesis nu professionaliseren en doorontwikkelen voor klinisch gebruik.

Woutjan en Remco, zonder jullie inbreng was het PET/MRI stuk uit deze thesis niet tot stand gekomen. Jullie hulp was hard nodig bij het uitvoeren van de PET experimenten en data analyses. Remco, jouw code en ervaring met e7-tools hebben hoofdstuk 5 mogelijk gemaakt. Zelfs vanuit de VS heb je input geleverd en tips gegeven. Woutjan, jouw PET kennis hielp goed bij het voorbereiden van experimenten en je praktische hulp erbij was erg prettig.



Figuur 1 De eerste (werkende!) plakband-prototypes.

Sara, Jochem, Mark G., Marielle, Wilfred, André, Emy, Thomas, Bastiaan, Tuan, Marijn, Eveline en alle laboranten, bedankt voor jullie hulp tijdens mijn vele experimenten. Zonder jullie hulp had ik nooit zoveel verschillende metingen uit kunnen voeren. Ook Jan (K.) hoort natuurlijk in dit rijtje thuis. Jij bent een van de meest gepassioneerde medewerkers van de afdeling met een decennialange ervaring met de MR-linac. Zeker aan het begin van mijn promotie heb je mij enorm veel bijgebracht over straling, linacs en de MR-linac.

Alexis, Gijs, Dawit, Mark, Erwin en alle andere ICT-medewerkers, ik heb vaker aan jullie bureau gestaan dan ik had (en jullie hadden) gewild, maar altijd werd ik geholpen en werden oplossingen bedacht voor mijn problemen. Dank hiervoor.

Judith en Yvette, het is een algemeen geaccepteerde wijsheid dat je secretaresses te vriend moet houden en bij jullie was dat niet moeilijk. Altijd als ik de voorraadkast leeg kwam roven of jullie hulp nodig had met administratieve zaken, volgde een gezellig praatje en vertrok ik met een glimlach (en mijn armen vol dozen thee, nietmachines, printerpapier, ...).

My office mates from Q02: Maarten, Robin, Charis, Georgios, and Szabolz. You were the ones that I spent most of the day with, which I thoroughly enjoyed. Dozens of coffee breaks, going to the coffee pantry for 'luxe broodjes' or cake, and complaining about *reply-all* e-mail threads really creates a bond. Maarten, ik heb nooit spijt gehad van mijn voorstel om je in contact te brengen met Nico voor een PhD in het UMC. Dat je vervolgens ook nog mijn kantoorgenoot werd, was ook een (gezellige) meevaller. Robin, ik hoop dat je me nog niet zat was, want inmiddels zijn we weer collega's.

Alle tafelvoetballers, Osman, Mike (*NEE, NEE, NEE*), Maureen, Ellis, Anna, Mark (*it's not over 'til the fat lady sings*), bedankt voor het dagelijkse ontspanmoment om 16:00. Tom, wij wisten zelfs twee keer vicekampioen te worden op het radiotherapie tafelvoetbaltoernooi (en zijn beide keren verslagen door Ellart...). Tijdens de corona-thuiswerkperiode miste ik dit natuurlijk het meest.

Alle andere (ex-)OiO's en AiO's, bedankt voor jullie gezelligheid tijdens alle OiO uitjes, congressen, borrels, activiteiten en meetings. Stan, Mike, Daan, Filipa, Jorine, Tim, Steven, Pim, Joris, Sophie, Hans, Soraya, Filipa, Dennis, Mick en alle anderen: dank jullie wel!

Tenslotte wil ik iedereen van de radiotherapieafdeling bedanken. In 2015 begon ik aan mijn Master afstudeerproject op de afdeling. Op dat moment wist ik niet wat ik na mijn studie wilde doen, maar één ding wist ik zeker: ik wil in ieder geval niet gaan promoveren. De overweldigend positieve ervaring op de afdeling, een combinatie van razend interessant onderzoek en een gemoedelijke en behulpzame sfeer, brachten mij tot inkeer en in 2017 begon ik hier toch aan een promotie. Er is ongelooflijk veel kennis op de afdeling en daarvan wordt optimaal geprofiteerd door de openheid en behulpzaamheid, waardoor onverwachte (interdisciplinaire) samenwerkingsverbanden ontstaan en snel vooruitgang kan worden geboekt. Ook laboranten staan altijd klaar

om te helpen, zelfs tussen patiënten door, als er weer eens een onderzoeker belt voor hulp met een vreemd klinkend experiment. Daarnaast is het ook gewoon erg gezellig op de afdeling en heb ik genoten van alle activiteiten, borrels, lunches, samenkomsten en uitjes. Ik gun iedereen zo'n omgeving en hoop deze in al mijn toekomstige functies weer te vinden.

Om een promotietraject vol te houden, is het natuurlijk ook belangrijk om (op de juiste momenten) te ontspannen. Daarom wil ik graag Mark, Pieter, Martijn, Tom en de hele vriendengroep uit Eindhoven (Denise, Jacques, Meike, Moniek, Pascal, Rens, Rick, Rowin, Saskia, Stan en Tim) bedanken voor de mooie avonden, activiteiten en vakanties waarna ik weer met frisse moed (of volledig uitgeput) verder kon met het werk in deze thesis.

Pap, mam, Eline, bedankt voor jullie steun in deze jaren. Ook al woon ik al jaren niet meer in Apeldoorn, toch voelt het altijd weer als thuiskomen en voel ik me altijd welkom. Wim en Marian, ook bij jullie voel ik me inmiddels altijd welkom.

Tot slot, de belangrijkste persoon voor mij. Lieve Ilona, bedankt voor je onvoorwaardelijke steun tijdens mijn hele promotietraject. De afgelopen jaren zijn niet altijd makkelijk geweest voor ons beiden, maar hebben zeker ook onmiskenbare hoogtepunten gekend, zoals onze bruiloft. Het feit dat ik elke dag thuiskwam bij iemand die een soortgelijk traject doorliep en mijn dagelijkse PhD-problematiek begreep, was erg waardevol. Sterker nog, naarmate mijn project vorderde, begon je zelfs inhoudelijk best goed te begrijpen wat ik deed! Nu is het tijd voor een volgende stap voor mij, en iets later ook voor jou. Ik ben erg benieuwd naar wat de toekomst ons gaat brengen, maar zie het vol vertrouwen tegemoet.

Curriculum Vitae

Stefan Zijlema was born on August 18th, 1993 in Apeldoorn, the Netherlands. He attended high school at the Christelijk Lyceum Apeldoorn and received his Gymnasium diploma in 2010. After a gap year at a high school in the United States, he studied Biomedical Engineering (Bachelor) and Medical Engineering (Master) at the Eindhoven University of Technology. During these years, he focused on biomedical imaging with MRI in particular. He conducted his Master thesis at the University Medical Center (UMC) Utrecht, where



he worked on dynamic prostate MRI for the 1.5 T MR-linac. Subsequently, he performed an externship at Philips Research in Hamburg, Germany, where he worked on 4D MRI techniques to capture respiratory motion. In 2017, Stefan returned to the UMC Utrecht to start a PhD, where he developed radiation transparent MRI receive arrays for MRI-guided radiotherapy and PET/MRI. The results of this research are presented in this thesis.

Currently, Stefan is working at the Netherlands Cancer Institute as a Clinical Scientist.

